Durham E-Theses

Production of y* resonances by low energy k(^-) mesons

Fleming, George Peter

TO

YVONNE

AND

MY PARENTS

Production of Y* Resonances

by Low Energy K⁻ Mesons

A thesis presented by

George Peter Fleming

for the

Degree of Doctor of Philosophy

at the

University of Durham

September, 1977
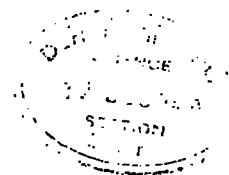
Y CO-ORD

28.

18.

e−

e+

e−

e+

e−

e+

p

π−

K−

53.1

43.1

33.1

23.1

13.1

X CO-ORD

FRAME 1331415 EV 1

COMPUTER DISPLAY OF A Λ^{o} + 3 GAMMA RAYS EVENT

Abstract

This thesis is a preliminary account of work carried out to examine the characteristics of the isospin $I = 1$ and $I = 0$ channels

$$K^-p \rightarrow \Lambda^0 \pi^0$$

and $K^-p \rightarrow \Sigma^0 \pi^0$ at primary momenta between 150 and 480 Mev/c.

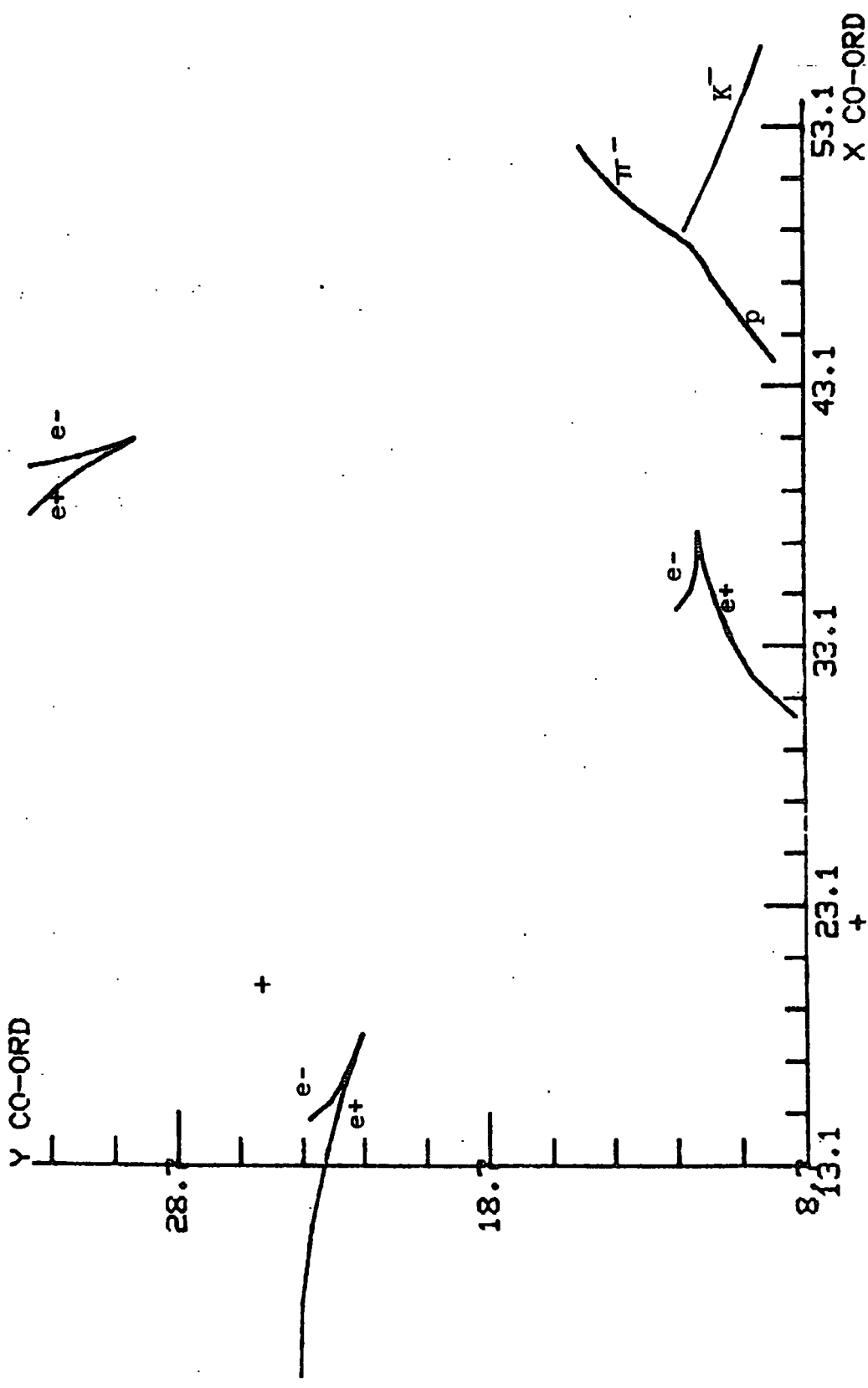The experiment used the British National Hydrogen Bubble Chamber at the Rutherford Laboratory with a Track Sensitive Target configuration, which provided gamma ray detection.

Two approaches are adopted to separate these normally ambiguous channels. The first is a statistical separation of the kind used by previous workers, the second uses the gamma ray detection of the Track Sensitive Target to resolve these two channels directly. The results of the two methods are compared and are in good agreement. The presence of the $\Lambda(1520)$ is clearly demonstrated in the determination of the branching ratio of $K^-p \rightarrow \Lambda \pi^0$ to $K^-p \rightarrow \Lambda^0$ + neutrals, as a function of momentum, and in the angular distribution of the Σ^0 in the K^-p centre of mass system. There is no evidence for the $\Sigma(1480)$ resonance.

CONTENTS

CHAPTER ONE

This thesis describes preliminary data on K^- meson
interactions with hydrogen, using a track sensitive target
inside a bubble chamber containing a hydrogen-neon mixture
for gamma ray detection. The aim of the experiment as a
whole, was to measure cross-sections for all channels
produced by K^- mesons below 500 Mev/c; the data presented
here is on the channels producing a Λ^0 hyperon and neutrals
for K^- momenta between 150 and 480 Mev/c. In particular
the momentum region 340 to 440 Mev/c, where most of the
statistics are available, is compared with the high statistics
experiments of refs 1.1 and 1.2, and the dominance of the
Λ (1520) clearly demonstrated. The statistics are low, but
it seemed worthwhile to check the data in a region that had
already been measured and to set up an analysis system for
use with the final data when assembled.

In Chapter 2 the basic bubble chamber and track
sensitive target are described, together with a brief descrip-
tion of the beamline. Chapters 3 and 4 describe the film
analysis chain adopted to provide the data discussed in
later Chapters. Chapter 4 also shows the selections made on
the data to provide a cleaner sample.

In Chapter 5, an analysis is shown using the missing
mass squared to the point Λ^0 fit and the channel branching
ratio to $\Lambda^0 \pi^0$ shown as a function of momentum. In Chapter 6
a method of maximum likelihood is used, to find the production
angular distributions of the $\Lambda^0 \pi^0$ and $\Sigma^0 \pi^0$ channels as a
function of momentum.
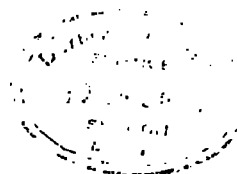
Feynman Diagrams of the s and t channels
for K⁻p interactions

s-channel
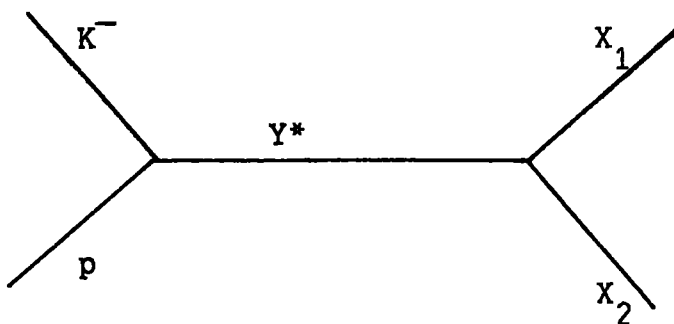
t-channel
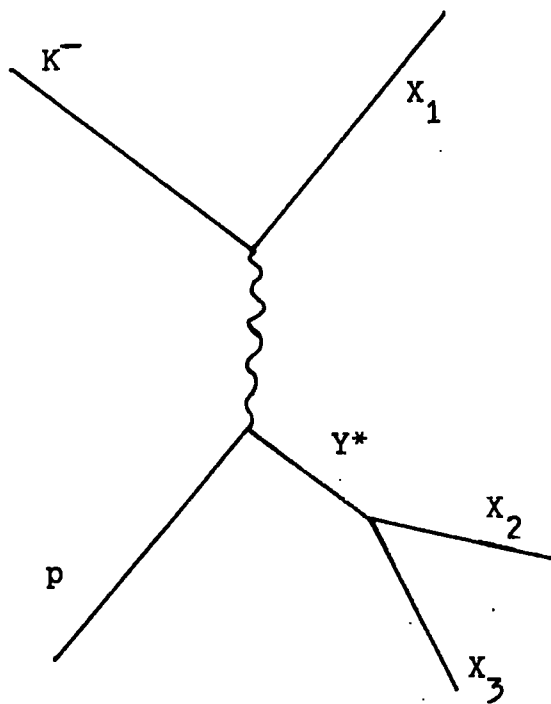
<u>Fig 1-1</u>

Chapter 7 shows these derived angular distributions compared directly with those obtained from $\Lambda^0\pi^0$ and $\Sigma^0\pi^0$ constrained fits using the Λ^0 + one seen gamma ray events and Chapter 8 presents the conclusions of these analyses in a short final chapter.

Appendices are attached with fuller derivations of some of the relationships used in the text.

The rest of this chapter gives some of the background to what is known about the low momentum K^-p interactions.

1.1 SURVEY OF LOW MOMENTUM K^-p INTERACTIONS

At low momentum the K^-p system can be used to form an intermediate Y* in the s-channel as opposed to the t-channel (see fig 1.1). However these low momentum K beams present difficulties and these are described in the following chapters.

Below 500 Mev/c there have been two high statistics experiments studying K^-p interactions refs 1.1 and 1.2 and a lower statistics experiment at zero momentum ref 1.3 . This region is dominated by the $\Lambda(1520)$ which decays predominately into $N\bar{K}$ and $\Sigma^0\pi^0$. Other Y* resonances have been claimed in this region notably the $\Sigma(1480)$ ref 1.4, however the evidence for these is somewhat slender.

A Y* resonance has a particular isospin (0 (Λ), 1 (Σ)) most final state channels are a superposition of these e.g.

$\Sigma^+\pi^-$ is $\sqrt{1/3}$ [I = 0> + $\sqrt{1/2}$ [I = 1 > + $\sqrt{1/6}$ [I = 2 >

The I = 2 state cannot be present since the initial state

K^-p can only have $I = 0$ or 1 ($I_K = I_p = 1/2$), but any resonance Y* structure has to be unfolded from the superposition of the two isospin states 0 and 1. The neutral final states $\Lambda^0 \pi^0$ and $\Sigma^0 \pi^0$ are pure isospin $I = 1$ and $I = 0$ states respectively and offer cleaner channels to explore the excitation of Y* resonances. However kinematic overlap (see Chapter 5) presents a difficult problem of separating these channels. Other workers have resolved them statistically (as in Chapters 5 and 6)·

1.2 THE TRACK SENSITIVE TARGET CONCEPT

The concept of the track sensitive target is to detect gamma rays, so that a fit can be made to these channels directly. The experimental details are given in Chapter 2.

Λ^c + one seen gamma ray

$$\Lambda^0 \pi^0 \rightarrow \Lambda^0 \gamma \; (\gamma)$$

This gives a 1C fit to the unseen gamma ray where the $\gamma + \gamma$ mass is constrained to be that of a π^0 .

$$\Sigma^0 \pi^0 \rightarrow \Lambda^0 \gamma \; (\pi^0)$$

1C fit again with the combination Λ^0 + gamma ray mass constrained to be that of the Σ^0.

With one gamma, the $\Lambda^0 \pi^0$ should always fit, if this is the appropiate channel, the $\Sigma^0 \pi^0$ will only fit if the gamma is from the Σ^0 decay to $\Lambda^0 \gamma$.

Λ^0 + two seen gamma rays

$$\Lambda^o \pi^o \rightarrow \Lambda^o \gamma \gamma$$

This is now a 4C fit the gamma + gamma combination forming a π^o.

$$\Sigma^o \pi^o \rightarrow \Lambda^o \gamma \gamma (\gamma)$$

This gives a 1C fit to both :

a) one gamma combined with the Λ^o constrained to give a Σ^o, and the other gamma combined with an unseen gamma constrained to give a π^o.

b) both gammas constrained to give a π^o, with the missing gamma combined with the Λ^o to give a Σ^o.

At least two gammas are needed to ensure a fit channel.

In this thesis, there were only enough statistics to use the Λ^o + one gamma ray events (see Chapter 7), hence suppressing the statistics of the $\Sigma^o \pi^o$ channel with respect to the $\Lambda^o \pi^o$ channel.

CHAPTER TWO

In this chapter, the basic bubble chamber operation
is outlined, and this is followed by a description of the
track sensitive target, its specification for this experiment
and the various modifications for low momentum beams, together
with a brief description of the beamline itself.

2.1 THE CHAMBER

Figure 2.1 shows the plan view of the British National
Hydrogen Bubble Chamber with its surrounding magnet. Its
volume is 150 × 45 × 50 cms. The chamber is photographed
by three cameras positioned 1.4 metres away in the configurat-
ion of an isosceles triangle, which has a base (=height) of
480 ± 0.1 mm. The observable volume is 300 litres. This basic
chamber was modified to accept the track sensitive target
which forms the basis of this experiment. These modifications
only effect the normal operation of the bubble chamber in a
minor way and will be described in the next section.

The operation of the bubble chamber is complex in detail,
but its principle of operation is as follows.

The proton synchrotron, NIMROD, gives a timing pulse
30 ms before the beam arrives; this pulse is delayed, to
allow for the time of flight of the K^- beam and used to
trigger various pieces of equipment.

The expansion cycle is initiated at about 15 ms after
the timing pulse. The static pressure P_s of the liquid in the
chamber, which is higher than the vapour pressure P_v, is
decreased rapidly. (P_s in this experiment was 117.4 psia and

Plan View of B.N.H.B.C.

Beam Entrance
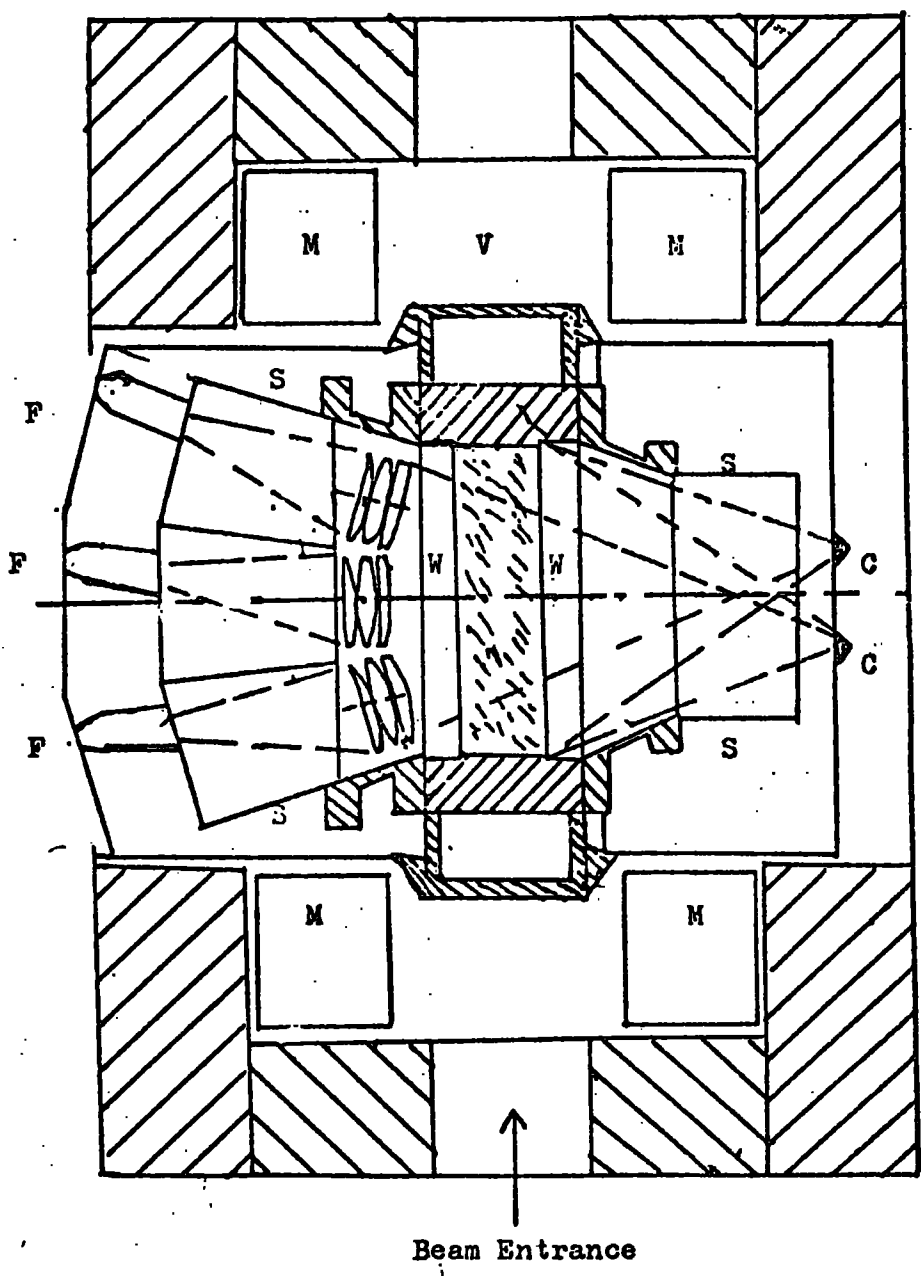
Fig 2-1

C= Camera
F= Flash
M=Magnet
S= Shield of Hydrogen
V= Vacuum
W= Window

Pv was 76.0 psia).

Ps falls below Pv and the liquid is now in its sensitive state, when charged particles will form tracks of bubbles. These bubbles form around the ions created in the superheated liquid by the passage of charged particles.

Ps continues to fall for a further 5 ms and the bubbles formed, are allowed to grow for 1 to 2 ms before they are photographed using electronic flash tubes. The pressure Ps is then reapplied, which collapses the bubbles and the chamber is ready for the next cycle.

The factors which are critical to the correct operation of the system include:-

a) If the expansion is not fast enough, the liquid will boil off the various surfaces raising the pressure above Pv again, resulting in the sensitive region not being reached.

b) If the reapplication of Ps is too slow, large quantities of the liquid will have been boiled off with result of even slower recompression as large amounts of vapour have to be liquified again.

c) If the flash tubes are fired too soon the resultant picture will have lost tracks due to insufficient bubble growth and tracks due to low momentum particles will lack enough bubbles per centimetre to produce reliable ionisation measurements.

A typical pressure-time curve is shown in fig 2.2.

The apparent size of the bubbles, determined from their images is about 250 microns in the chamber. This large size is due to the small apertures of the cameras, this produces a diffraction pattern (the Airy disk) which is the image on the
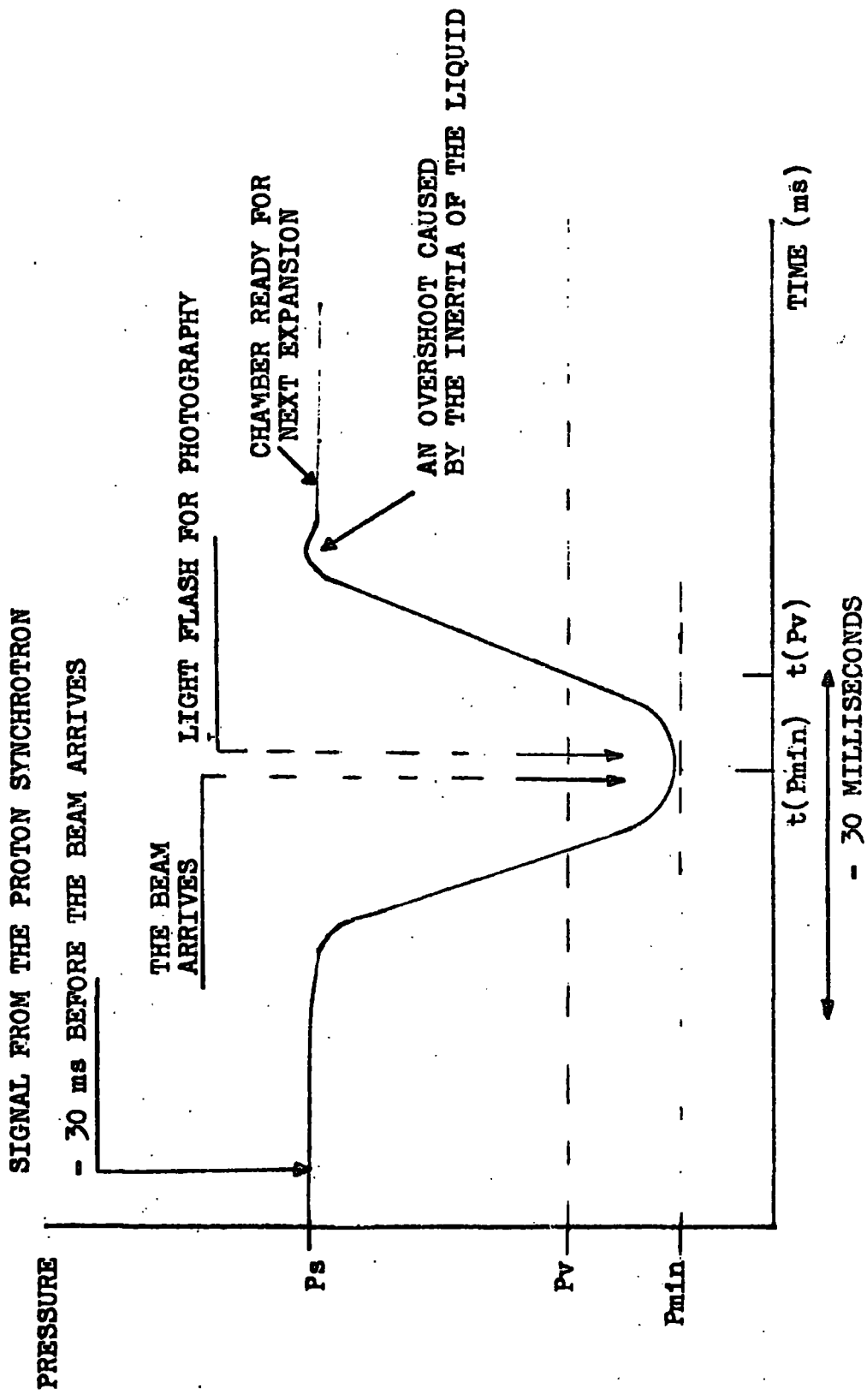
Fig 2-2

THE PRESSURE-TIME CURVE FOR A BUBBLE CHAMBER

photograph. The small apertures are required to ensure adequate focussing over the whole depth of the chamber.

2.2 THE TRACK SENSITIVE TARGET

The hydrogen bubble chamber is one of the most powerful tools available to the high energy physicist. Its main weakness is the long conversion length for gamma rays into electron-positron pairs($\approx$12.5 metres). Bubble chamber experiments have been performed with chambers filled with heavy liquids e.g. propane and freon with conversion lengths of 1.4 m and .14 m respectively, however the advantage of having a pure proton target for primary interactions is lost.

To overcome this problem the track sensitive target (T.S.T.) was developed. The system is shown schematically in fig 2.3 and in more detail in fig 2.4.

The T.S.T. is, in essence, two bubble chambers one inside the other and operating simultaneously. The operating temperatures and pressures of the chamber are chosen to make the hydrogen in the target volume and the mixture, in the outer simultaneously sensitive. It was because of the different temperatures of the two regions that a change in the normal operation of the bubble chamber had to be made, separate cooling loops had to be introduced to maintain the mixture and the hydrogen target at their optimum operating temperatures (found empirically). No separate expansion mechanism was provided for the target. The necessary expansion was achieved by a 1% change in the volume of the target, caused by pressure variations in the mixture being transmitted by the flexible

GAMMA RAYS CONVERT
TO e^+e^- PAIRS IN NEON
HYDROGEN

WALLS OF TARGET ARE OF 6mm PERSPEX

TRACKS PASS THROUGH
PERSPEX INTO CHAMBER

CHAMBER CONTAINS NEON HYDROGEN MIXTURE
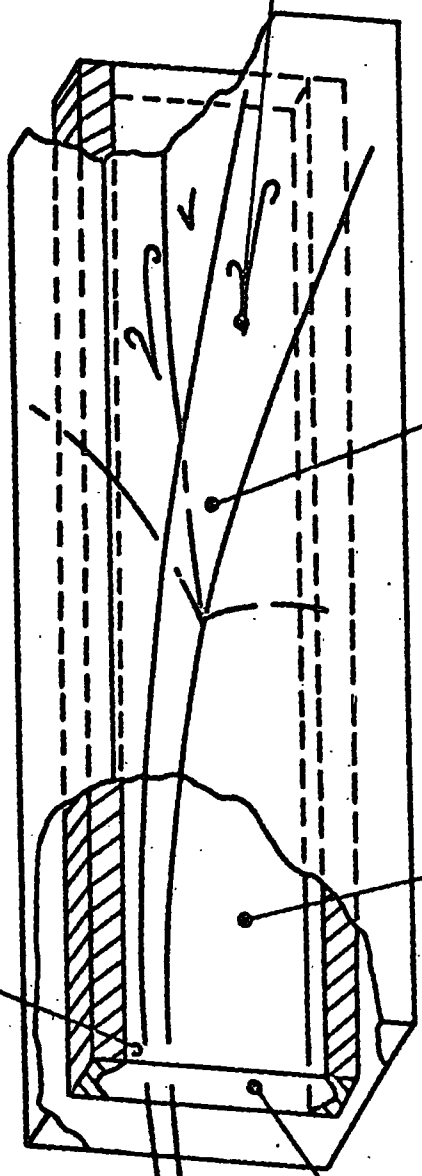
BEAM TRACKS
ENTER HYDROGEN
ONLY

TARGET
CONTAINS HYDROGEN

SCHEMATIC DIAGRAM OF TRACK SENSITIVE
TARGET

Fig 2-3

Perspex walls. The amount of wall deflection required to achieve the volume change, was 500 microns.

The mixture for this experiment was 78% Neon 22% Hydrogen by molecular weight. The conversion length for this mixture was about 0.40 m. This was not as good as one would have liked, but experimental conditions did not allow higher concentrations of Neon. As outlined in Chapter 1, this is essentially a Λ^o/Σ^o experiment and the target dimensions have to be commensurate with the decay length of the Λ^o at this momentum i.e. of the order of 10 cms. The target was eventually built with internal dimensions 135 × 33 × 7.5 cms (approx). This allows a large section of solid angle for gamma ray detection and a reasonable volume for primary interactions and short-lived secondaries, to be visible in the hydrogen target.

The optimum operating conditions were found by trial and error and eventually the temperatures were set at 29.5 ^{o}K for the hydrogen target and 29.8 ^{o}K for the hydrogen-neon mixture.

This produced fine tracks in the hydrogen and reasonable but denser tracks in the mixture. The denser tracks in Ne/H mixture are due to the higher ionisation loss of particles in these parts of the chamber.

2.3 BEAM ENTRY INTO THE CHAMBER

This experiment is investigating the low momentum region from 0 - 500 Mev/c K$^-$ interactions. At these low momenta the K$^-$ in the beam would decay over the length of the beamline to the bubble chamber. To overcome this problem, the beam was

PRESSURE TRANSDUCER

LOCATION PIN

BEAM EXIT WINDOW

SLIDE BRACKET

INFLATABLE GASKET

WINDOW

WINDOW LOCATION

INDIUM SEAL

CHAMBER BODY

VAPOUR PRESSURE BULB

COOLING LOOP

LOCATION SPIGOT

TARGET LIQUID SAMPLING LINE

FILLING VALVE

DUMP VALVE

INDIUM SEAL

BEAM

BEAM ENTRY WINDOW

SLIDE
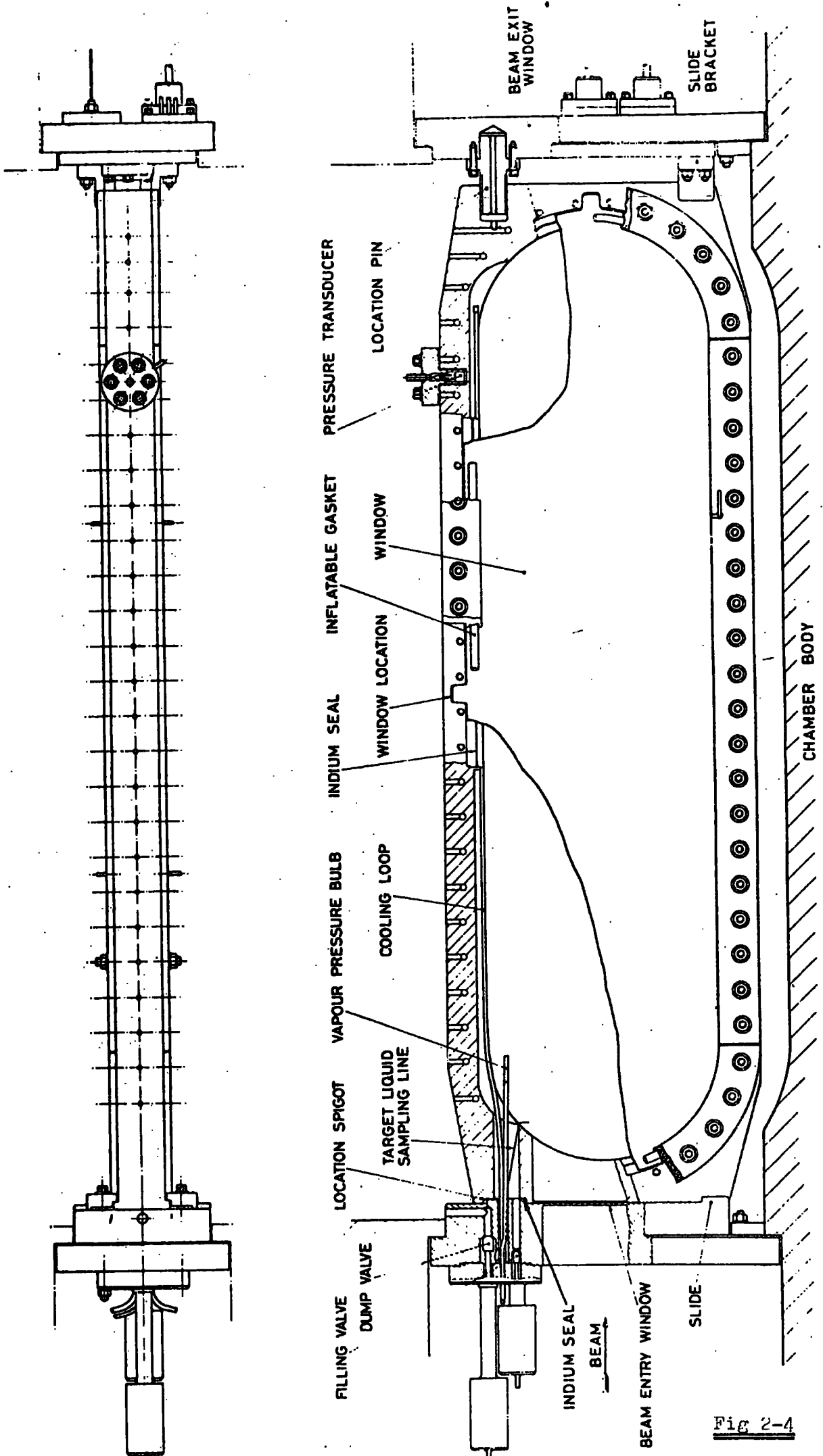
TRACK SENSITIVE TARGET FOR 1·5 METRE CHAMBER

Fig 2-4

transported at higher momenta (about 700 Mev/c) and before
the kaons entered the hydrogen target, they were slowed by
ionisation loss in a 30 cm aluminium degrader. However, even
with 700 Mev/c kaons, there is a problem with the bubble
chamber main magnet. The fringe field at the beam entry port
(see fig 2.1), is large enough to deflect these kaons away
from the chamber. In this region, a correction magnet had to be
inserted to counteract this effect. It was positioned to
allow the incoming kaons to be deflected upwards as the main
magnet deflected them downwards. The field of this magnet
was adjusted until the particles were travelling through the
degrader and into the chamber.

The side effects of the degrader were:-

a) a spread of momentum, which was not too large ($\Delta p = 50$
Mev/c), but it does mean that the beam momentum is not too
well-known;

b) a lot of neutral particles were produced in the degrader -
decaying or interacting in the chamber - giving a lot of
background. However this did not prove serious in practice
and it was found that beam contamination was of the order of
10%, mostly muons and pions.

2.4 THE BEAMLINE

The K19 beamline at the Rutherford laboratory, was used
for this experiment, a schematic diagram is given in fig 2.5.
The 7 Gev/c protons from the NIMROD proton synchrotron, struck
a copper target in which various interactions produced kaons
and other particles; these include pions and muons. The
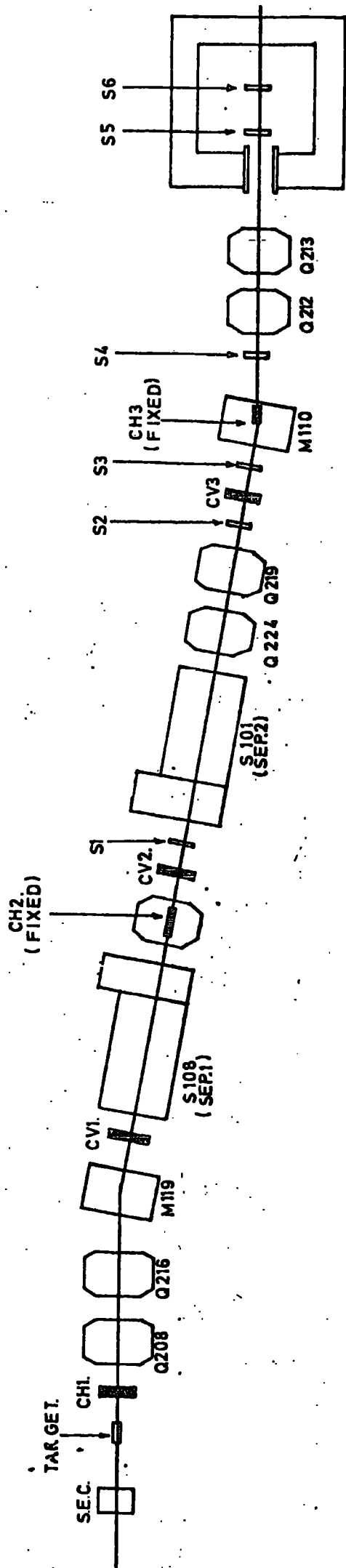
K19 BEAMLINE

Fig 2-5

number of protons per pulse was of the order of 6×10^{11}, producing on average about 30 kaons at the front of the degrader in the chamber, and about 10 entering the target.

The secondary emission chamber (S.E.C. in fig 2.5) gave a clear idea how well the proton beam was hitting the target by counting backward-going particles. This had the advantage of checking targetting but did not reduce the beam intensity.

The mixed beam of kaons, pions, muons etc., passed through a horizontal collimator into the first of two quadrupoles, the first focuses in the horizontal plane, the next in the vertical plane.

The beam was now comparatively narrow in the horizontal direction and mildly focussed in the vertical plane sufficient at least to enter the aperture of the first bending magnet. (M119 on fig 2.5) This is the first stage of momentum selection. Selection of momenta was achieved by the current setting of the first bending magnet and also the horizontal collimator CH2. Some momentum selection was also achieved by adjusting the quadrupoles, only the values around the central momenta were focussed on-to CH2. This momentum bite cannot be too small, otherwise there would be sizeable number of particles in the beam for further separation.

The beam was now ready for mass separation. This was done with electrostatic separators (S108 and S101 on fig 2.5). Electrostatic separators only work effectively below 5 Gev/c, as for much greater momenta, the velocity difference between different types of particles is insufficient. The electric field was vertical to the beam direction and the deflection

that the particles experience, depends on their velocity. As by this time all particles have approximately the same momenta, the result of the electrostatic separator was a mass separation. A particle mass bite was selected by the collimator CV2.

The above formed the basic units of the beamline. Subsequent stages involved further mass separation and just before entering the bubble chamber magnets, a further momentum selection (M110), as shown in fig 2.5.

2.5 THE EXPOSURE SUMMARY

The momentum range in the chamber covered in the whole experiment was about 0 - 500 Mev/c. In the exposure from which the present data is taken, some 433,000 pictures were obtained. This film was distributed equally between the four collaborating laboratories; Birmingham - Durham - University College, London. Each laboratory had film covering the whole momentum range.

The data presented in this thesis is the total currently available at Durham and represents 20% of the total film that was exposed. A summary of the run is given in table 2.1

TABLE 2.1

BLOCK NO.	ROLL NOS.	1000s FRAMES	APPROX NO. K/FRAME	APPROX. ENTRY MOMENTUM	APPROX. EXIT MOMENTUM
1	1-105	229	5	260	0
2	106-126	54	8.4	315	235
3	127-147	45	10.1	370	320
4	148-168	54	12.3	405	370
5	169-188	51	8.8	445	410

CHAPTER THREE

In this and the following chapter, the film analysis chain adopted to provide the data discussed later, is outlined. In all bubble chamber experiments, there has been established a well-defined structure of film analysis. This consists of scanning, measuring, geometric reconstruction and kinematic fitting to physical hypotheses. The details of each process are experiment dependent, although standard computer programs exist to handle the reconstruction and kinematic fitting of events. In the present analysis, the RHEL programs, GEOMETRY and KINEMATICS were used. The use of a T.S.T. introduced special requirements in the analysis chain and these are discussed in the next chapter. Since Durham's group approach is to extract data on all physical channels of interest in this experiment, the account in these two chapters is not restricted to those channels considered in detail later.

3.1 SCANNING

Scanning is the first step of film analysis. It involves looking at the film for various configurations of tracks which are characteristic of different types of physical channels. An initial step of this process is first deciding what to look for. In this T.S.T. experiment gamma rays can be detected and therefore any channels which can produce gamma rays are especially important.

At these momenta (0-500 Mev/c), there are six two body interactions which can be investigated, these are:

$$K^- p \rightarrow K^- p \qquad \text{elastic scattering}$$
$$\rightarrow K^o\, n \qquad \text{charge exchange} \quad (90 \text{ Mev/c})$$
$$\rightarrow \Sigma^+ \pi^-$$
$$\rightarrow \Sigma^- \pi^+$$
$$\rightarrow \Sigma^o \pi^o$$
$$\rightarrow \Lambda^o \pi^o$$
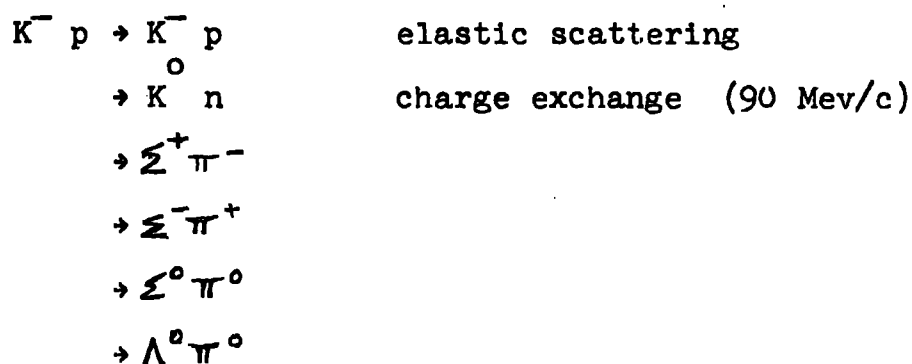
(the number in () is the threshold K^- momentum)

In addition there are the three body final states:

$$K^- p \rightarrow \Sigma^o/\Lambda^o \pi^+ \pi^-$$
$$\rightarrow \Sigma^o/\Lambda^o \pi^o \pi^o$$
$$\rightarrow \Sigma^- \pi^+ \pi^o$$
$$\rightarrow \Sigma^+ \pi^- \pi^o$$
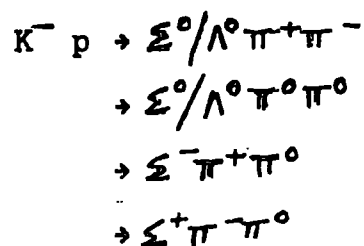
3.1.1 KAON DECAYS

As well as interacting, the K^- decays, mostly into $\mu^- \bar{\nu}_\mu$ and $\pi^- \pi^o$ but with a 5.59% branching ratio into the tau decay mode, $\pi^- \pi^- \pi^+$. This decay has the distinctive signature of three pion tracks at the primary vertex. (Ionisation of the pion tracks distinguish the tau decay from other three prong decays.) This makes it easy to see in scanning.

If one of the tracks for the tau-decay mode was less than 1 cm long and dark, the event was noted as probably being an interaction with an isolated neon atom (but was still subsequently measured). Throughout this experiment, there was a small seepage of neon into the target and hydrogen into the outer chamber. Events with four or more secondaries were all recorded as neon events. From these events it was possible to estimate the neon contamination of the target.

The number of neon events, of the order of 1%, indicated
that the contamination was low and that neon interactions
formed a very small background to the experiment.

3.1.2 ELASTIC SCATTERING

Elastic scatters are copiously produced in this momentum
region and to avoid flooding the measuring system (the next
stage of the process) with too many events to be handled in
a reasonable time, elastic scatters were only scanned for in
a subset of the rolls of film, giving reasonable statistics.
(Approximately 1000 elastic scatters were measured in each
momentum block.)

3.1.3 CHARGED SIGMAS

$$K^- p \rightarrow \Sigma^+ \pi^-$$
$$\rightarrow \Sigma^- \pi^+$$
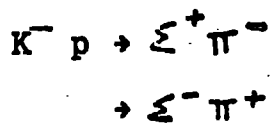
Followed by
$$\Sigma^+ \rightarrow p \pi^0, \; \pi^0 \rightarrow \text{two gammas}$$
$$\rightarrow n \pi^+$$
$$\Sigma^- \rightarrow n \pi^-$$

The charged sigma production can be divided into two categories,
those without the possibility of a gamma ray and those with.
In the latter, the only category is sigma+ production, in
which the sigma+ subsequently decays into a proton and a pi-
zero, the pi-zero in turn decays into two gamma rays.

The length of the sigma before decaying is of the order
of 5 mm. These events are very distinctive. The only significant
decay mode for the sigma- is to pi- and a neutron. The pion
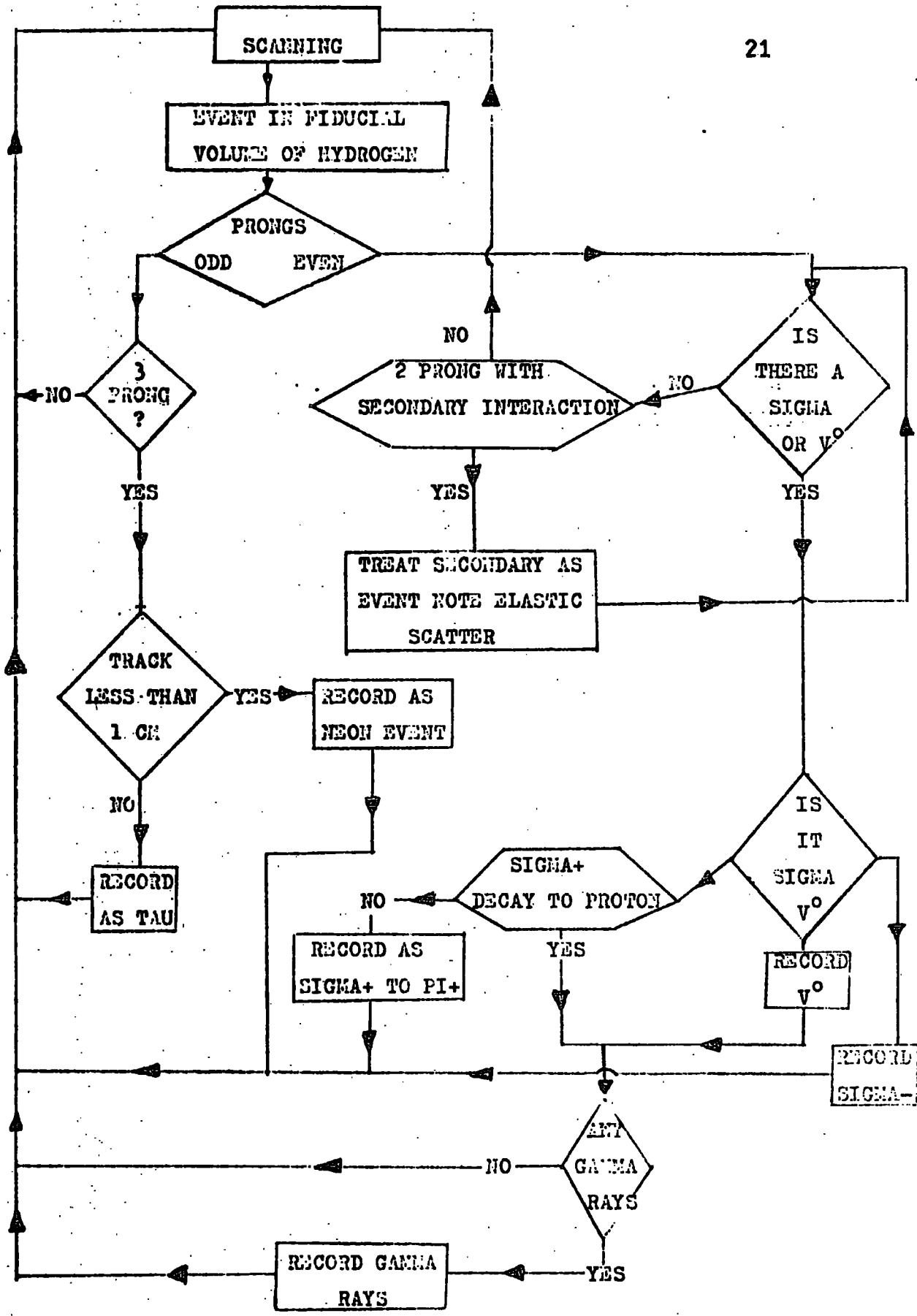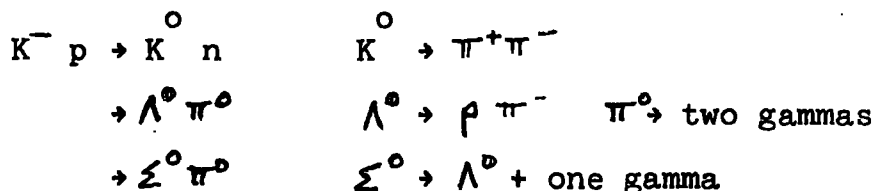track is usually light (in hydrogen) and long. It may pass

Fig 3-1

into the neon-hydrogen mixture, where, as explained in Chapter 2, it will form a darker track: Similiarly with the sigma+ decaying into pi+ and a neutron.

With a sigma+ decaying into a proton and a pi-zero, there are two possible signatures. The decay track of the sigma+,(the proton),is now darkish in the hydrogen (and if it gets into the neon-hydrogen mixture- black) and is usually only a few centimetres long. The second possible signature is an associated gamma ray. This gamma ray in the form of an electron-positron pair, is from the decay of the pi-zero. As the pi-zero decays very quickly (0.84×10^{-16} secs), the pi-zero decay vertex and the sigma+ decay vertex, are virtually identically located in the bubble chamber.

3.1.4 ZERO PRONG INTERACTIONS

These are interactions with an associated V^o.

$$K^- p \rightarrow K^o n \qquad K^o \rightarrow \pi^+ \pi^-$$

$$\rightarrow \Lambda^o \pi^o \qquad \Lambda^o \rightarrow p \, \pi^- \qquad \pi^o \rightarrow \text{two gammas}$$

$$\rightarrow \Sigma^o \pi^o \qquad \Sigma^o \rightarrow \Lambda^o + \text{one gamma}$$

One of the first problems to come to light with the zero prong interactions, was the large number of K^- tracks stopping in the Perspex walls of the T.S.T., with or without an associated V^o. In later analysis, a cut was made on the data to eliminate possible Perspex interactions producing V^o s in the hydrogen. (V^o s in the hydrogen-neon mixture were ignored.) To eliminate as many unassociated V^o s as possible, the V^o had to lie within a circle,radius approximately 10 cms of the zero prong. As explained in Chapter 1, this experiment
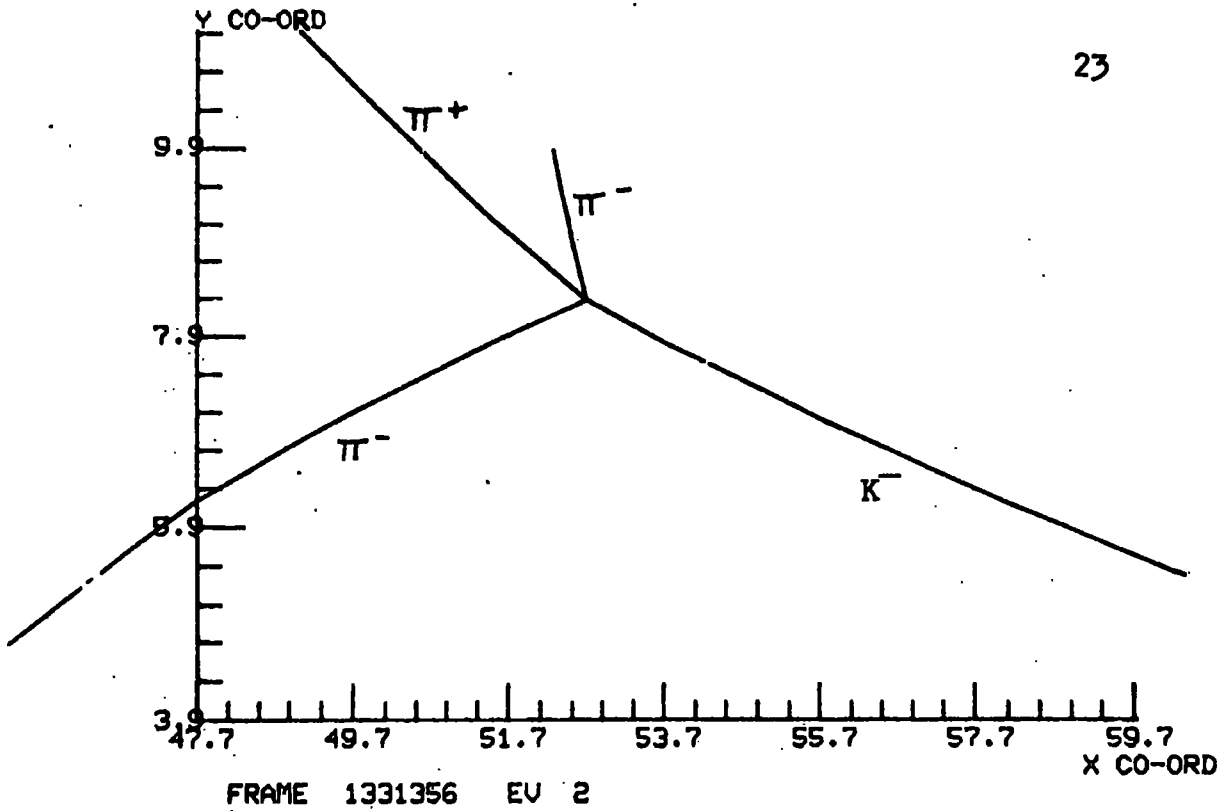
FRAME 1331356 EV 2

Fig 3-2

TAU DECAY
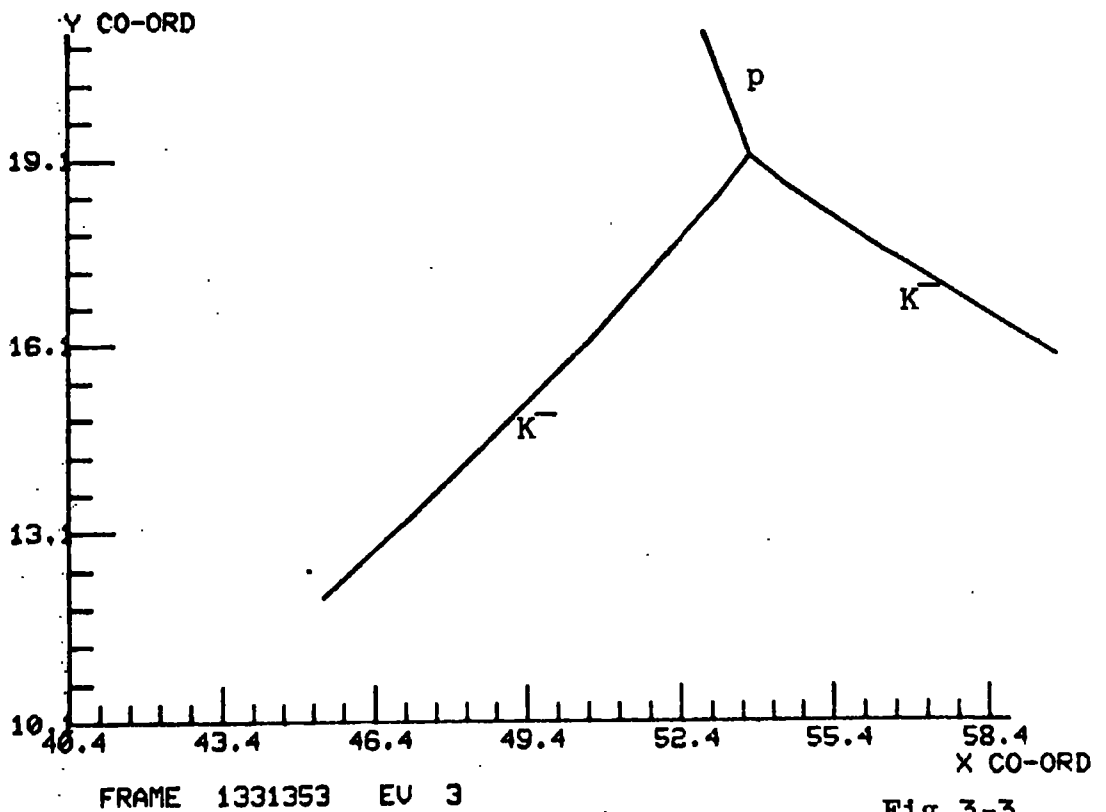
FRAME 1331353 EV 3

Fig 3-3

ELASTIC SCATTER

is primarily aimed at the Λ^o/Σ^θ ambiguity above, the only difference being the extra gamma ray from the Σ^o decay. A careful scan was made for gamma rays associated with V^o events.

Figs 3.2 to 3.5 show computer displays of various categories of actual measured events.

3.1.5 SCANNING PROCEDURE

A fiducial area was defined for the film from camera 2. Each hydrogen track was examined until it :-

a) left the hydrogen target (entered the Perspex walls and maybe subsequently the neon-hydrogen mixture)

b) left the fiducial area

c) interacted or decayed.

For (a) and (b) the track was ignored. For (c) the flow chart fig 3.1 was followed, resulting in interactions and tau decay modes being recorded.

3.2 SCANNING EFFICIENCIES

To evaluate scan efficiencies the film was double-scanned. (Some was triple-scanned). By comparison of the number of events which are common to both first and second scans (1/2), the number seen in the first scan only (1 $\bar{2}$) and the second scan only ($\bar{1}$ 2), the overall efficiency of scanning can be found:

If p_1 = probability of observing an event on scan 1

p_2 = probability of observing an event on scan 2

N_0 = actual no. of events on the film

N_1 = no. of events seen only on scan 1

FRAME 1331389   EV 1

CHARGED SIGMA   Fig 3-4

FRAME 1331387   EV 1

ZERO PRONG   Fig 3-5
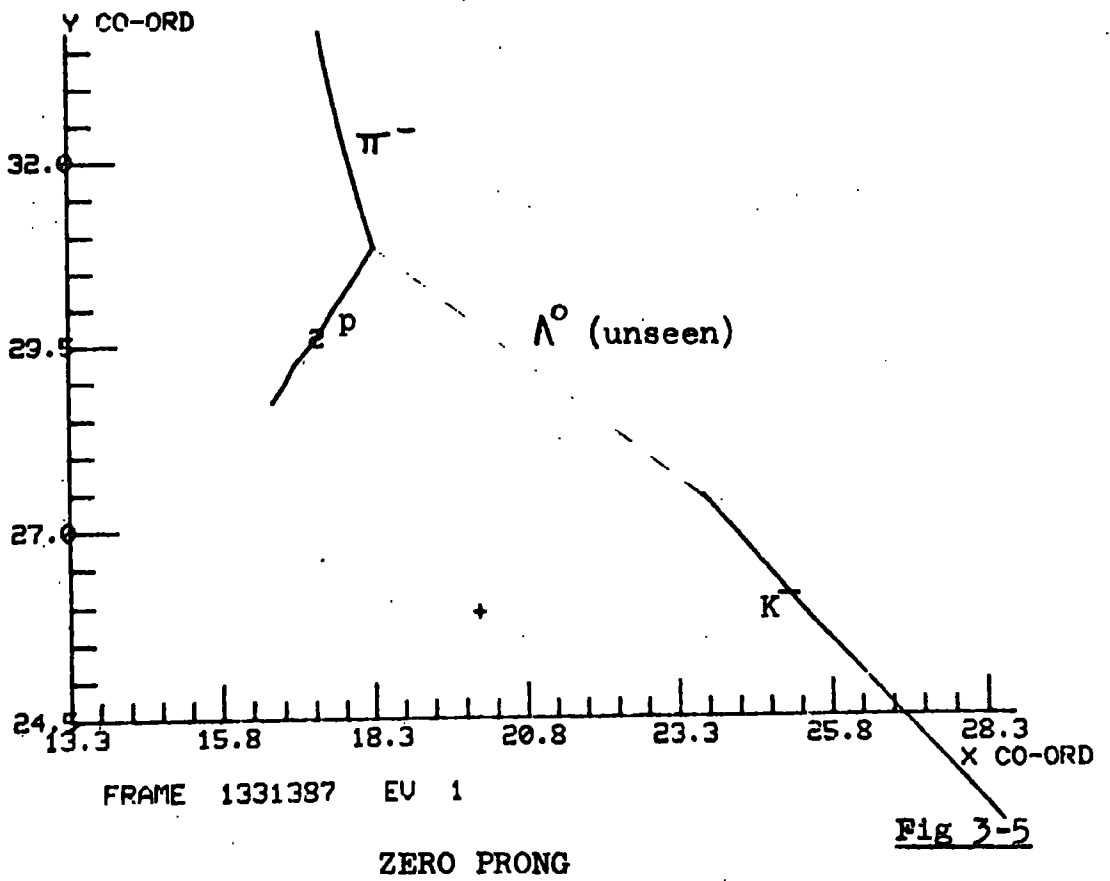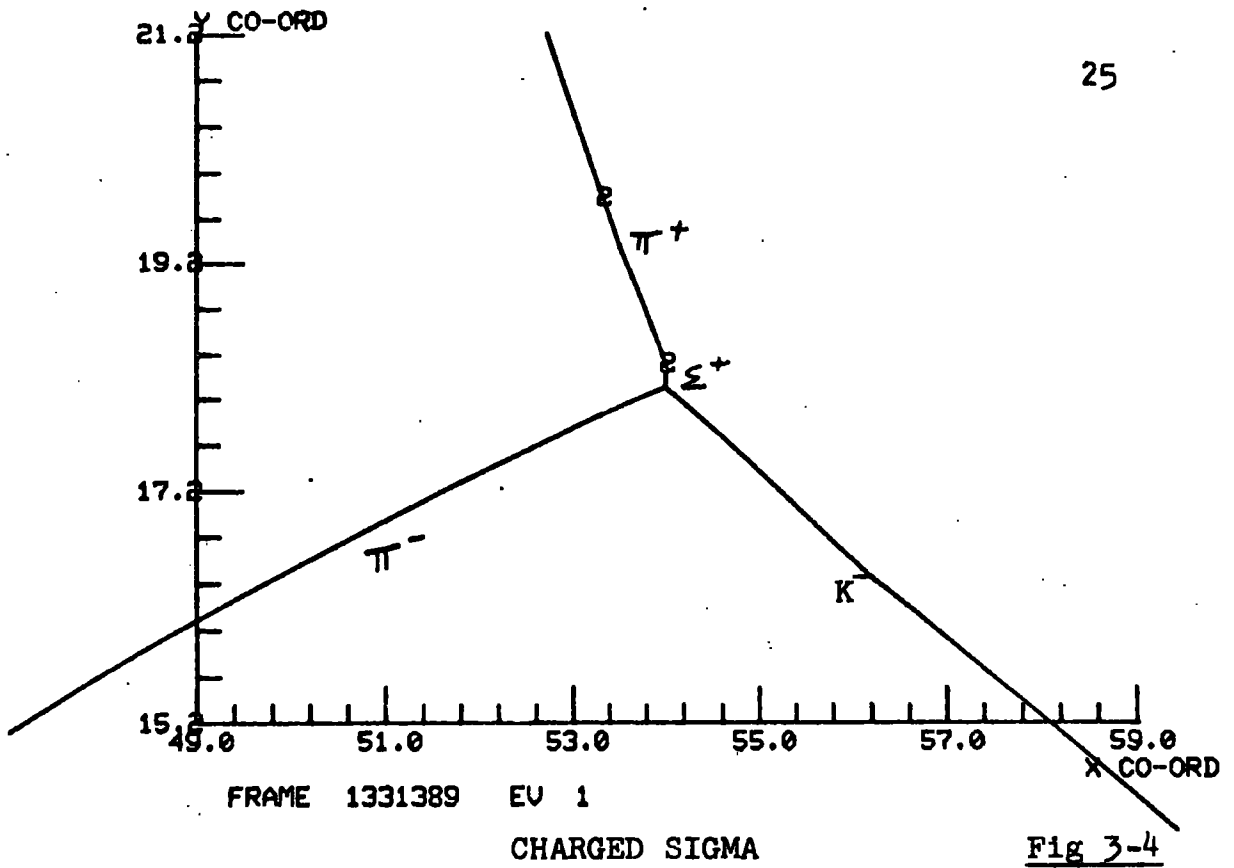
N_2 = no. of events seen only on scan 2

N_{12} = no. of events seen on both scans

then

$$N_1 = N_0 p_1 q_2$$

$$N_2 = N_0 p_2 q_1$$

$$N_{12} = N_0 p_1 p_2$$

where $q_1 = 1 - p_1$ and the scans are taken to be independent. This gives

$$p_1 = \frac{N_{12}}{N_2 + N_{12}}$$

$$p_2 = \frac{N_{12}}{N_1 + N_{12}}$$

$$N_0 = \frac{(N_1 + N_{12})(N_2 + N_{12})}{N_{12}}$$

The total efficiency of the two scans combined is

$$E_0 = \frac{N_1 + N_2 + N_{12}}{N_0}$$

Given in table 3.1 are various probabilities and over-all scanning efficiencies for various classes of events, on a sample from all momentum blocks. It must be emphasized that these efficiencies do not represent the total losses for any channel but just give an indication of the losses due to scanning.

TABLE 3.1 (ref 3.1)

CLASS OF EVENT	NO. OF 1/2	NO. OF ℓ 2	NO. OF 1 ℓ	p_1	p_2	E_0
SIGMAS	642	158	153	.81	.80	.96
V^0	510	183	178	.74	.74	.93
TAU DECAYS	264	58	41	.87	.82	.97

3.3 MEASURING CONSIDERATIONS

The programs,(described in the next chapter), which process the measured events, reconstruct them from the film plane of the camera and transform them into chamber space. The standard measuring system used in Durham,employs image plane digitizers, giving an accuracy of about 100 microns in the plane of the projected image of the film on the table. With a magnification factor of about 15, this transforms to approximately 7 microns in the film plane.

The transformation from image to film plane can be done analytically, and to demonstrate the number of consider-ations involved,(this is detailed below),in practice a poly-nomial of order 3 was used.

To transform the image produced by the projector back to the film plane, requires a very general approach to allow for all kinds of rotations and distortions of the image due to lens aberrations and the angled positions of the projectors.

Starting in the image plane, the following transform-ations are needed;

a) Change of origin of the co-ordinate system in the x,y plane (image plane)

$$x^* = x - x^o$$
$$y^* = y - y^o$$

b) a rotation through the angle Θ to align co-ordinate systems (see fig 3.6a)

$$\begin{pmatrix} x^* \\ y^* \end{pmatrix} = R(\Theta) \begin{pmatrix} x - x^o \\ y - y^o \end{pmatrix}$$

c) a rotation to allow for the projector tilt, see fig 3.6b. With the projection system used in this experiment, all tilts were in the y,z plane. This means in the projected image plane y is replaced by

$$y^{**} = y \cos \lambda$$

In general, if there is a tilt in the x,z plane of L, then the expression becomes:

$$\begin{pmatrix} x^* \\ y^* \\ 0 \end{pmatrix} = R(\Theta) \begin{pmatrix} 1 & 0 & 0 \\ 0 & \cos\lambda & \sin\lambda \\ 0 & -\sin\lambda & \cos\lambda \end{pmatrix} \begin{pmatrix} \cos(L) & 0 & \sin(L) \\ 0 & 1 & 0 \\ -\sin(L) & 0 & \cos(L) \end{pmatrix} \begin{pmatrix} x - x^o \\ y - y^o \\ z \end{pmatrix}$$

The z dependence is now included because the next transformation is the magnification M matrix, which is z dependent. The next D transformation is to allow for various lens distortions giving:

$$\begin{pmatrix} x^* \\ y^* \\ 0 \end{pmatrix} = R(\Theta).D.M(x,y,z).R(\lambda).R(L) \begin{pmatrix} x - x^o \\ y - y^o \\ z \end{pmatrix}$$

There is now one final rotation T and translation, to get the film plane transformed to the co-ordinate system of the fiducial marks of the chamber, recorded on the film, giving the overall expression as:
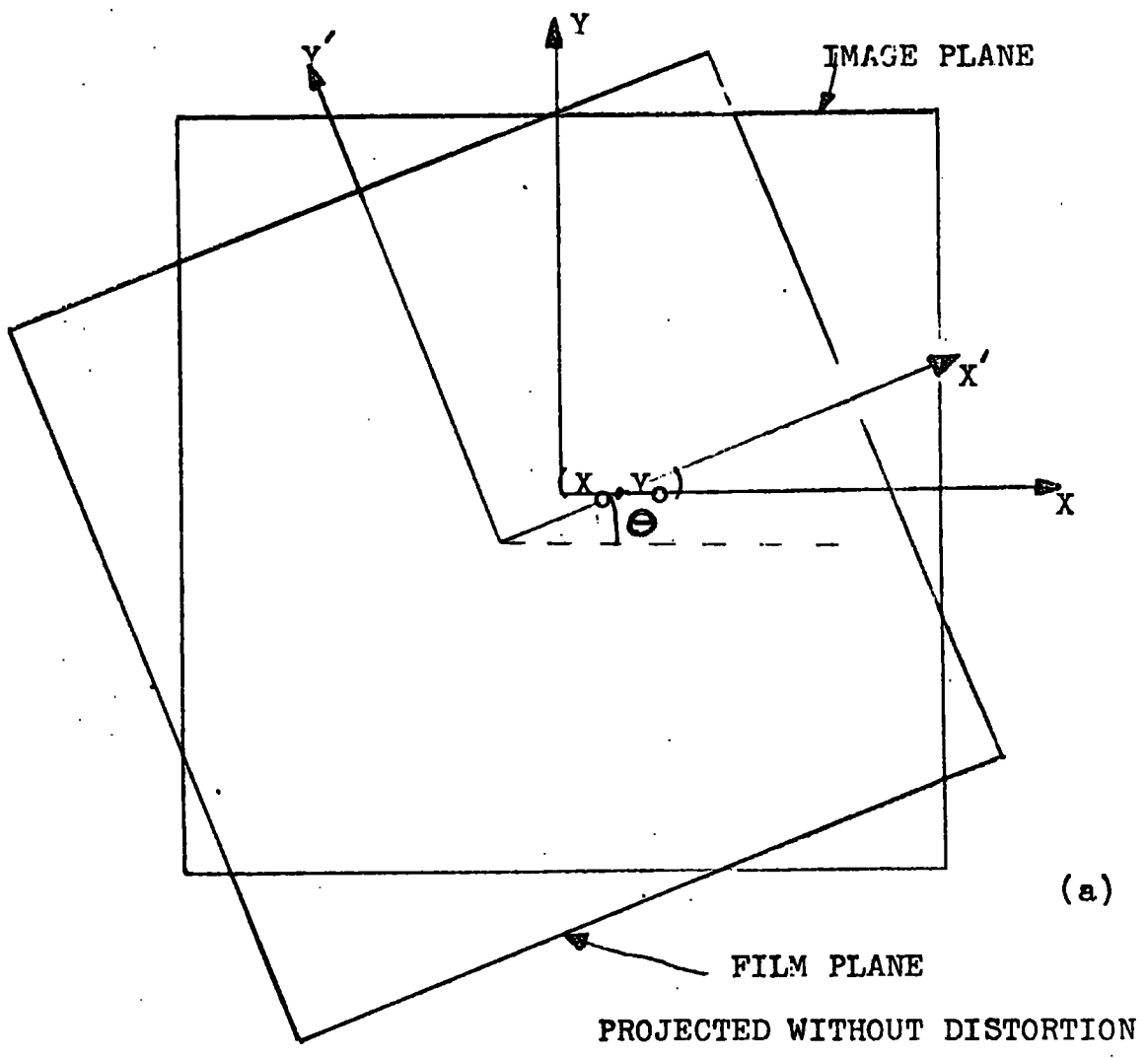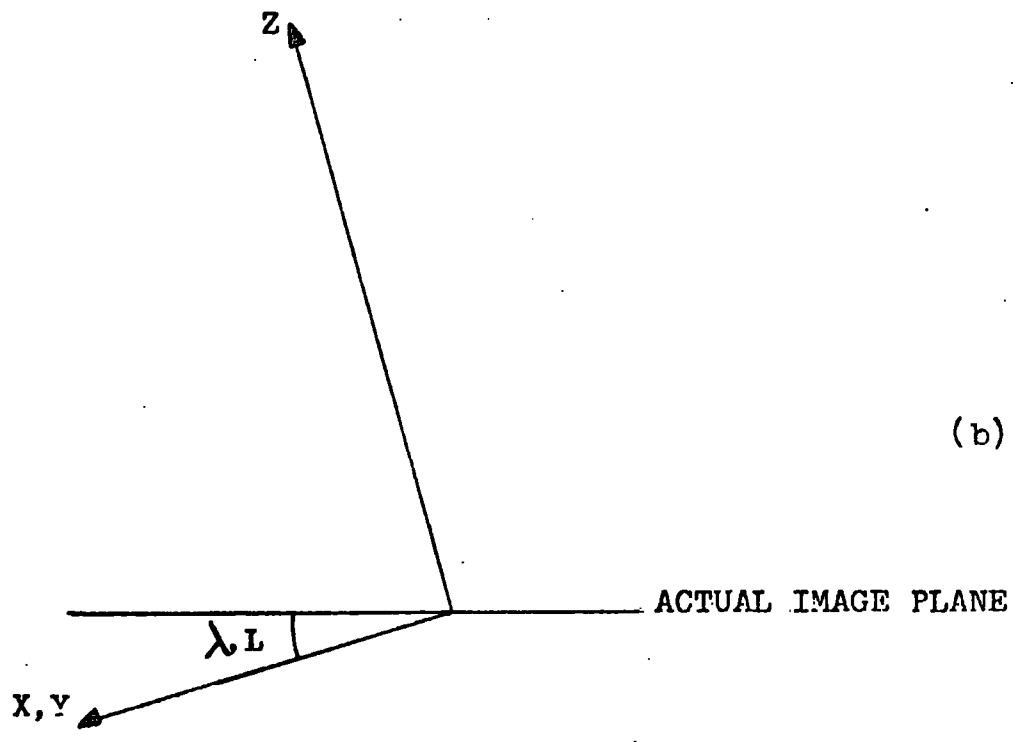
Y

Y′

IMAGE PLANE

X′

(X₀,Y₀)

Θ

X

(a)

FILM PLANE

PROJECTED WITHOUT DISTORTION

Fig 3-6

Z

ACTUAL IMAGE PLANE

(b)

λ L

X,Y

$$\begin{pmatrix} x^{**} \\ y^{**} \\ 0 \end{pmatrix} = R(T) . \left[R(\Theta).D.M(x,y,z).R(\lambda).R(L) \begin{pmatrix} x - x^{o} \\ y - y^{o} \\ z \end{pmatrix} - \begin{pmatrix} x_{f} \\ y_{f} \\ 0 \end{pmatrix} \right]$$

This produces in general a polynomial in each co-ordinate of the type:

$x^{**} = K + Ax + By + Cx^2 + Dy^2 + Exy +$ higher order terms,

with K, A, B, C, D, E, etc. as constants having different values for each co-ordinate. The constants were determined, using a least squares fit to measurements of the images of 20 fiducials on each view.

To ensure that this transformation was constant, i.e. the on-line system was measuring the co-ordinate system (defined by fiducial marks on the surfaces in the chamber) correctly, the whole projector system had to be rigidly fixed and tests built into the system to check that the projectors had not moved. This was achieved by measuring the distances between various fiducial marks on each view. If these distances were not within tolerance, the system was stopped until the projectors were back in line again.

The measurements were stored on a disk of an 1130 IBM computer. These were then transferred to the main processing chain. The transformation of these measurements into a form acceptable to the main processing programs (i.e. the film plane co-ordinates of each point measured) is achieved by programs called REAP and TRANS. It is here that the third order polynomial transformation is used on the data. The main programs of the processing chain are described in the next chapter.

CHAPTER FOUR

In this chapter the chain of processing programs is described briefly and the changes required by the T.S.T., and the gamma ray measurements discussed. This is followed by a discussion of event selection for subsequent analysis.

4.1 THE PROCESSING PROGRAMS

Having measured the events, the next step was geometrical reconstruction; this was achieved with a standard RHEL program called GEOMETRY. For a full description of this program see ref 4.1. The modifications due to the T.S.T. configuration had to allow for the three media in the chamber (hydrogen, Perspex and the hydrogen-neon mixture) and the bremsstrahlung radiation of the electrons in the hydrogen-neon mixture.

The three media in the chamber were corrected for by optical calibration programs (MONGOOSE ref 4.2) suitably modified and three separate range-momentum tables were constructed to allow for energy loss (swimming) of particles along their tracks through all three media. To indicate that a track was being measured into the hydrogen-neon mixture the last point in the hydrogen was measured twice. (Hence the figure 2 on the computer displays of events shown in chapter 3). Apart from this the two sections of the track were measured in the normal way.

Some modifications were necessary for utilising measurements on electron-positron pairs (i.e. gamma rays). These modifications were in line with those normally used in

heavy liquid bubble chambers. In geometric reconstruction,
use was made of the slowing down corrections for particles.
For hadrons, this allowed for the ionisation loss. For elect-
rons, bremsstrahlung is an important extra reason for energy
loss.

As a preliminary to more elaborate reconstruction
methods for gamma ray momentum and angles, a gamma checking
procedure was incorporated into the program. This was initially
established to determine which vertex the gamma ray pointed
to, but finally included other checks.

First the e+ e- tracks were swum to the vertex(i.e.
reconstructed taking into account energy loss) and a check
was made on the compatibility of dip and azimuth angles of
the two tracks- here some e+ e- pairs failed and the gamma
ray was deleted from the event record.

Secondly the e+ e- momentum vectors were vectorially
added to define a gamma direction and momentum. This direct-
ion was then compared with that obtained from the line
joining the production and materialisation vertices of the
gamma. In the case of two possible production points, the
correct one was taken as that for which the two directions
agreed best. The quantity X(=sum of differences of angles
squared, divided by sum of differences of errors squared -
a pseudo-chis squared) was used as a quantitative measure
of agreement and it was empirically decided that if $X > 20.0$,
the measured gamma ray was unlikely to be really associated
with the presumed origin. The final direction of the gamma
was taken as a weighted mean of the two above estimates.

For the kinematic fitting of hypotheses to physical
channels, the RHEL program KINEMATICS was used. This is
described in refs 4.3 and 4.4 . This program did not require
extensive modifications due to the T.S.T. arrangement
because GEOMETRY provided all momenta and angles in the
hydrogen target for the tracks. (Except for electron-positron
pairs, where it provided the gamma ray track, see above).
Therefore the tracks can be considered to be those of a
conventional hydrogen bubble chamber experiment.

4.2 BOOKEEPING AND DATA SUMMARY TAPES

The bookeeping for this experiment was achieved by a
system called MASTERLIST. This consists of a large set of
files containing an entry for each event found in scanning.
Each entry consists of 20 parts giving frame and number of
event in the frame, a status word indicating what stage
of processing had been reached with this event and the fitted
hypotheses. This entry is a summary of the event and was used
to control the writing of the Data Summary Tape. (see below)

Having scanned, measured, reconstructed and fitted the
events to some physical channels, the next stage was to look
at them again and reconsider them in the light of the
measurements and the physical channels, if any, that have
been fitted. This stage is known as Judging. Only certain
classes of events were judged, others were considered accept-
able, if they had fitted only one physical channel and it was
clear that no further information would be gained. An example
of this category were the unambigious $K^- p \rightarrow \Sigma^- \pi^+$ interactions.

All V^o events were however judged, irrespective of their status after the first measurement.

During judging, a further detailed scan was made for gamma rays in connection with those events which fitted the possible gamma ray producing channels (see section 3.1). Any events found at this stage with associated gamma rays , were put back into the remeasure chain. Likewise all events considered to be improperly fitted and all events which fail to reconstruct, were also put into this chain.*

Those events considered to be satisfactory were given a status word on the MASTERLIST which sets the event as completely processed. In order to facilitate the analysis of the events in terms of physics, it was necessary to form a Data Summary Tape (D.S.T.). The control of this process was done by MASTERLIST, which only allowed the accepted (by judging) fitted hypotheses for each event to be written on to the D.S.T. The data used in this thesis was from the first measure. As can be seen in Chapter 7 there are very low statistics in $\Lambda^o + \gamma$ channels. This is partly due to the large fraction of associated gamma events in the remeasure chain.

The variable length record for each event on the D.S.T. contains: the x, y, z co-ordinates for all vertices, unfitted (GEOMETRY) and fitted (KINEMATICS) values of the momentum, dip angle, and azimuth angle for each track, together with each track length, and at the end of each record a summary of the information on MASTERLIST. (see Appendix for sample D.S.T. record) The D.S.T. records were processed using a program which incorporated HYBRID (see ref 4.5 for flow chart

* As a result 60% of the Durham point Λ^o events are used at present.

and HYBRID facilities).

The basic structure of HYBRID was extended and incorporated features for easy handling of the D.S.T. record outlined above. The run cards selected up to 6 hypotheses from KINEMATICS fitting and stored a summary of each in specified locations. Similiarly particular tracks (selected by masscode) were specified and loaded into the HYBRID p-vectors, the default was fitted track variables, measured variables were loaded, if subroutine GOBACK was called in the user subroutines. In addition, centre of track or vertex quantities were selected by run cards.

Also incorporated were various subroutines which extended the HYBRID facilities. These included a statistics package, which gave the moments of a distribution of variables, a facility for concatenation of D.S.T.'s with different run cards for each, and the option to produce GRAPHICS (see ref 4.6) plots in addition to the normal HYBRID plots. This last facility has produced most of the plots for this thesis.

All **minimising** procedures used subsequently used MINUIT (see ref 4.7).

4.3 D.S.T. EVENT SELECTION

After the events have been written on to a D.S.T, it is important to select a sample which will be clear of the more obvious biases . The remarks in this section are confined to the $K^-p \rightarrow \Lambda^o$ + neutrals channels as these are to be considered in more detail in the following chapters. The data discussed below comes from the kinematic fit of the Λ^o, constrained to

have its momentum vector pointing to the end of the K^- track (point fit, normally a 3 constraint fit). Fig 4.1 shows the distribution of momenta of the K^- beam track at the interaction vertex for all $K^-p \to \Lambda^0 +$ neutrals channels. The total number of events in this plot is 2000. It can be seen that there is a very large spike at zero momentum and similiarly in fig 4.2 a large spike close to zero momentum , the Λ^0 momentum distribution. This is unlikely to occur in practice because a very low momentum Λ^0 has such a low mean free path for decay that it will look like a two prong event in the chamber, and therefore would not be in the datasets under discussion.

The χ^2 fit probability distribution is shown in fig 4.3 and the z co-ordinate distribution of the interaction vertices in fig 4.4 In the probability distribution, which should be flat, there is a large spike in the bin 0.0 to 0.01, indicating that events have been included which do not belong to the $\Lambda^0 +$ neutrals channels. A probability cut was made at 0.01.

The z co-ordinate distribution has large peaks at the extreme ends. These are due to interactions in the Perspex walls of the T.S.T.,which as can be seen,copiously produce Λ^0 events which have to be excluded because the target in this case is not pure hydrogen. The ends of this distribution are not sharp due to errors of measurements, which in GEOMETRY reconstruction produce errors in z. The z cut used in this analysis was to take events lying between $19.8 \leqslant z \leqslant 26.8$ cms. This effectively excludes 0.5 cms of T.S.T. at each Perspex interface.
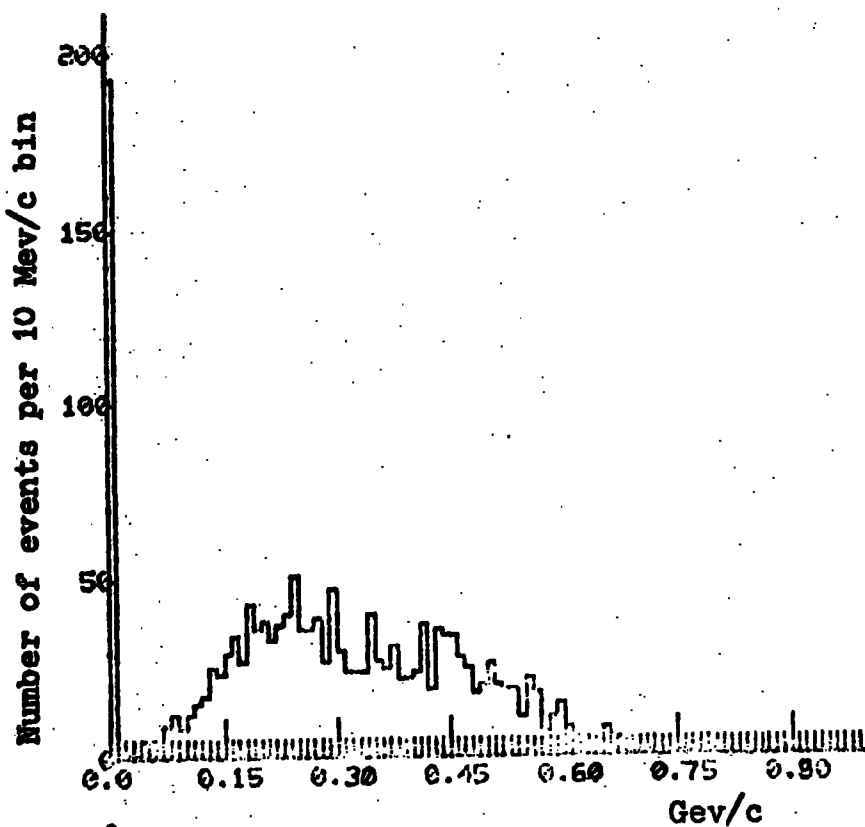
The results of these cuts are shown in figs 4.5 to 4.8. Fig 4.5 shows that the large spike at zero K^- momentum has been greatly decreased and in fig 4.6 the very low momentum Λ^os have been removed. The probability distribution, fig 4.7, is now reasonably flat, though there is still an excess below 0.05. The z distribution is shown in fig 4.8.

Fig 4.5 still shows a spike at zero momentum and a subsiduary peak at 120 Mev/c. Events below 150 Mev/c were simulated by a Monte-Carlo program generating Gaussian distributions of momenta at the centre of track and these produced highly asymmetric distributions of momenta at the vertex, events were either at zero momentum or in a peak around 120 Mev/c.

Such skew distributions at the vertex would lead to non-Gaussian errors on the missing mass squared which is used in Chapter 5 and 6, and hence invalidate the analysis carried out there. Hence the events below 150 Mev/c have been excluded from the analysis. They are predominately due to interactions of K^- mesons at rest.

Of the original 2000 events, 1560 had a K^- momentum above 150 Mev/c, after the probability and z cuts, 1057 events were used in the subsequent analyses.

At this low momentum K^o/Λ^o ambiguity was mainly resolved by judging the events and the remaining ambiguities, some 20 events, were left in the analyses which follow as Λ^o events.
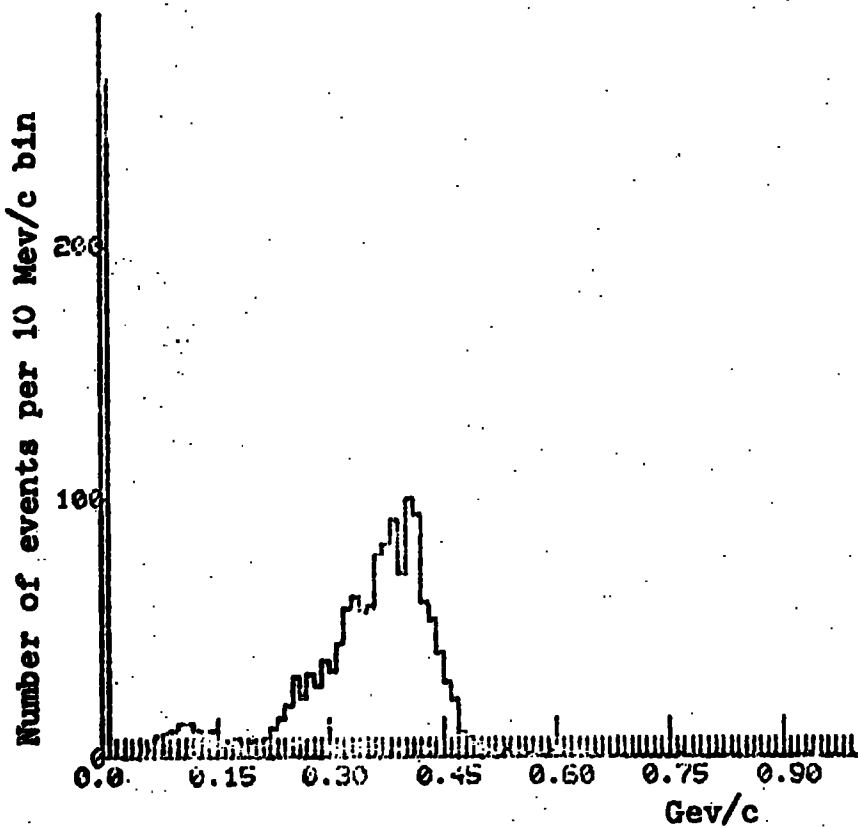
Fig 4-1

K⁻ Momentum distribution

Fig 4-2

Λ° Momentum distribution
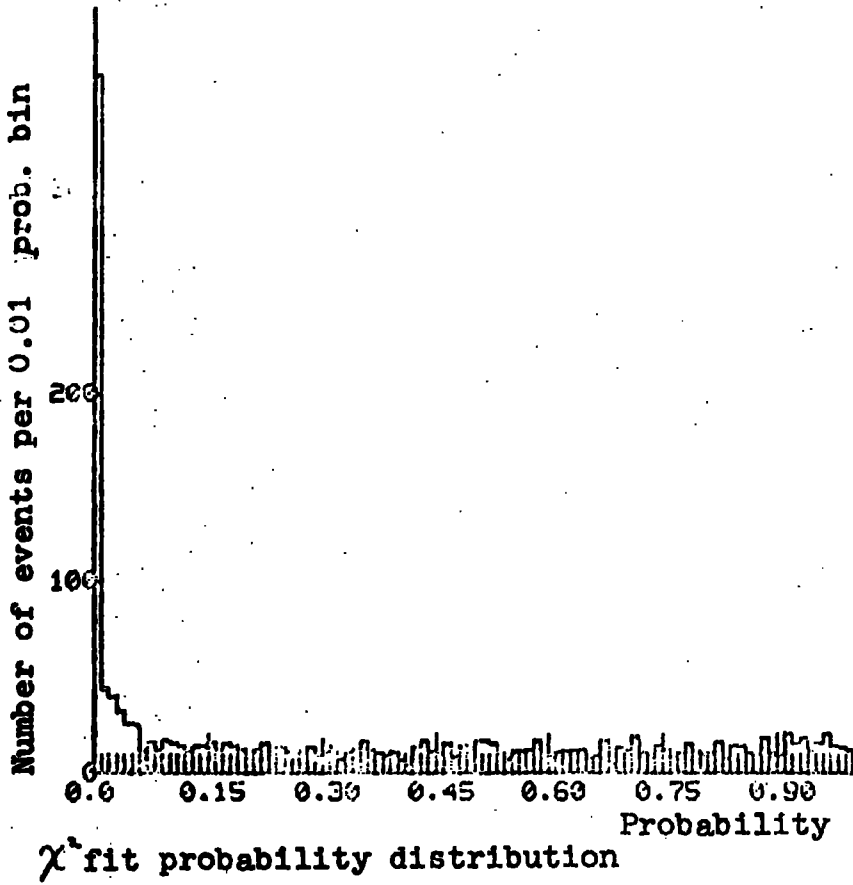
χ^2 fit probability distribution Fig 4-3
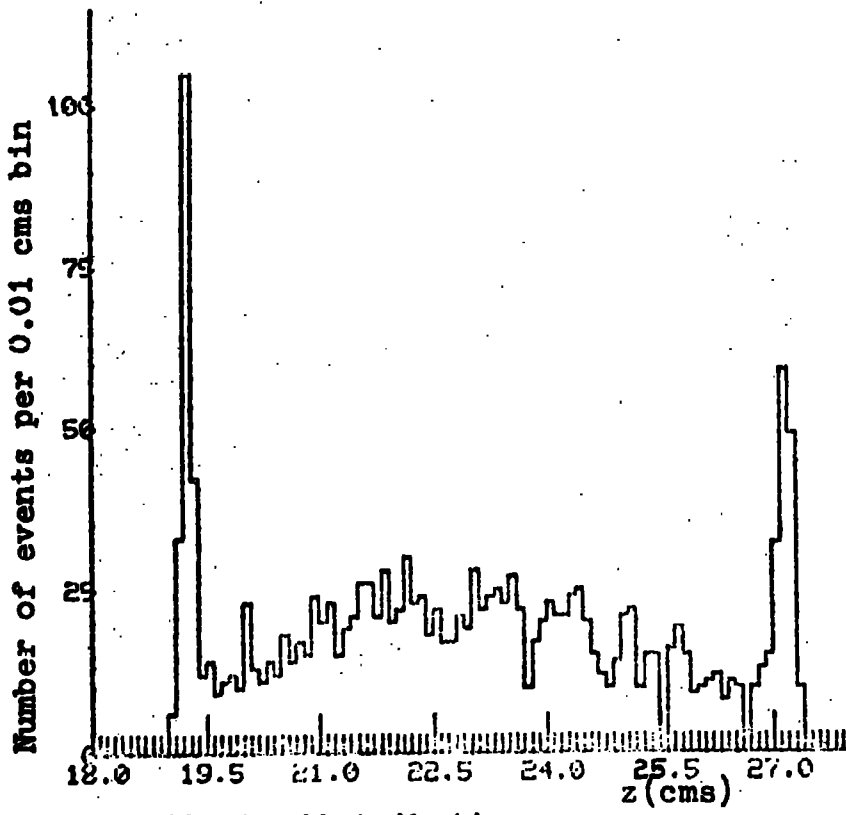
z-coordinate distribution Fig 4-4
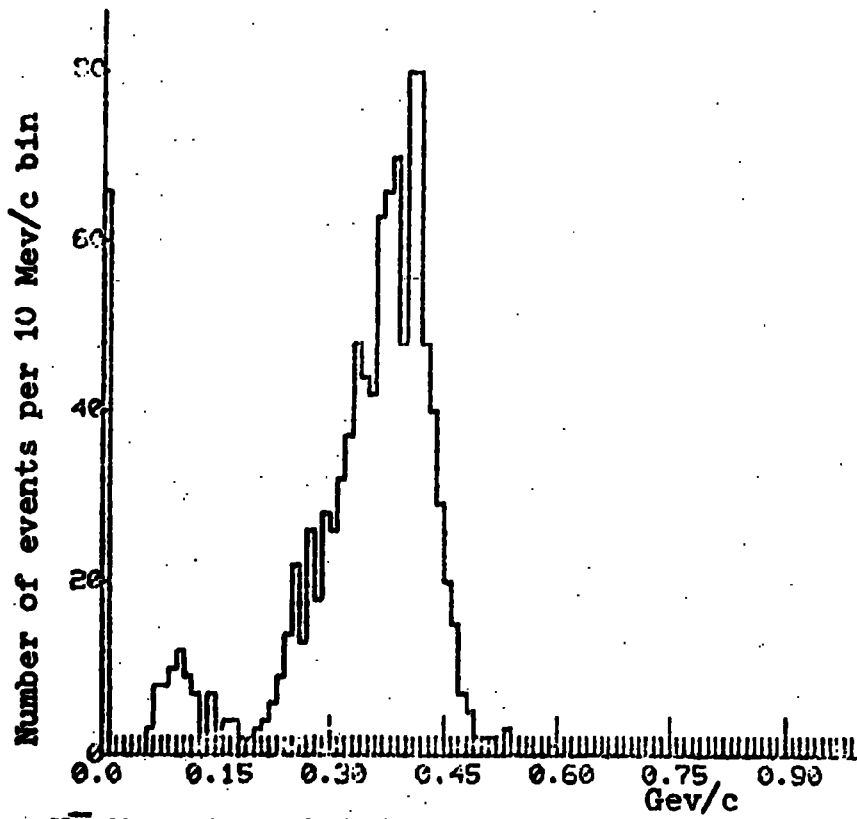
Fig 4-5

K⁻ Momentum distribution
with cuts
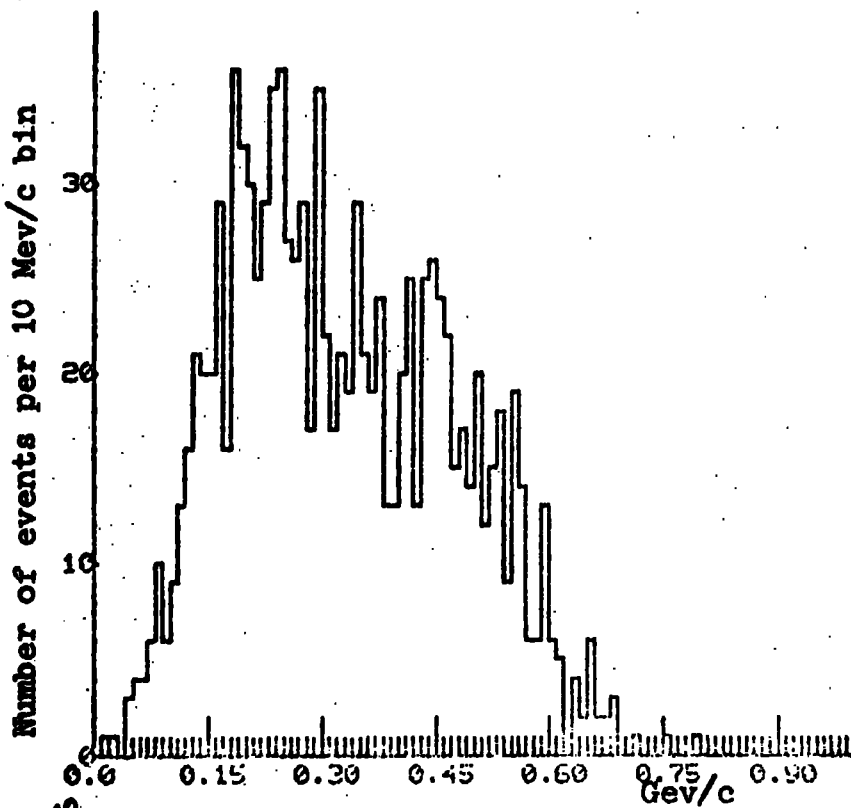
Fig 4-6

Λ° Momentum distribution
with cuts
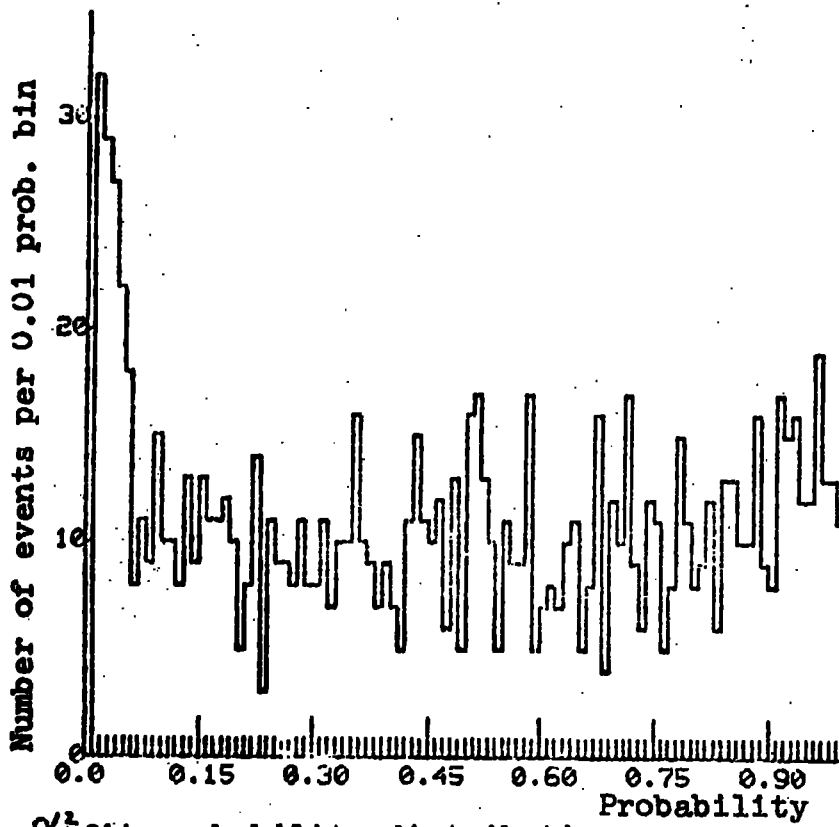
Fig 4-7

χ^2fit probability distribution
with cuts

Fig 4-8

z-coordinate distribution
with cuts

CHAPTER FIVE

The main aim of this experiment, as described in Chapter 1, is to separate the $\Lambda^0\pi^0$ and $\Sigma^0\pi^0$ channels as a function of momentum and determine their differential cross-sections. As pointed out in Chapter 3, the $\Lambda^0\pi^0$ and $\Sigma^0\pi^0$ channels have an identical appearance in a hydrogen bubble chamber - that of a single V^0 pointing to a K^- track ending in the chamber. With the T.S.T. there is the chance of gamma rays material- ising, which adds informa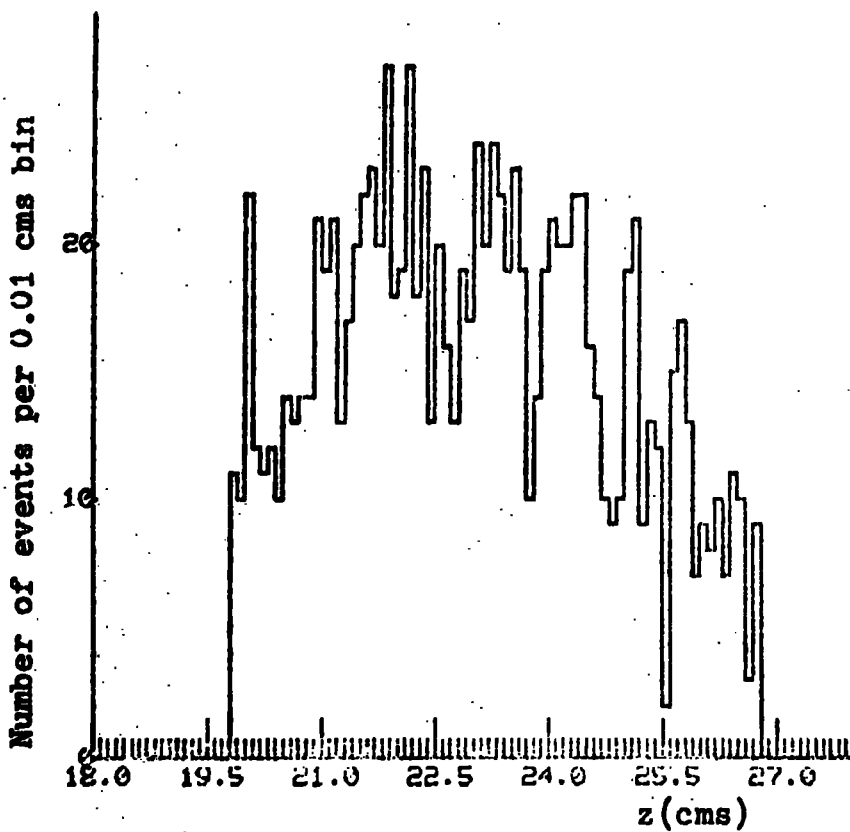tion to resolve the ambiguity, however if there is only one gamma ray and it comes from the pi-zero of the $\Sigma^0\pi^0$ channel a constrained kinematic fit is not possible. This combined with the low statistics of the $\Lambda^0\gamma$ and $\Lambda^0\gamma\gamma$ events available at the present time, does not allow full use of the data from gamma detection and the analyses which follow, use only the point V^0 fits to Λ^0 events. In Chapter 7, the $\Lambda^0\gamma$ events available will be used as a consistency check on the results obtained from the two methods that are described in this and the next Chapter.

One possible starting point for separating the two channels without using gamma information, was to accept all events which kinematically fit the $K^-p \rightarrow \Lambda^0\pi^0$ channel as genuinely belonging to that channel. However, there is considerable overlap between the kinematic regions belonging to the $\Lambda^0\pi^0$ and $\Sigma^0\pi^0$ channels, leading to erroneous separation of these channels by this method. (see below) As has been done in refs 5.1 and 5.2 only the information from the 3 constraint fits of Λ^0_S pointed to the K^- track endings, is used in the analyses presented in this and the next Chapter. A maximum
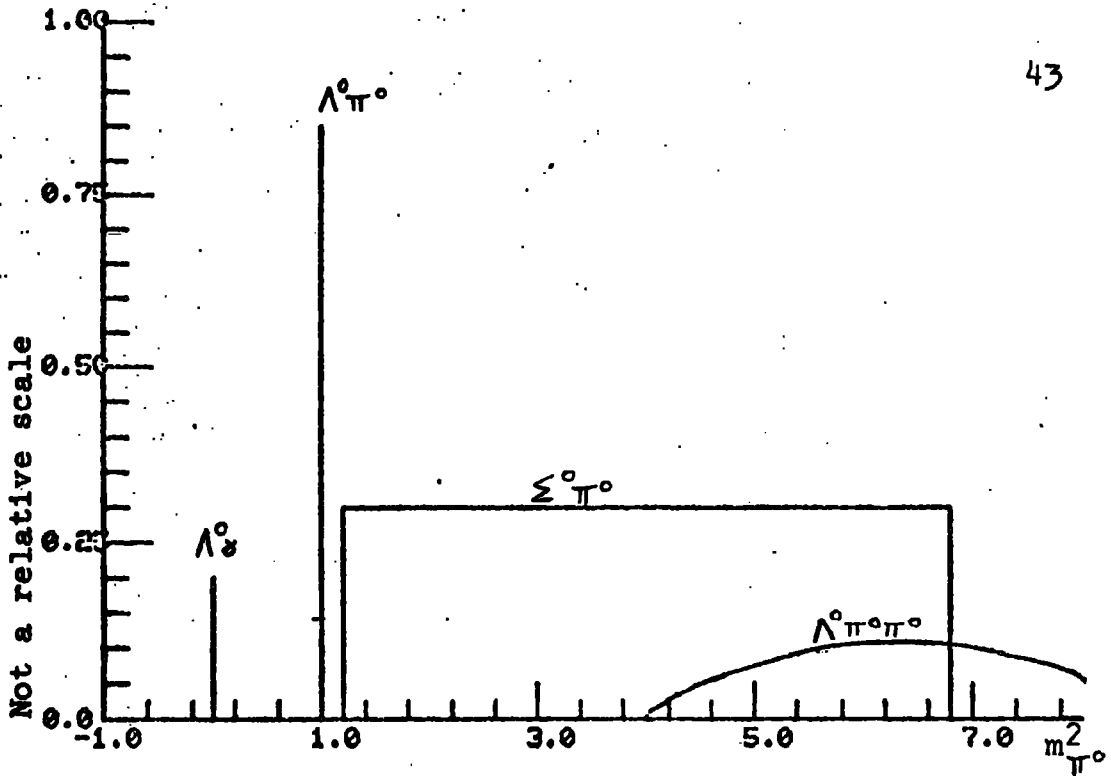
Theoretical MMSQ distribution

Fig 5-1
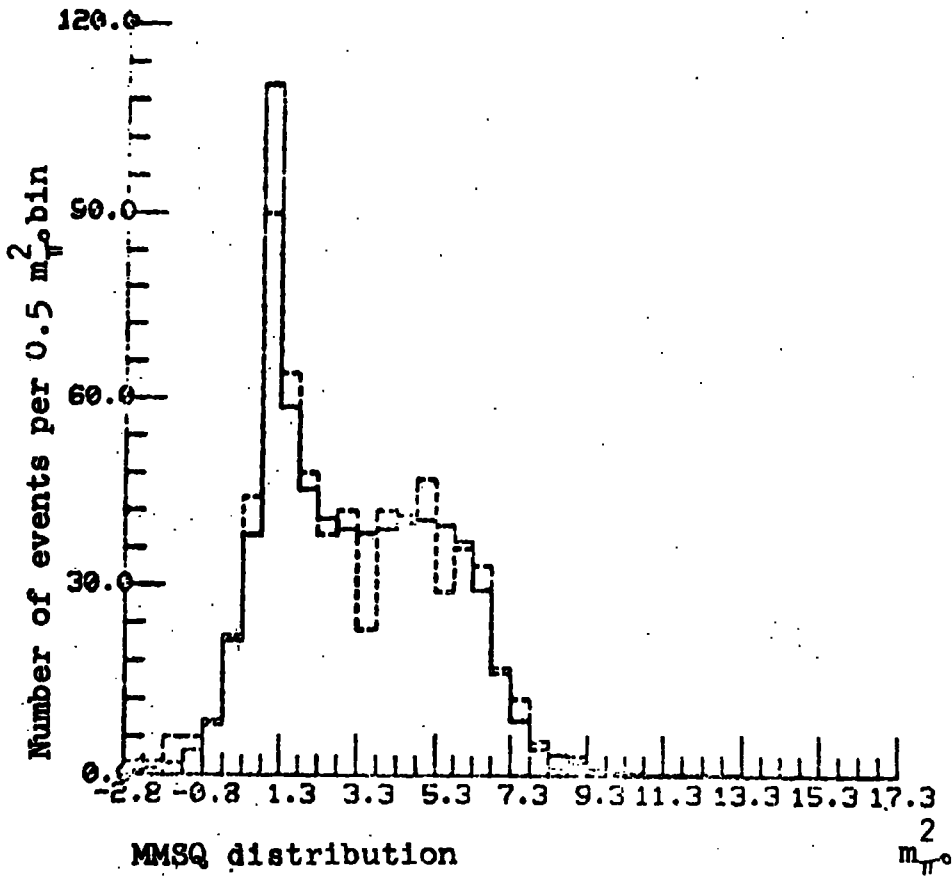
MMSQ distribution

Fig 5-2

likelihood function identical to that used in ref 5.2 is used

in Chapter 6, but in this Chapter a simpler approach is

adopted based on the missing mass squared(MMSQ) to the Λ^o .

5.1 SEPARATING THE $\Lambda^o \pi^o$ AND $\Sigma^o \pi^o$ CHANNELS

The missing mass squared is defined as follows:

$$\text{MMSQ} \equiv (q_i - q_\Lambda)^2$$

where q_i is the four-vector obtained by adding that of the

incident K^- to that of the target proton,

and q_Λ is the four-vector of the Λ^o .

With no measurement errors, the components of the

spectrum of MMSQ are shown in fig 5.1 where the unit for MMSQ

is the mass of the pi-zero squared $(m_{\pi^o}^2)$. The relative heights

of the components in the figure are arbitrary and are not

intended to convey any information.

For the $K^-p \rightarrow \Lambda^o \pi^o$, the missing mass squared is that of

the unseen π^o mass squared - which in units of $m_{\pi^o}^2$ forms a

δ-function at 1.0. In the case of the $K^-p \rightarrow \Sigma^o \pi^o$, the products

are $\Lambda^o \gamma \pi^o$ where the combination of $\gamma \pi^o$ gives the value of MMSQ.

As, in the rest system of the Σ^o, the gamma ray direction

relative to the π^o forms an isotropic distribution, this

provides a range of MMSQ in the form of a flat topped distrib-

ution, whose limits are imposed by the centre of mass energy

which is available .

The $\Lambda^o \gamma$ (the radiative interaction) and the $\Lambda^o \pi^o \pi^o$ dist-

ributions are included for the sake of completeness. As the

mass of the gamma ray is zero the MMSQ for the $K^-p \rightarrow \Lambda^o \gamma$ forms

a δ-function at zero and the $K^-p \rightarrow \Lambda^o \pi^o \pi^o$ channel has a lower

45

EMMSQ vs MMSQ

Fig 5-3

Length of V⁰s   centimetres
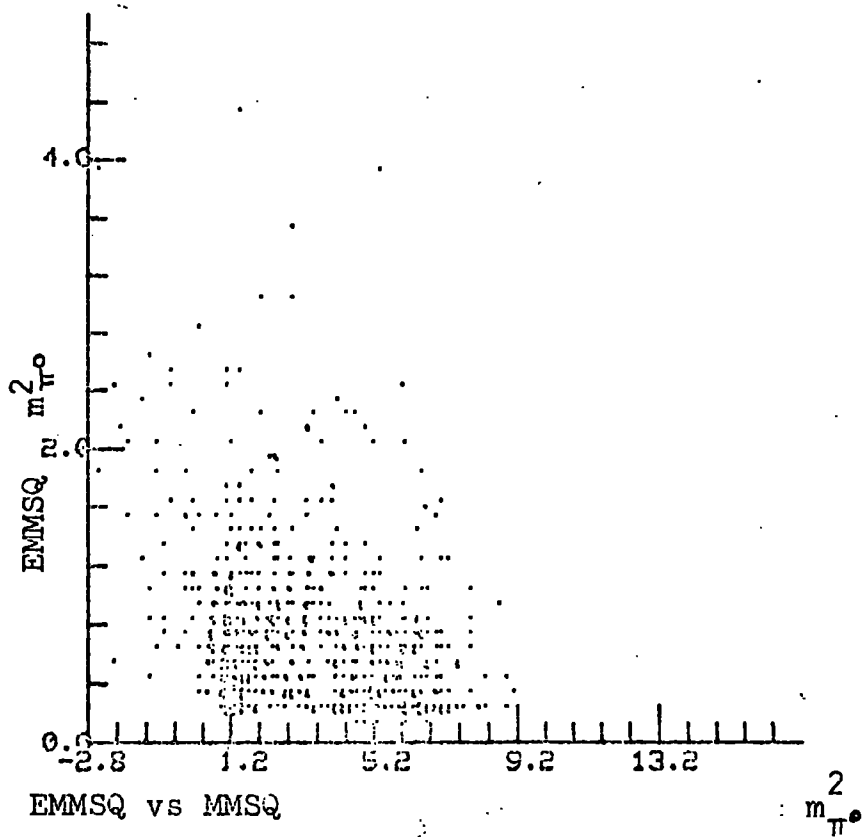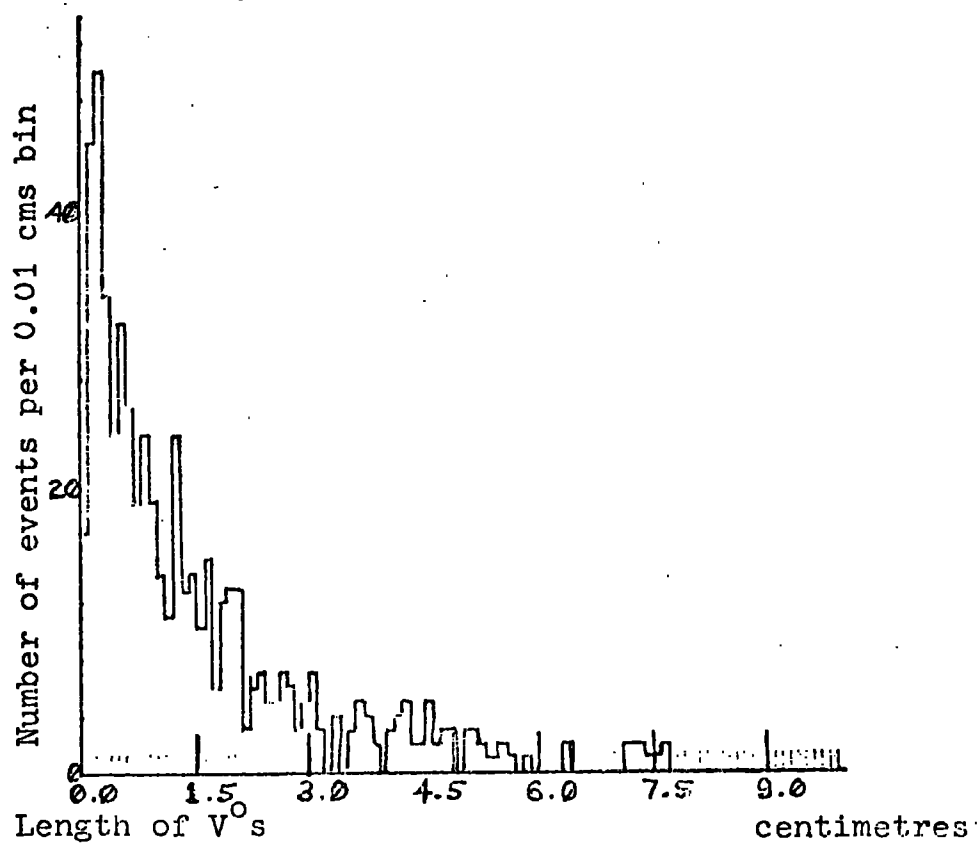
Fig 5-4

limit of $4m_\pi^2$, the upper limit again being given by the energy available   In the present analysis, the shape has been calculated from three body phase space. Tripp et. al. (ref 5.3) has shown that this distribution has some small deviation from phase space in this momentum region, but on the present statistics the effect of this would be negligible.

Experimentally the missing mass squared distribution is not in this idealised form (see fig 5.2) due to errors of measurement on all the tracks. These errors approximately Gaussian shaped missing mass squared distributions for K^- momenta above 150 Mev/c (see Chapter 4). If the error on the missing mass squared (EMMSQ) is known for each event, then it is possible to convolute this error into the theoretical distribution and,   by fitting to minimise the χ^2, determine the fractions of all channels in the total $K^-p \rightarrow \Lambda^0$ +neutrals.

5.2 ERROR ON THE MISSING MASS SQUARED

The error EMMSQ on MMSQ is obtained from the expression

$$MMSQ = m_K^2 + m_p^2 + 2E_K m_p + m_\Lambda^2$$

$$-2E_K E_\Lambda - 2m_p E_\Lambda + 2p_K p_\Lambda \cos \theta$$

where the subscripts p, K, Λ denote proton, kaon and Λ^0 , and m, E, p, θ are mass, total energy, momentum and angle between the vectors $\bar{p}_K$ and $\bar{p}_\Lambda$.

EMMSQ has to be found in terms of the errors of measurements and fitting which are available . The full expressions are given in Appendix A. The result is derived from :
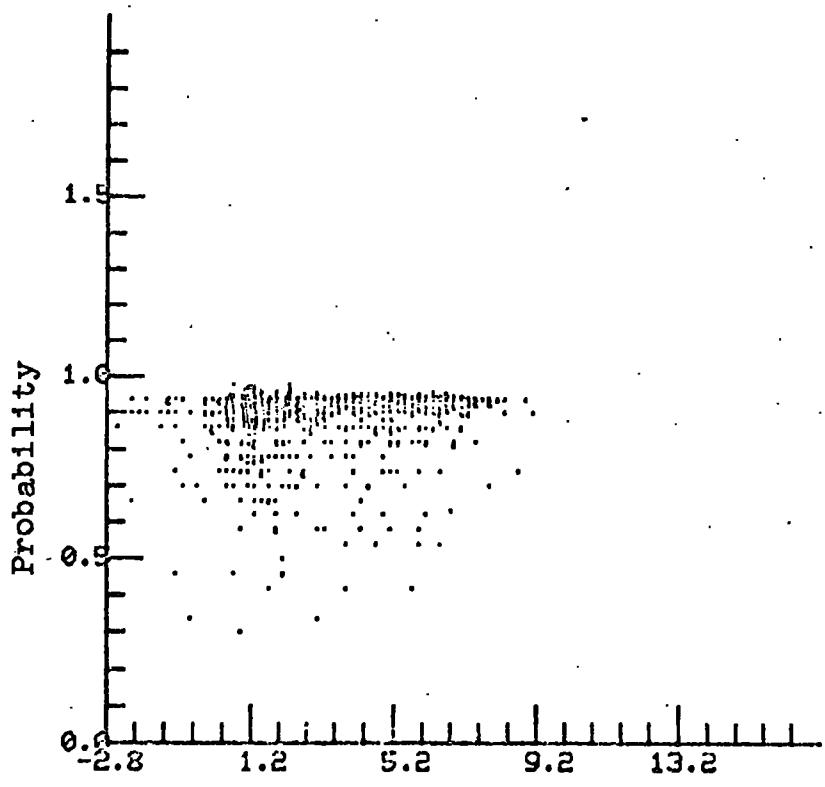
Probability of observation vs MMSQ $m^2_{\pi^o}$ Fig 5-5
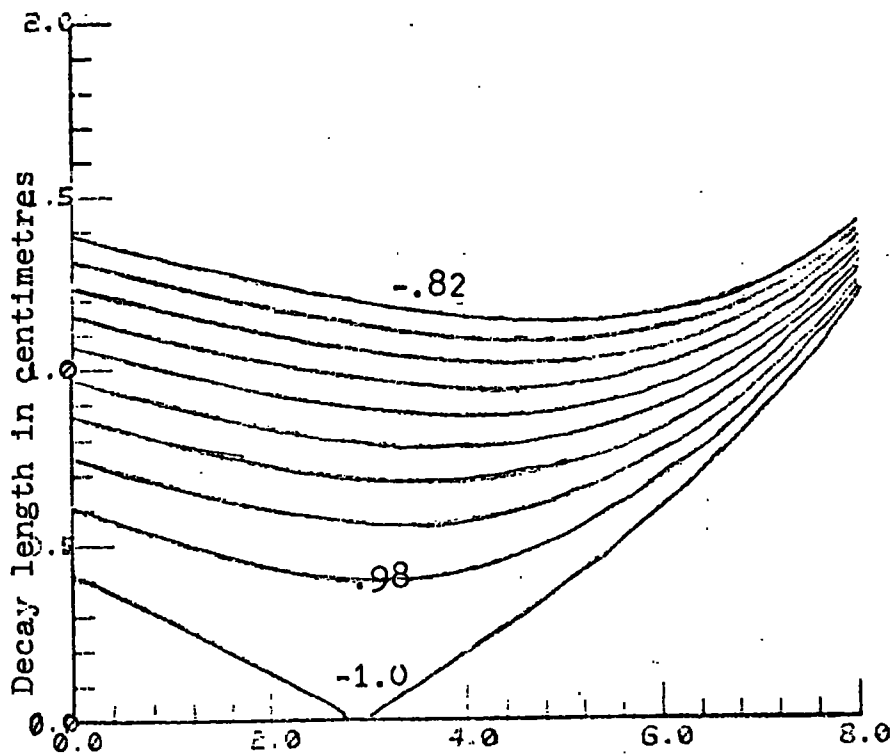
Decay length vs MMSQ for various
values of cos $\Theta^*_{\wedge}$

$m^2_{\pi^o}$

Fig 5-6

$$\text{EMMSQ} = \frac{\partial \text{MMSQ}}{\partial p_K} E(1/p_K) p_K^2 + \frac{\partial \text{MMSQ}}{\partial \phi_K} E(\phi_K) + \frac{\partial \text{MMSQ}}{\partial \lambda_k} \frac{E(\tan\lambda_K)}{\sec^2\lambda_K}$$

$$+ \frac{''}{\partial p_\Lambda} E(1/p_\Lambda) p_\Lambda^2 + \frac{''}{\partial \phi_\Lambda} E(\phi_\Lambda) + \frac{''}{\partial \lambda_\Lambda} \frac{E(\tan\lambda_\Lambda)}{\sec^2\lambda_\Lambda}$$

where $E(1/p), E(\phi)$ and $E(\tan\lambda)$ are the errors on reciprocal momentum, azimuth angle and tan(dip angle) respectively.

The errors $E(1/p_K)$ and $E(1/p_\Lambda)$ are at the interaction vertex of the K^- and the processing programs give the errors at the centre of track. As the Λ^0 track is neutral $E(1/p_\Lambda)_c = E(1/p_\Lambda)_V$ but for the K^- track the centre of track error $E(1/p_K)_c$ has to be swum to the vertex. The expression used to do this was :

$$E(1/p_K)_V = [p_{Kc}/p_{Kv}]^{n+1} E(1/p_K)_c$$

where n is from the approximate power law which relates the range of a track to its momentum.

$$R = \text{const. } p^n$$

The value of n was taken as 3.6.

Throughout this development correlation between the errors on the tracks is assumed to be zero and to first order, this is reasonable. However there is a correlation between the azimuth at the vertex and the centre of track momentum of the K^- track. This has been folded into the $E(1/p_K)_V$ error in the following way :

$$\text{EMMSQ} = \frac{\partial \text{MMSQ}}{\partial p_K} E(1/p_K) p_K^2 + \frac{\partial \text{MMSQ}}{\partial \phi_K} \frac{\partial \phi_K}{\partial p_K} E(1/p_K) p_K^2 +$$

$$\frac{\partial \text{MMSQ}}{\partial \phi_K} E(\phi_K) + \ldots\ldots\ldots$$

49

MMSQ distribution for biassed
sub-class of events

$m^2_{\pi^o}$

<u>Fig 5-7</u>

MMSQ distribution for biassed
sub-class of events after correction

$m^2_{\pi^o}$

<u>Fig 5-8</u>
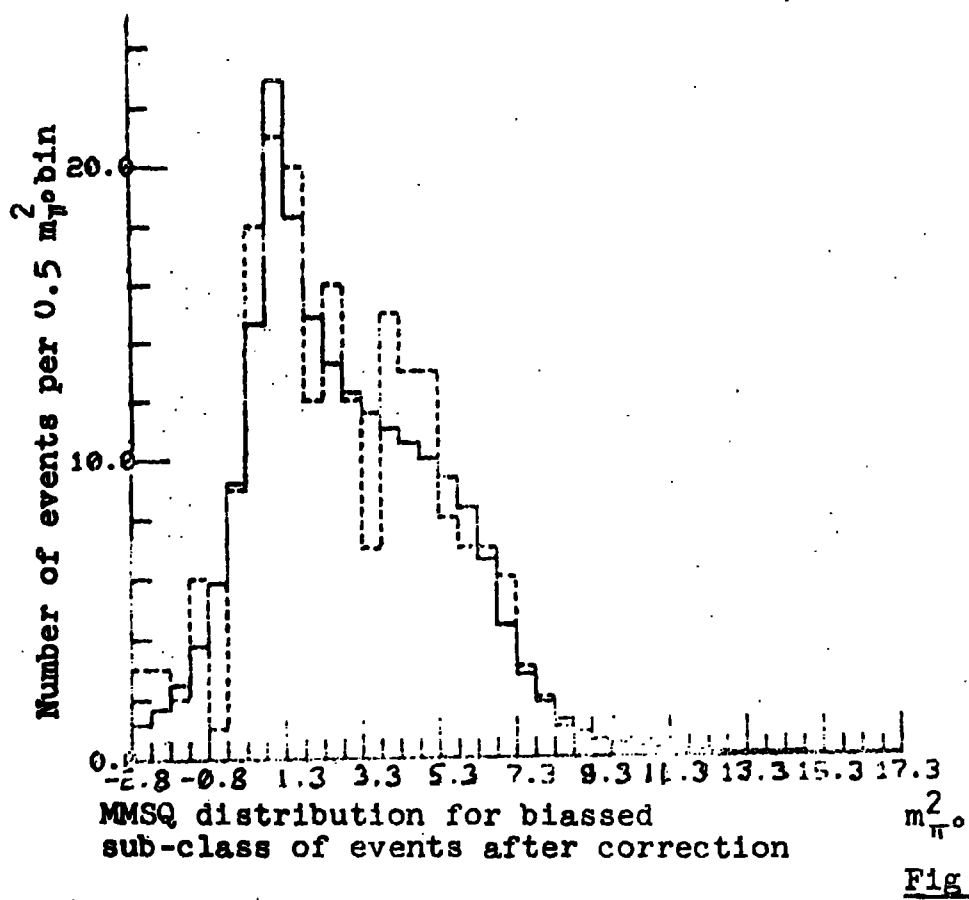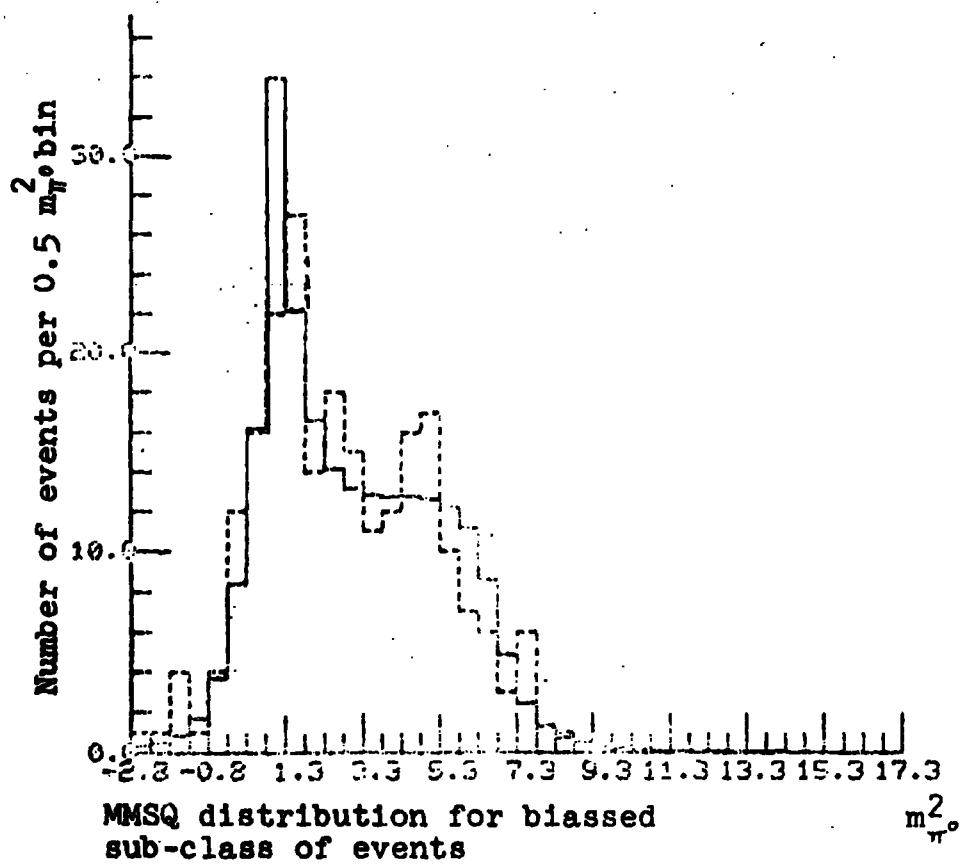
In order that the folding in of each error over the whole MMSQ distribution should be valid, EMMSQ, determined for each event, must bear no correlation to the MMSQ. It can be seen in fig 5.3 that this is a reasonable assumption.

The same must hold for the probability of seeing each event if the observed distribution of MMSQ is to exhibit the true physical ratios of channel intensities. From the point of view of lifetime effects, the probability of observation is

$$\text{Prob} = \exp(\ -l_c/d_1) - \exp(\ -l_{pot}/d_1)$$

where d_1 is the mean decay length for a Λ^o with momentum p_Λ.

The first term in the expression is the probability that the Λ^o will live long enough to give a visible gap between K^- and V^o, and the second is the probability that it will leave the fiducial volume. The value of l_c was taken to be 0.2 cms because in the length distribution of the Λ^os there is evidence of losses below this length (see fig 5.4). l_{pot} is calculated as the length traversed by the Λ^o to the edge of the fiducial volume. This is a cylinder of diameter 22.0 cms with the end faces on the walls of the T.S.T. a criterion setup at the scanning stage to eliminate wrongly associated V^os (i.e. a V^o which might point to a 0-prong K^- track but actually is produced elsewhere in the chamber, see section 3.1.4). Fig 5.5 shows the distribution of probability of observation vs MMSQ and shows no apparent correlation.

This can be understood by considering fig 5.6. The
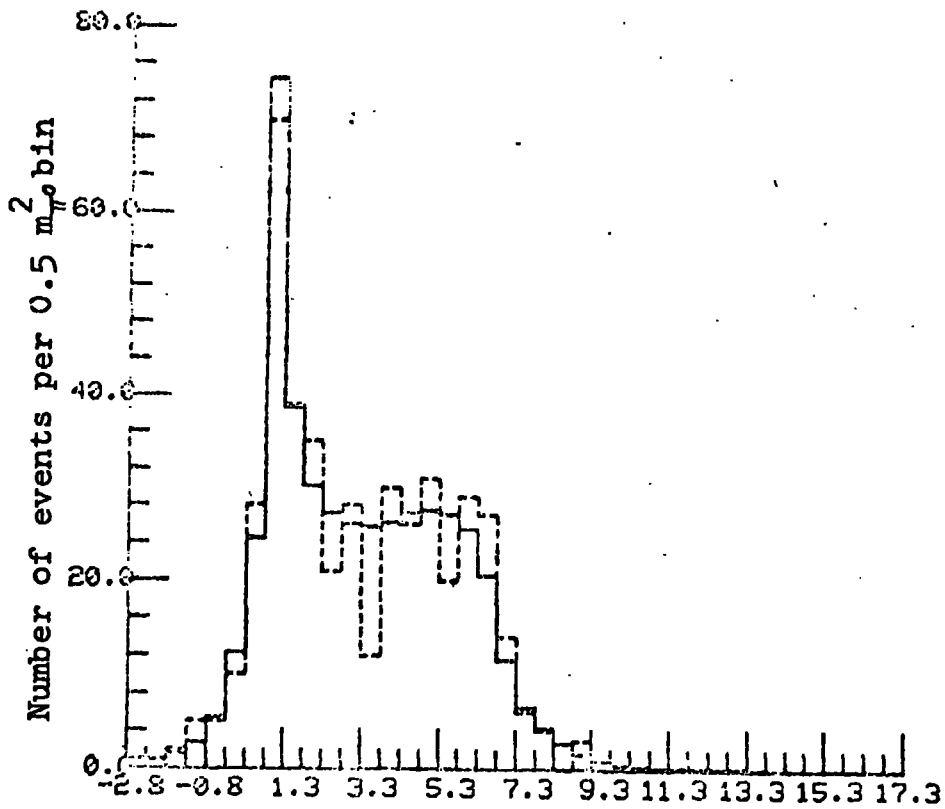
MMSQ distribution for unbiassed
sub-class of events. EMMSQ scaled by 1.12

Fig 5-9
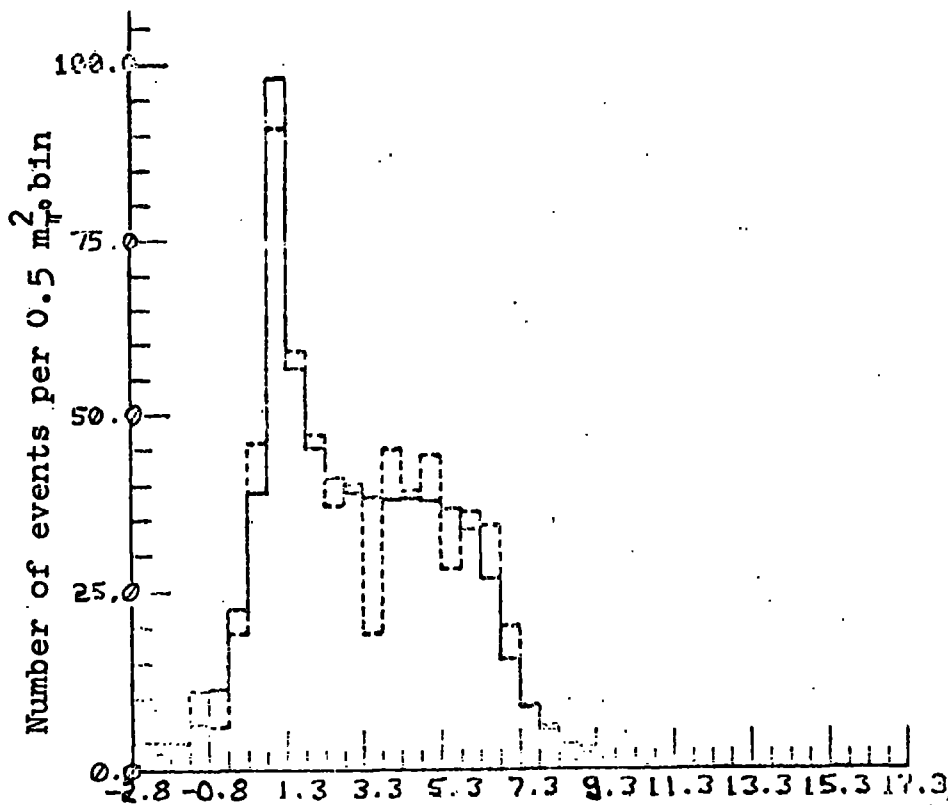
MMSQ distribution for total sample
with corrections for p_K 340→440 Mev/c

Fig 5-10

mean decay length is plotted as a function of MMSQ for
various $\cos \theta *$ ($\theta *$ is the centre of mass angle of the Λ^{o}).
The effect of the minimum length cutoff·of 0.2 cms is to
discriminate against events with values of MMSQ in the range
$1.6 \rightarrow 4.0$ m_{π}^{2}. for a very small interval of $\cos \theta *$ from -1.0
to -0.995. This has a negligible effect on the probability
of observation. At all other angles the mean decay length
does not change by more than 10% over the whole range of MMSQ
and hence there is no apparent correlation between probability
of observation and MMSQ.

5.3 CHANNEL BRANCHING RATIOS

Fig 5.2 shows the MMSQ distribution for K^{-} momenta
from 340 $\rightarrow$ 440 Mev/c i.e. a wide momentum interval around
the $\Lambda(1520)$ resonance excitation. The solid line is the
result of the fit and the dashed line is the actual data. It
can be seen that the π^{o} peak is too large in the fit compared
with the data, but that on either·side the agreement is
reasonable. Scaling the values of EMMSQ (the error for each
event multiplied by a constant factor) made the fit worse.

A search was then made for a sub-class of events which
might give an anomalous MMSQ.distribution in the region of
the π^{o} peak. After many attempts a class of events was found
with a shift to higher values of MMSQ, this distribution is
shown in fig 5.7. This subclass of events had the character-
istic that the proton from the Λ^{o} decay stopped in the Perspex
walls of the T.S.T. In these circumstances the processing
program GEOMETRY took the measurement of the proton momentum

from range and the endpoint of the track was taken to be the midpoint of its path through the Perspex walls. This procedure at first sight looks reasonable and would be adequate if, on average, the protons did stop half way through the Perspex. However as the protons from Λ^0 s in general have low momentum the average endpoint is much closer to the inside face of the T.S.T. wall. Therefore this procedure introduces a bias in the proton momentum which in turn effects the Λ^0 momentum and hence biases the MMSQ.

To overcome this bias in this sub-class of events, the Λ^0 momentum was recalculated from the measured angles.** As can be seen in fig 5.8, this puts the π^0 peak in the correct position, however the π^0 peak is much broader. To calculate the new EMMSQ for these events, the original EMMSQ (outlined above) was retained as the relative error on each event and then each error was scaled by 1.96, the result of this is shown in fig 5.8 . For this particular class of events the original biassed distribution had a χ^2 of 26.4 for 14 degrees of freedom, and the χ^2 for fig 5.8 was 13.15 for 15 degrees of freedom. Therefore it was concluded that the procedure adopted (re-calculating MMSQ and scaling the kinematic values of EMMSQ) was adequate.

It was found also that the rest of the events had an improved χ^2 if the EMMSQ for each event was scaled by 1.12. This fit is shown in fig 5.9

** This class of events are now being reprocessed as 2C fits i.e. the proton momentum is set unmeasured.

The total sample with biases removed, is shown in fig 5.10. The χ^2 for this fit is 30.5 with 17 degrees of freedom which gives a confidence level of about 5%. This high χ^2 results from two effects :

a) values of MMSQ out to -2.75 $m_{\pi^0}^2$ are retained for the fit. Their number is in excess of what would be expected from errors of measurement. Being in a region where the expected number is small, a few events add enormously to the χ^2.

b) There is a dip in the distribution at 3.5 $m_{\pi^0}^2$ which contributes a large amount to the χ^2. This dip occurs in one bin, and considering the width of the π^0 peak, is very unlikely to be a real physical effect. The minimum length cutoff effect shown in fig 5.6 is both too small and too wide to explain this dip. It is considered, therefore, to be a low probability statistical fluctuation. From the fit shown in fig 5.10, the channel branching ratios were found to be 31.4% $\Lambda^0\pi^0$, 1.9% $\Lambda^0\gamma$, 4.2% $\Lambda^0\pi\pi$ and 62.5% $\Sigma^0\pi^0$ (see below).

The MMSQ distributions were then fitted for different K^- momentum bins and the channel branching ratios calculated for each. The results are shown in fig 5.11 and table 5.1 for the $K^-p \rightarrow \Lambda^0\pi^0$ branching ratio. This clearly shows the Λ(1520), discussed in Chapter 1, which predominately decays to $\Sigma^0\pi^0$ at a K^- momentum of 390 Mev/c. Also shown, are the branching ratios determined by Tripp et. al. ref 5.2 . The agreement is good with the suggestion of the present data being somewhat lower by 10%, which in view of the statistics can hardly be considered a significant difference.

From table 5.1 it can be seen that the χ^2 values for

TABLE 5.1

Momentum Mev/c	χ^2	No. of degrees	No. in plot	Branching Ratio f	$\pm$error
150-260	3.86	7	81	.471	.074
260-310	22.5	11	131	.513	.051
310-340	9.27	9	119	.482	.062
340-360	4.93	9	94	.446	.087
360-380	11.53	10	130	.379	.055
380-400	24.8	13	146	.203	.047
400-420	11.04	13	183	.296	.046
420-440	4.51	9	99	.343	.066
440-480	6.44	7	74	.283	.071

most fits are good. For two of the nine momentum bins however the influence of the negative values of MMSQ and the dip at $3.5\ m_\pi^2$ can be seen to be severe. The fall in the branching ratio at 440→480 Mev/c may be due to a tail effect in the momentum distribution of the incident kaons. This momentum region is the extreme upper end of the momentum distribution and events might be ,in this region, due to errors of measurement but have true momenta at lower values, where the branching ratio is small.

Other channels included in the fits, $K^- p \to \Lambda^0 \gamma$ and $K^- p \to \Lambda^0 \pi^0 \pi^0$, are restricted to an upper limit of 2% and 25% respectively (refs 5.3 and 5.4) of the total $K^- p \to \Lambda^0$ +neutrals. With the statistics of this experiment, these channel branching ratios are not significantly greater than background.

The branching ratio of $K^-p \rightarrow \Lambda^0 \pi^0$ in the missing mass squared

distribution of $K^-p \rightarrow \Lambda^0 +$ neutrals as a function of K^- momentum

+ this experiment   o Tripp et al.

Fig 4-11
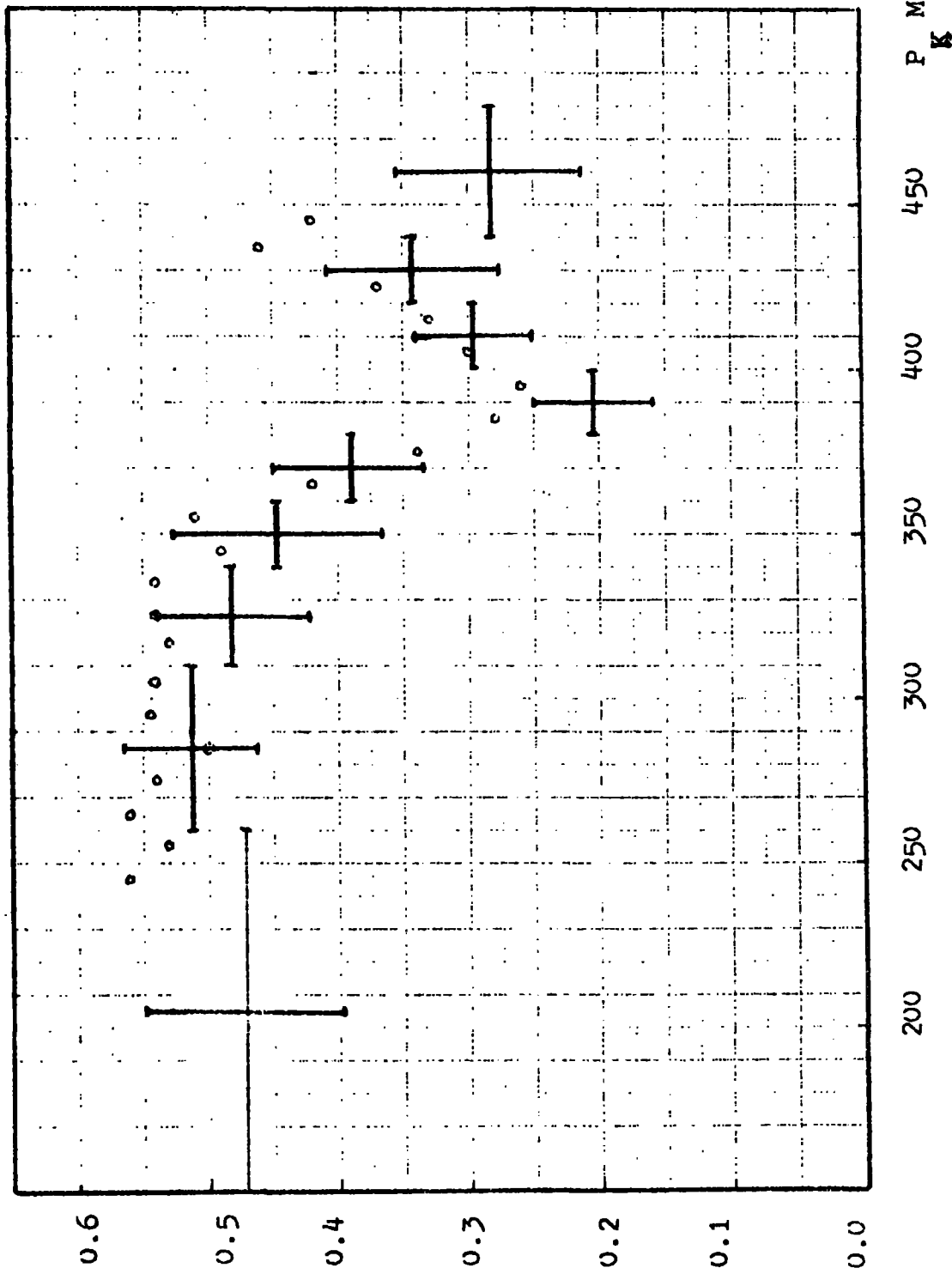
It is of interest that while the channel ratios given here are obtained by special treatment of part of the data, they are very close in value to those obtained in the first attempt to fit the data before any selections were made. The confidence levels of the fitted distributions were bad initially, but the branching ratios are somewhat insensitive to the selection and treatment of the data.

CHAPTER SIX

In Chapter 5, the channel branching ratios for $\Lambda^o\pi^o$ were found from the missing mass squared distribution as a function of K^- momentum. From table 5.1 it can be seen that the number of events per momentum bin are insufficient to determine the angular distributions as a function of momentum. To find the angular distributions, therefore a maximum likelihood approach was adopted and is described in this chapter. It is possible to get an average angular distribution in a momentum bin 340 to 440 Mev/c from the missing mass squared distribution fits and this is shown as a comparison with the maximum likelihood results. The analysis described here is a repeat of that given in ref 6.1. It is somewhat elaborate for the present statistics but has been prepared for use when the final data becomes available .

6.1 THE LIKELIHOOD FUNCTION

The data was divided into the same momentum bins used in Chapter 5 and the data was fitted in each bin independently to determine the angular distributions and polarisations of the $\Lambda^o\pi^o$ and $\Sigma^o\gamma^o$ channels.

Each event is completely defined by the following three quantities which form a kinematic set.

i) MMSQ, the missing mass squared of the unseen neutrals as defined in Chapter 5.

ii) $\cos\theta_\Lambda^*$, the cosine of the angle between the Λ^o and the K^- in the K^-p centre of mass system, see fig 6.1a

iii) $\cos b$, where

$$\cos b = \bar{p} \cdot \frac{(\bar{K} \times \bar{\Lambda})}{[(\bar{K} \times \bar{\Lambda})]}$$

and $\bar{K}$, $\bar{\Lambda}$ are the beam and Λ^{o} directions in the centre of mass and $\bar{p}$ is a unit vector in the proton direction in the Λ^{o} rest frame.

The likelihood for each event is written as follows :

$$\pounds(MMSQ_1 , \cos \theta^*_{\Lambda 1}, \cos b_1) = \pounds_{\Lambda^o \pi^o} + \pounds_{\Sigma^o \pi^o} + \pounds_{\Lambda^o \gamma} + \pounds_{\Lambda^o \pi^- \pi^o}$$

The expressions for each of these likelihoods is described below. To account for the finite resolution of the MMSQ a Gaussian function was used.

$$G(MMSQ, MMSQ^*) = \frac{1}{\sqrt{2\pi} \, EMMSQ} \exp\left\{ -\frac{(MMSQ - MMSQ^*)^2}{2(EMMSQ)^2} \right\}$$

This can be justified by the fits of Chapter 5 which require Gaussian errors. For convenience as in Chapter 5, units of $m_{\pi^o}^2$ were used.

a) $\pounds_{\Lambda^o \pi^o}$

The likelihood that the event belongs to the $\Lambda^{o}\pi^{0}$ channel is defined by

i) the angular distributions for production and decay

$$\frac{dN}{d(\cos \theta^*_\Lambda) d(\cos b)} = I(1 + \alpha P_\Lambda \cos b)$$

where P_Λ is the Λ^o polarisation which is itself a function of $\cos \theta^*_\Lambda$, and $\alpha = 0.645$ is the Λ^o decay asymmetry parameter.

ii) the Gaussian probability function centred at one $m_{\pi^o}^2$

$$f_{\Lambda^o \pi^o} G(1 , MMSQ^*)$$

where $f_{\Lambda^o \pi^o}$ is the fraction of $\Lambda^o \pi^o$ in the total channel. The angular distribution and polarisation distribution
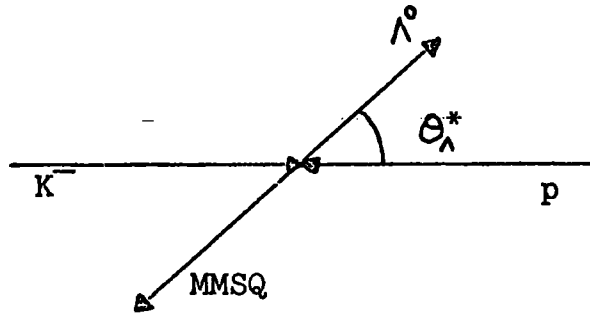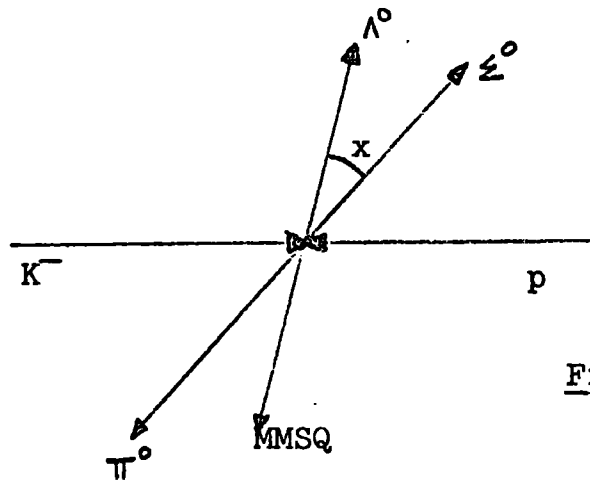
Fig 6-1a

Fig 6-1b
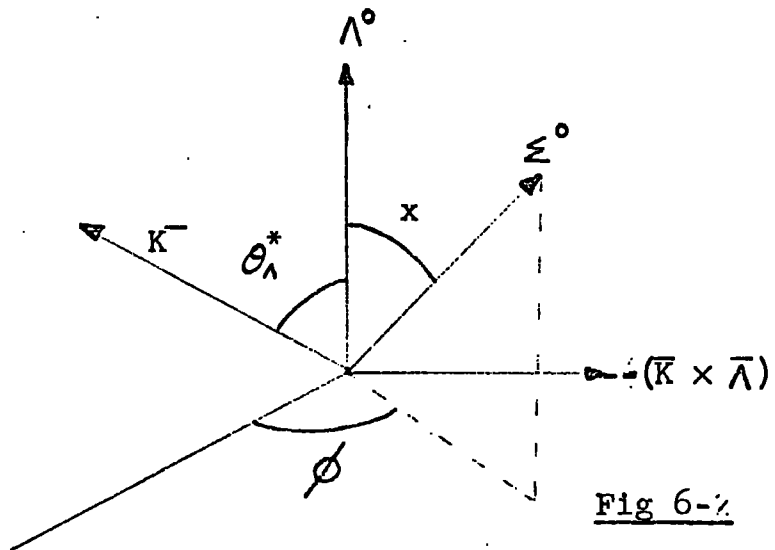
Fig 6-2

have been parameterised in the form of Legendre polynomials,
giving :

$$\mathcal{L}_{\Lambda\pi^o} = f_{\Lambda^o}G(\,1\,,MMSQ*)\underset{1}{\mathcal{\le}}\,[A_1P_1(\cos\theta_\Lambda*) + \alpha\cos b\,\sin\theta_\Lambda^*\,B_1P_1'(\cos\theta_\Lambda*]$$

<div align="right">eqn. 6.1</div>

Using $\sin\theta_\Lambda^*P_1'(\cos\theta_\Lambda*) = P_{1,1}(\cos\theta_\Lambda*)$ for IP_Λ ensures the
physical requirement that $P_\Lambda = 0$ for $\theta_\Lambda^* = 0^o$ and 180°.

b) $\mathcal{L}_{\Sigma^o\pi^o}$

For the $K^-p \rightarrow \Sigma^o\pi^o$ channel the Σ^o direction is unknown.
Only the Λ^o is observed. The angle x between the Σ^o direction
and its Λ^o decay product can be calculated from the value
of MMSQ (see fig 6.1b). The Σ^o can still be anywhere in a cone
around the Λ^o direction at an angle x to the Λ^o direction
(see fig 6.2). In this momentum region tha angle is small
(max = 15°) but it is taken into account below.

If the Σ^o direction was known the likelihood of the $\Sigma^o\pi^o$
events could be written in a similiar form to eqn 6.1.
However the terms have to be modified to allow for the
unseen Σ^o .

Expressing the intensity in terms of Legendre polynomials

$$I = \frac{dN}{d(\cos\theta_\Sigma^*)} = \underset{1}{\mathcal{\le}}\,C_1\,P_1(\cos\theta_\Sigma^*)$$

the following identity is used to transform to the measured
angle of the Λ^o :

$$P_1(\cos\theta_\Sigma^*) = \frac{4\pi}{2l+1}\underset{m=-1}{\overset{m=+1}{\mathcal{\le}}}\,Y_{1,m}(x,\phi)\,Y_{1,-m}(\theta_\Lambda^*,\phi)$$

ϕ is the unknown azimuth angle of the Λ^o round the Σ^o see
fig 6.2.
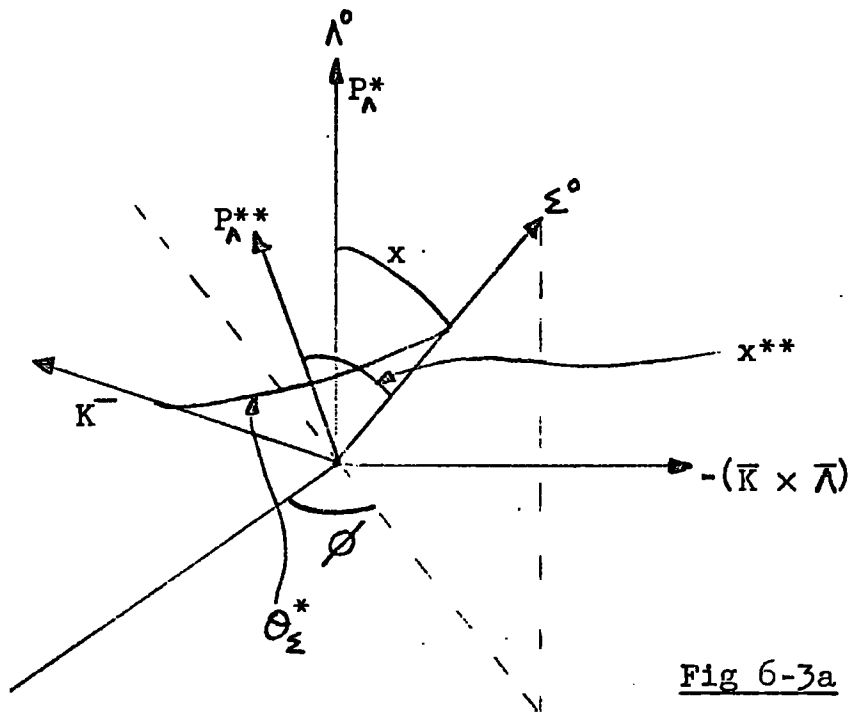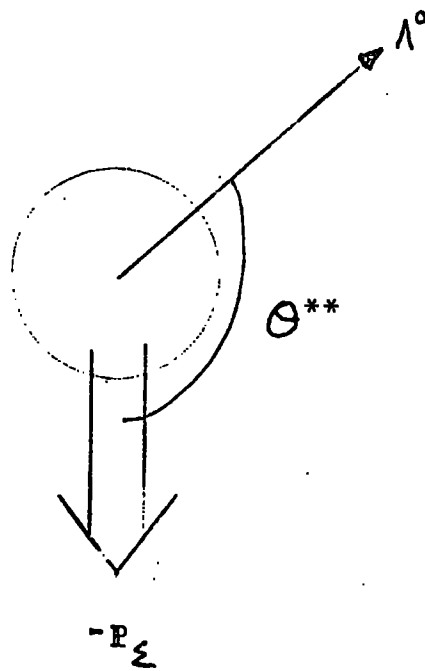
Fig 6-3a

Fig 6-3b

Integrating over ϕ gives

$$P_1(\cos\theta_\Sigma^*) = P_1(\cos x)\, P_1(\cos\theta_\Lambda^*)$$

therefore

$$\frac{dN}{d(\cos\theta_\Sigma^*)} = \sum_1 C_1\, P_1(\cos x)\, P_1(\cos\theta_\Lambda^*)$$

A fuller derivation is given in Appendix B.

The polarisation of the Σ^o can still only be measured through the amount transferred to the Λ^o, using the full angular distribution including cos b :

$$\frac{dN}{d(\cos\theta_\Sigma^*)d(\cos b)} = I(\, 1 + \alpha\, P_\Lambda \cos b) \qquad \text{eqn 6.2}$$

In the rest system of the Σ^o (see fig 6.3b), the polarisation is along the direction of the Λ^c :

$$\mathbf{P}_\Lambda = \mathbf{P}_\Sigma \cos\theta^{**}\frac{\overline{\mathbf{P}}_\Lambda}{[\mathbf{P}_\Lambda]}$$

Where $\mathbf{P}_\Sigma$ the polarisation of the Σ^o is along the normal to the $K^-\Sigma^o$ plane. The polarisation of the Λ^o is measured with respect to the $K^-\Lambda^o$ plane. The component of polarisation of the Λ^o in the direction of this normal is given by :

$$\mathbf{P}_\Lambda = -\, \mathbf{P}_\Sigma \cos\theta^{**}\, \sin(x^{**} - x)\, \sin\phi$$

(see fig 6.3a)

where x^{**} is the angle between the Σ^o and the Λ^o in the rest frame of the Σ^o. Using the invariance of transverse momentum to a Lorentz transformation,

$$P_\Lambda^*\, \sin x = P_\Lambda^{**}\, \sin x^{**}$$

where P_Λ^* and P_Λ^{**} are the Λ^o momenta in the centre of mass

and the rest system of the Σ^o respectively. Also from geometry (see fig 6.3a)

$$\cos \theta^{**} = \frac{\sin x^{**} \sin \theta_{\Lambda}^* \sin \phi}{\sin \theta_{\Sigma}^*}$$

Hence the polarisation term in eqn 6.2 above can be written in terms of P_{Σ} :

$$IP_{\Lambda} = IP_{\Sigma} \frac{\sin \theta_{\Lambda}^*}{\sin \theta_{\Sigma}^*} \sin^2\phi \frac{P^* \sin^2 x (P^*\cos x - P^{**}\cos x^{**})}{P^{**^2}}$$

Working in the rest frame of the Σ^o ,

$$P^{**^2} = \frac{(m^2_{\Sigma} - m^2_{\Lambda})^2}{4m^2_{\Sigma}}$$

P^* cos x is the Lorentz transformed component of P^{**}, along the direction of the Σ^o, from the Σ^o rest system to the centre of mass system i.e.

$$P^* \cos x = \frac{E_{\Sigma}}{m_{\Sigma}} P^{**} \cos x^{**} + \frac{P_{\Sigma}}{m_{\Sigma}} (m^2_{\Lambda} + P^{**^2})^{1/2}$$

where E_{Σ} and P_{Σ} are the centre of mass energy and momentum respectively of the Σ^o. Bearing in mind that in this energy range $P_{\Sigma} < 0.3$ Gev/c making E_{Σ}/m_{Σ} approximately unity and P^{**} is 0.074 Gev/c,

$$P^* \cos x \Rightarrow P^{**} \cos x^{**} + \frac{P_{\Sigma}}{m_{\Sigma}} m_{\Lambda}$$

Hence

$$IP_{\Lambda} = \frac{-4m_{\Sigma} m_{\Lambda} P_{\Sigma} P_{\Lambda} IP_{\Sigma}}{(m^2_{\Sigma} - m^2_{\Lambda})^2} \frac{\sin \theta_{\Lambda}^*}{\sin \theta_{\Sigma}^*} \sin^2\phi \sin^2 x \qquad \text{eqn 6.3}$$

In a similiar manner to that for the $\Lambda^o \pi^o$ channel, IP_{Σ} is expanded as :

$$IP_{\Sigma} = \sin \theta_{\Sigma}^* \sum_1 D_1 P_1'(\cos \theta_{\Sigma}^*)$$

The final relation on substituting into eqn 6.3,
expressing $\cos\theta_\Sigma^*$ in terms of $\cos\theta_\Lambda^*$ and integrating over ϕ
as was done for I above, yields, for the full distribution :

$$\frac{dN}{d(\cos\theta_\Sigma^*)d(\cos b)} = \sum_l C_l P_l(\cos\theta_\Lambda^*)P_l(\cos x) +$$

$$2\pi\alpha M \sin\theta_\Lambda^* \sin^2 x \sum_l \frac{D_l P_l'(\cos\theta_\Lambda^*)P_l'(\cos x)}{l(l+1)}$$

where

$$M = \frac{-4m_\Sigma m_\Lambda P_\Sigma P_\Lambda}{(m_\Sigma^2 - m_\Lambda^2)^2}$$

The likelihood for the $\Sigma\pi^0$ channel also has to take
into account the range of MMSQ which lies between MMSQ min
and MMSQ max. This gives for the likelihood function :

$$\mathcal{L}_{\Sigma\pi^0} = f_{\Sigma\pi^0}\int_{MMSQ\ min}^{MMSQ\ max} G(MMSQ, MMSQ^*)\frac{dN}{d(\cos\theta_\Sigma^*)d(\cos b)}\frac{d(MMSQ^*)}{\left(MMSQ_{max} - MMSQ_{min}\right)}$$

where $f_{\Sigma\pi^0}$ is the fraction of $\Sigma\pi^0$ in the total channel. It
should be noted that MMSQ max and MMSQ min depend on the K^-
momentum for a particular event.

c) $\mathcal{L}_{\Lambda^0\gamma}$

This likelihood was written as in ref 6.1 as

$$\mathcal{L}_{\Lambda^0\gamma} = f_{\Lambda^0\gamma}G(0, MMSQ^*)\left(1 - \frac{1}{2}P_2(\cos\theta_\Lambda^*)\right)$$

d) $\mathcal{L}_{\Lambda^0\pi\pi^0}$

The likelihood for the $K^-p \rightarrow \Lambda^0\pi\pi^0$ channel was written
as

$$\mathcal{L}_{\Lambda^0\pi\pi^0} = f_{\Lambda^0\pi\pi^0}\int G(MMSQ, MMSQ^*)\ g\ d(MMSQ^*)$$

where g was parameterised to approximately reproduce the

MMSQ and angular distributions found by Tripp et al ref 6.2.

(c) and (d) were included for completeness and nothing about these channels were determined in the likelihood analysis.

The final contribution to the likelihood of the set for a given event, was the sum of the above terms calculated for that event multiplied by the probability of observing the Λ^0 (see Chapter 5) :

$$\pounds_i = P_{obs} [\pounds_{\Lambda^0\pi^0} + \pounds_{\Sigma^0\pi^0} + \pounds_{\Lambda^0\gamma} + \pounds_{\Lambda^0\pi^0\pi^0}]_i$$

In the angular distributions described above, the summation of the Legendre polynomials in theory goes to infinity. Bearing in mind the presence of the D-wave $\Lambda(1520)$ significant contributions are expected up to lmax = 4. For the present analysis, lmax =3 was taken to reduce the number of parameters to be determined. An attempt to include lmax =4 merely resulted in random fluctuations of the coefficients without much change in those for lower values of l. Indeed Tripp et al ref 6.1 found the coefficient for l = 4 close to zero and Berley et al ref 6.3 did not include that partial wave.

The fits were initially attempted allowing the channel branching ratios to vary, these were found to be approximately 20% lower than those determined in Chapter 5. In view of the statistics, it was thought that too many parameters were being determined with this analysis and the fit was repeated with the channel branching ratios fixed at those determined previously. The likelihood function was maximised using a program called MINUIT.
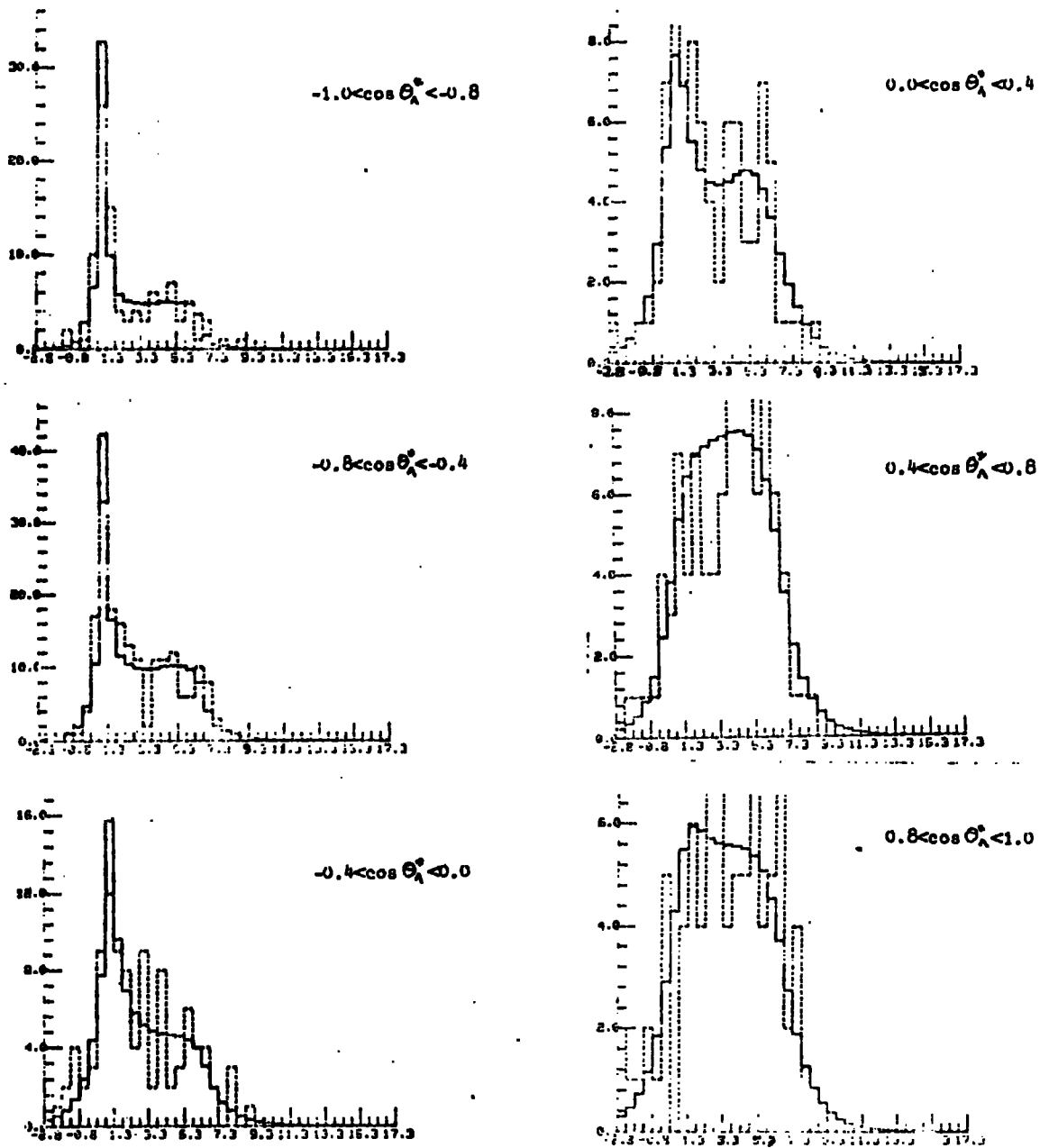
MMSQ distributions for 6 intervals of $\cos\theta_\Lambda^*$
for the momentum bin 340 → 440 Mev/c
(vertical scale = No. of events/0.5 $m_{\pi^0}^2$
horizontal scale = $m_{\pi^0}^2$ units)

Fig 6-4

6.2 THE AVERAGE ANGULAR DISTRIBUTION FOR 340 - 440 Mev/c

To check the consistency of the results obtained from the likelihood analysis, a comparison was made with the angular distribution it is possible to obtain from the simpler approach of Chapter 5.

To ensure adequate statistics a momentum bin 340 - 440 Mev/c was used. The principle was to split the events into intervals of cos θ_Λ^* and find the branching ratio of $K^-p \to \Lambda^0\pi^0$ channel for cos θ_Λ^* interval. The sample was the same as used for the branching ratio determinations in Chapter 5. In fig 6.4, the missing mass squared distributions are shown for the 6 intervals of cos θ_Λ^* used. It should be noted that for cos $\theta_\Lambda^* > 0.8$ there is very little $\Lambda^0\pi^0$ channel, but events at negative MMSQ gave an unreasonably large branching ratio of $K^-p \to \Lambda^0\pi^0$ and a large χ^2. The reason for this was tail noise and low signal. Therefore for this bin MMSQ < 0.0 have been excluded in this and the likelihood function analysis. Table 6.1 gives the branching ratio for $K^-p \to \Lambda^0\pi^0$ as a function of cos θ_Λ^* interval for the momentum bin 340 → 440 Mev/c.

The likelihood analysis was also done on the momentum bin 340 → 440 Mev/c for direct comparison and the Legendre polynomial coefficients are shown in Table 6.2. The angular distributions are shown graphically in figs 6.5 and 6.6. (the solid lines). Also shown are the points (*) obtained from the missing mass squared approach detailed above. It can be seen that there is good agreement between the two approachs.

Angular distribution
for $K^-p \rightarrow \Lambda^0\pi^0$

Fig 6-5

Angular distribution
for $K^-p \rightarrow \Sigma^0\pi^0$
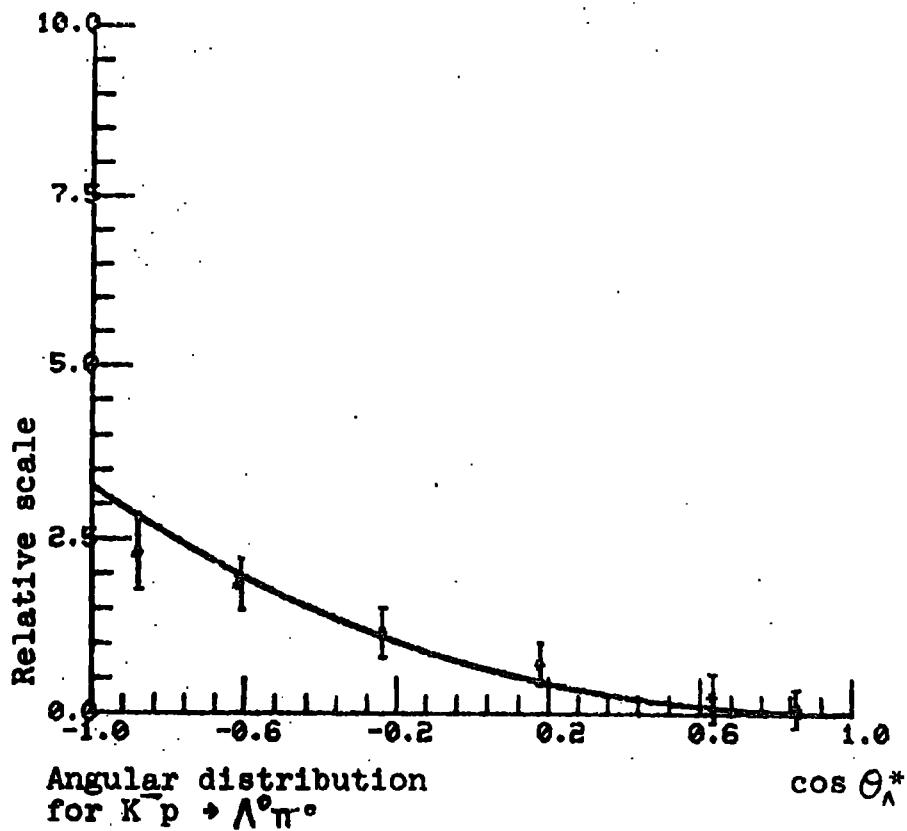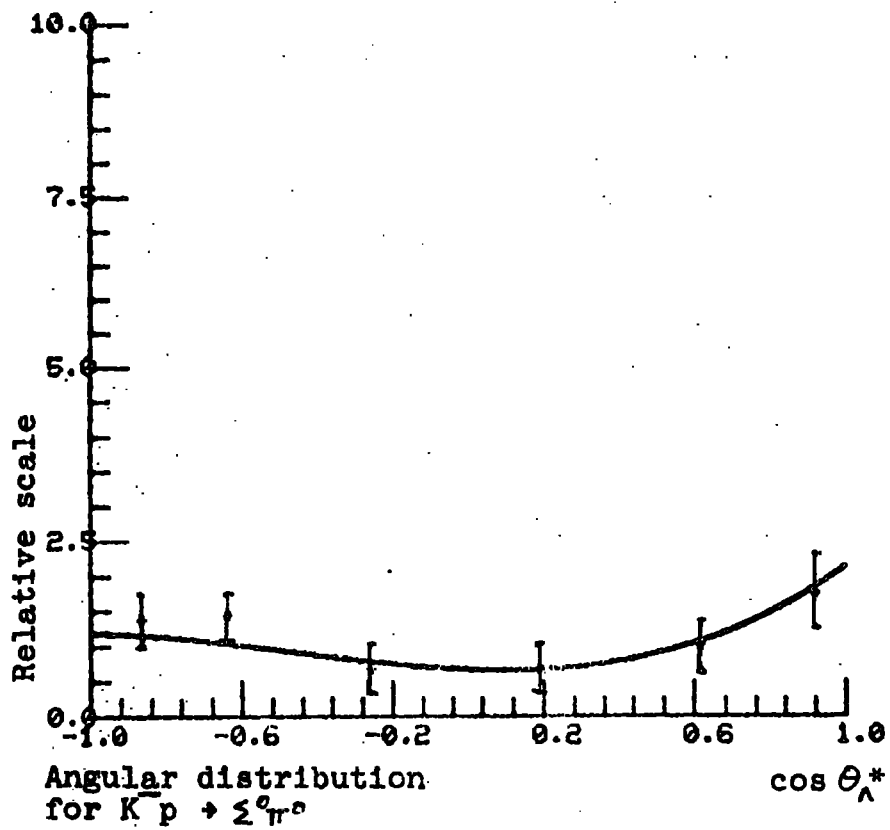
Fig 6-6

TABLE 6.1

Branching ratio of $K^-p \to \Lambda^0\pi^0$ as a function of $\cos\theta_\Lambda^*$

$\cos\theta_\Lambda^*$	No. of events	$f_{\Lambda^0\pi^0} \pm$ error	χ^2	No. of deg. freedom
-1.0 → -0.8	100	0.43 ± .06	8.1	7
-0.8 → -0.4	185	0.362 ± .05	15.1	11
-0.4 → 0.0	98	0.441 ± .07	10.1	9
0.0 → 0.4	82	0.326 ± .07	7.9	9
0.4 → 0.8	102	0.096 ± .05	10.6	9
0.8 → 1.0 (a)	85	0.2 ± .07	14.4	8
0.8 → 1.0 (b)	74	0.0 ± .07	8.4	7

(a) See text

(b) Corrected by excluding MMSQ < 0.0 events.

TABLE 6.2

Coefficients of the production angular distributions averaged over 340 → 440 Mev/c

Channel	A_1/A_0	A_2/A_0	A_3/A_0
$K^-p \to \Lambda^0\pi^0$	-1.57 ± .03	0.628 ± .1	-0.057 ± .08
$K^-p \to \Sigma^0\pi^0$	0.195 ± .15	0.666 ± .13	0.28 ± .07

6.3 ANGULAR AND POLARISATION LEGENDRE COEFFICIENTS AS A FUNCTION OF MOMENTUM

In this section, the results of the likelihood analysis are given. In table 6.3, the Legendre coefficients are shown as a function of momentum for the production angular distribution of the $K^-p \to \Lambda^0\pi^0$ channel and are shown graphically in fig 6.7. For comparison the results of Berley (x) and Tripp (0) are also shown in the figure.

TABLE 6.3

$\Lambda^o \pi^o$ Production angular distribution Legendre coefficients

Momentum (Mev/c)	A_1/A_o	A_2/A_o	A_3/A_o
205	-0.70 ± 1.18	0.50 ± 1.37	0.22 ± 1.40
285	$-0.72 \pm .11$	$0.22 \pm .12$	$-0.49 \pm .11$
325	$-1.14 \pm .78$	$0.78 \pm .92$	-0.19 ± 1.10
350	$-1.26 \pm .01$	$0.52 \pm .03$	$-0.24 \pm .05$
370	$-1.39 \pm .12$	$0.74 \pm .20$	$0.25 \pm .13$
390	$-1.16 \pm .06$	$0.42 \pm .10$	$-0.13 \pm .11$
410	$-1.44 \pm .13$	$0.52 \pm .84$	$0.11 \pm .18$
430	$-1.45 \pm .12$	$0.80 \pm .18$	$-0.31 \pm .15$
460	-2.00 ± 1.50	$1.82 \pm .27$	$-0.81 \pm .06$

TABLE 6.4

$\Sigma^o \pi^o$ Production angular distribution Legendre coefficients

Momentum (Mev/c)	c_1/c_o	c_2/c_o	c_3/c_o
205	0.25 ± 1.08	-0.20 ± 1.65	0.55 ± 1.13
285	$-0.10 \pm .92$	0.07 ± 1.35	0.07 ± 1.64
325	$0.19 \pm .80$	$-0.34 \pm .49$	$0.48 \pm .45$
350	$0.41 \pm .89$	-0.43 ± 1.17	-0.14 ± 1.25
370	$0.31 \pm .78$	0.23 ± 1.18	$0.48 \pm .75$
390	$0.10 \pm .68$	$0.88 \pm .93$	-0.57 ± 1.29
410	$0.17 \pm .87$	$0.99 \pm .74$	0.71 ± 1.09
430	0.02 ± 1.05	1.44 ± 1.19	0.73 ± 1.41
460	0.62 ± 1.11	$1.04 \pm .33$	-0.02 ± 1.18

TABLE 6.5

$\Lambda^o \pi^o$ Polarisation distribution Legendre coefficients

Momentum (Mev/c)	B_1/A_o	B_2/A_o	B_3/A_o
205	0.23 ± 1.54	-0.32 ± 1.31	-0.58 ± 1.33
285	0.34 ± 2.91	-0.02 ± 1.27	-0.56 ± 1.00
325	-0.19 ± 2.83	-0.21 ± 1.38	-0.15 ± 1.26
350	-0.55 ± 2.72	0.02 ± 1.49	$-0.00 \pm .93$
370	$-0.01 \pm .36$	$-0.21 \pm .14$	$0.50 \pm .11$
390	$0.81 \pm .33$	$-0.30 \pm .12$	$-0.17 \pm .07$
410	$0.24 \pm .14$	$0.06 \pm .09$	$-0.20 \pm .62$
430	$0.00 \pm .41$	$0.13 \pm .17$	$0.11 \pm .12$
460	1.89 ± 3.04	-2.00 ± 3.55	0.79 ± 1.04

TABLE 6.6

$\Sigma^o \pi^o$ Polarisation distribution Legendre coefficients

Momentum (Mev/c)	D_1/C_o	D_2/C_o	D_3/C_o
205	$-0.02 \pm .94$	$-0.43 \pm .60$	$-0.06 \pm .57$
285	$0.14 \pm .73$	$0.10 \pm .57$	$0.08 \pm .50$
325	$0.02 \pm .60$	$0.03 \pm .32$	$0.01 \pm .21$
350	$-0.07 \pm .78$	$-0.15 \pm .67$	$-0.15 \pm .72$
370	$0.10 \pm .44$	$0.12 \pm .39$	$0.05 \pm .39$
390	$0.00 \pm .41$	$0.18 \pm .43$	$-0.13 \pm .31$
410	$-0.02 \pm .32$	$0.11 \pm .37$	$0.06 \pm .27$
430	$0.12 \pm .64$	$0.12 \pm .51$	$0.02 \pm .46$
460	$0.41 \pm .25$	$-0.33 \pm .56$	$-0.11 \pm .18$

In view of the low statistics compared with these previous experiments, there is very good agreement. The monotonic decrease of A_1/A_0 is well reproduced.

The results of the $K^-p \rightarrow \Sigma^0\pi^0$ channel angular distribution are shown in table 6.4 and graphically in fig 6.8. Again within errors, this experiment shows good agreement with the previous results. The C_2/C_0 coefficient shows a large rise in the region $380 \rightarrow 420$ Mev/c (the $\Lambda(1520)$), though the rise is not as large as that determined by Berley and Tripp, it clearly demonstrates the presence of the $\Lambda(1520)$ D-wave resonance.

The polarisation Legendre coefficients for $K^-p \rightarrow \Lambda^0\pi^0$ are shown in table 6.5 and fig 6.9. The large errors, the penalty of the low statistics, make it difficult to draw any conclusions about these coefficients.

For the $K^-p \rightarrow \Sigma^0\pi^0$ channel the results are shown in table 6.6 and fig 6.10. Here again it is difficult to draw conclusions. However the coefficients are on average within one standard deviation of those determined by Berley and Tripp. The values of D_2/C_0 in the $\Lambda(1520)$ region are not as high as obtained by previous workers, but in any case the earlier results do not agree too well with each other to define the behaviour with momentum of the polarisation coefficients.

Production angular distribution Legendre coefficients as a function of momentum. $K^- p \rightarrow \Lambda^o \pi^o$

74
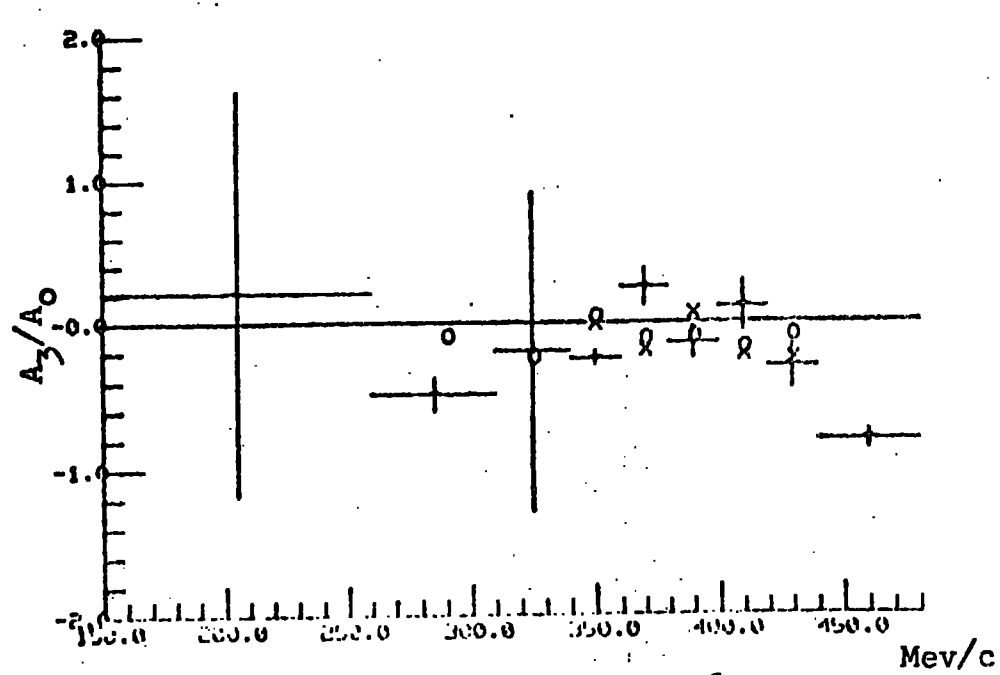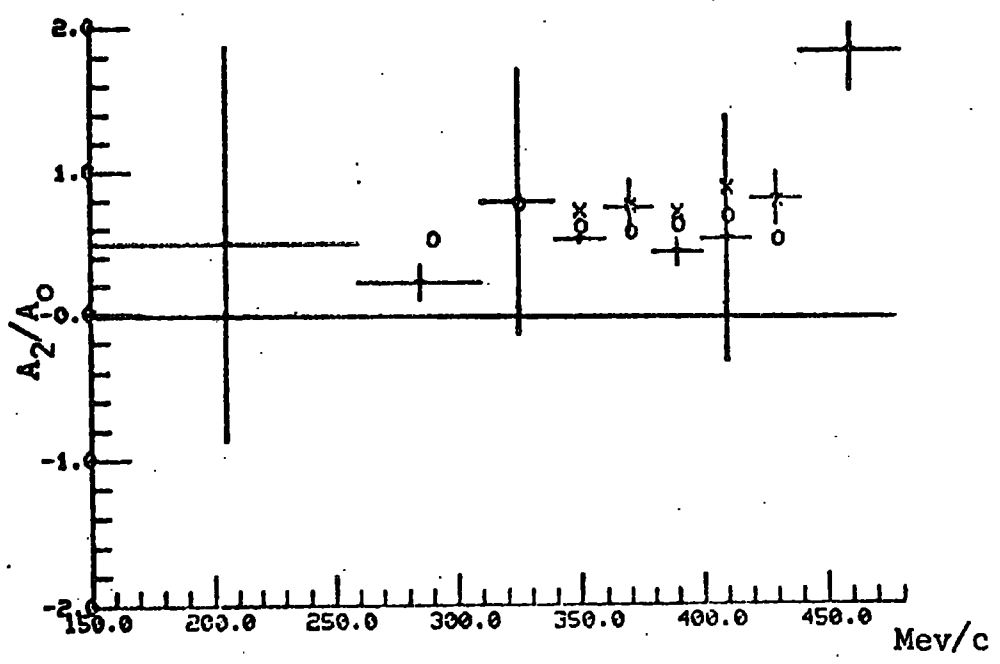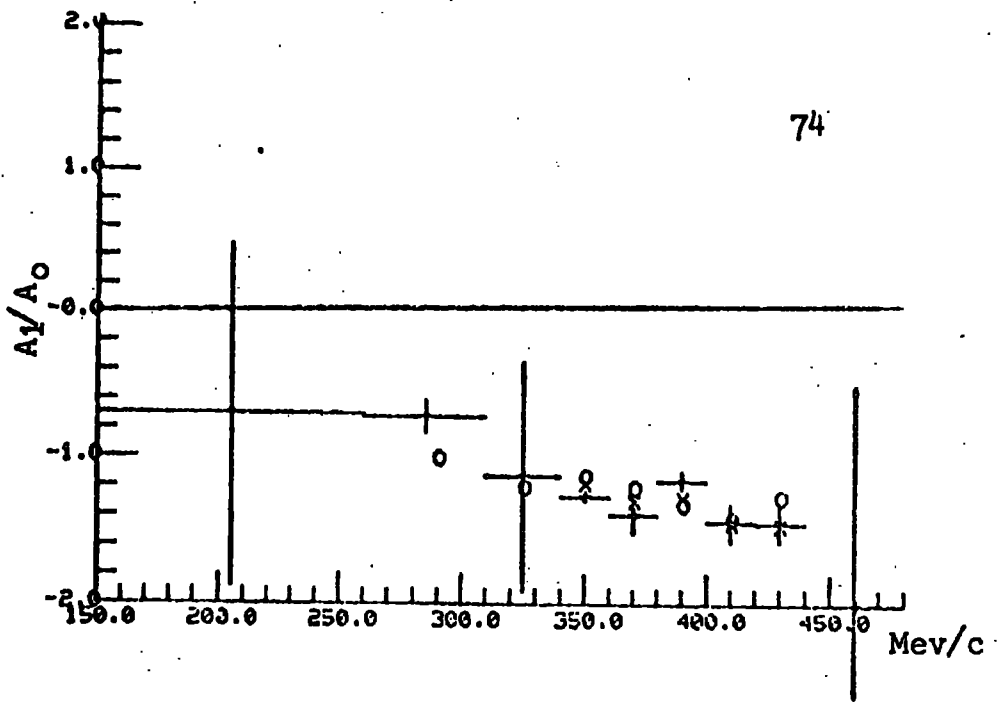
Fig 6-7

Production angular distribution Legendre coefficients as a function of momentum. $K^-p \to \Sigma^0 \pi^0$
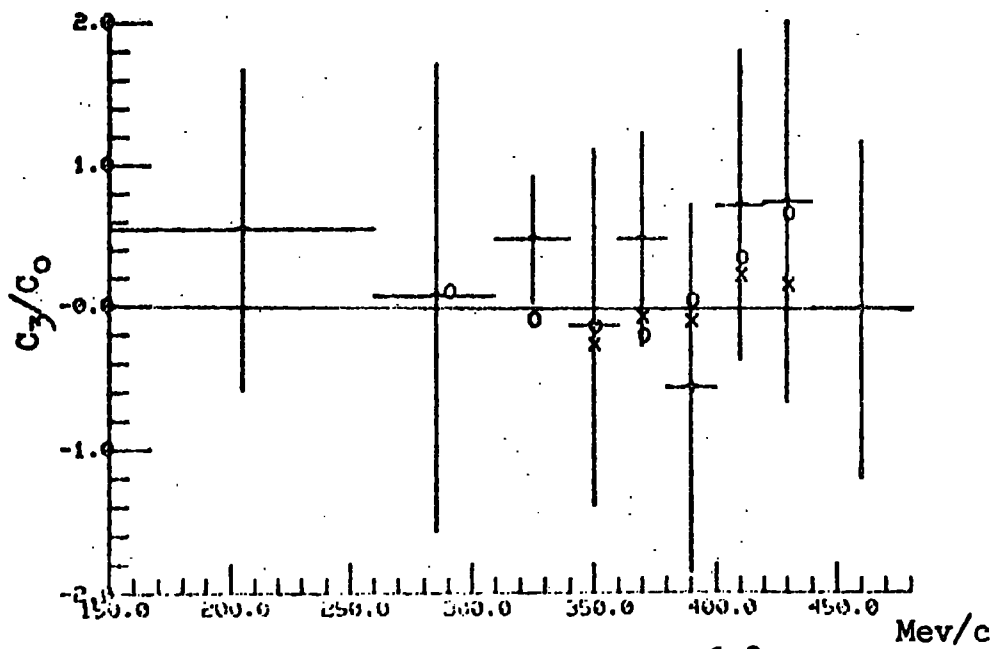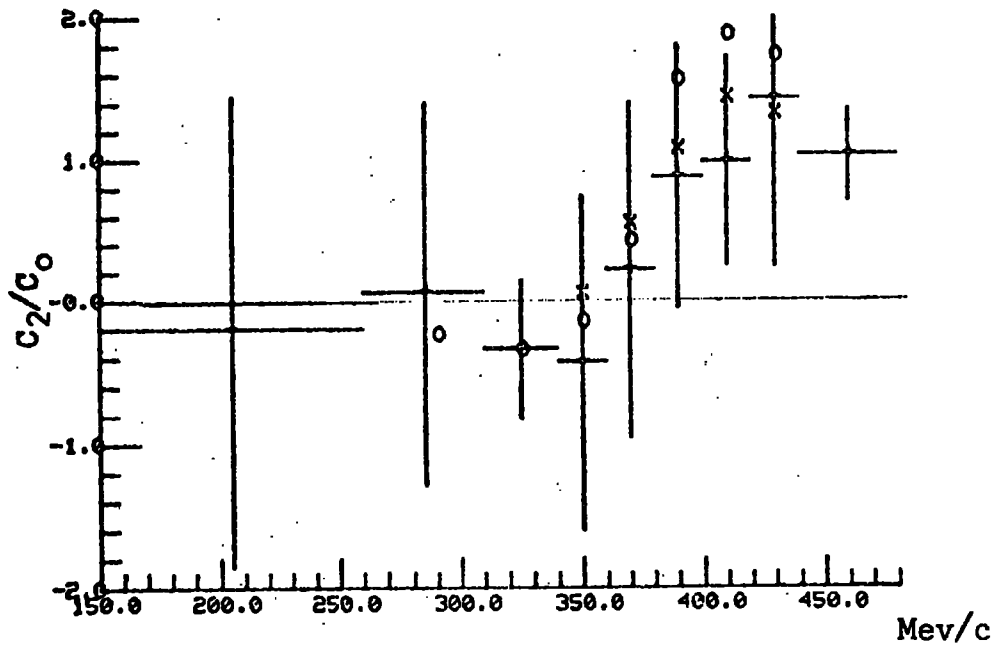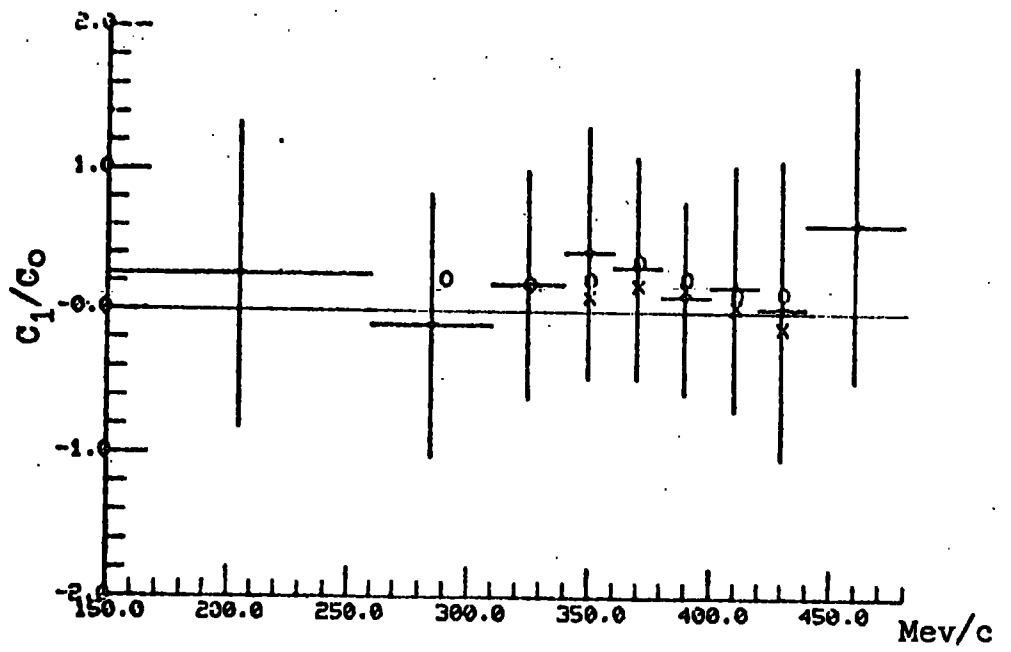
Fig 6-8

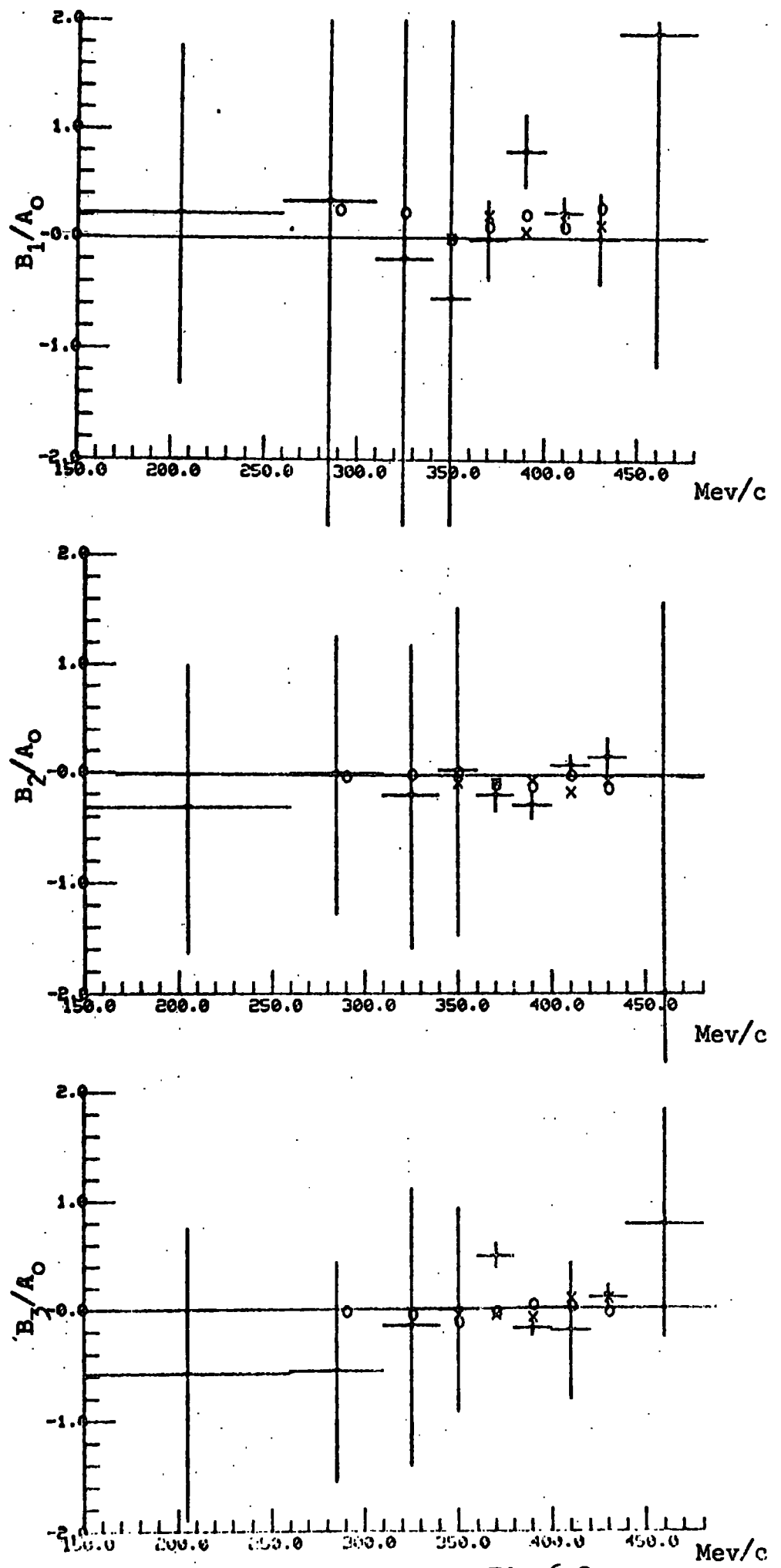Polarisation distribution Legendre coefficients as a function of momentum. $K^- p \rightarrow \Lambda^o \pi^o$

Fig 6-9

Polarisation distribution Legendre coefficients as a function of momentum. $K^- p \rightarrow \Sigma^\circ \pi^\circ$
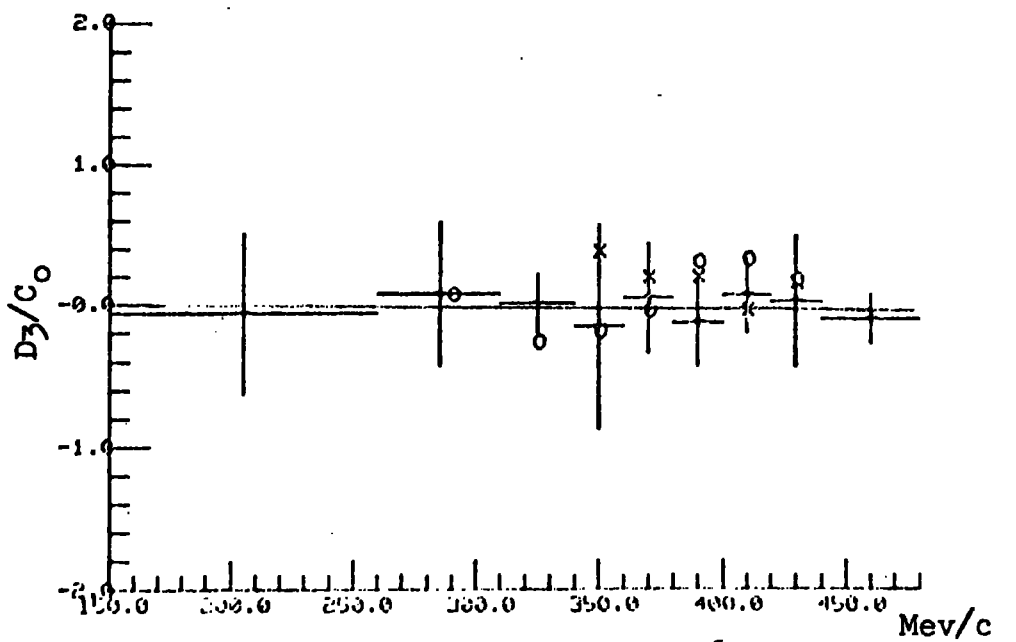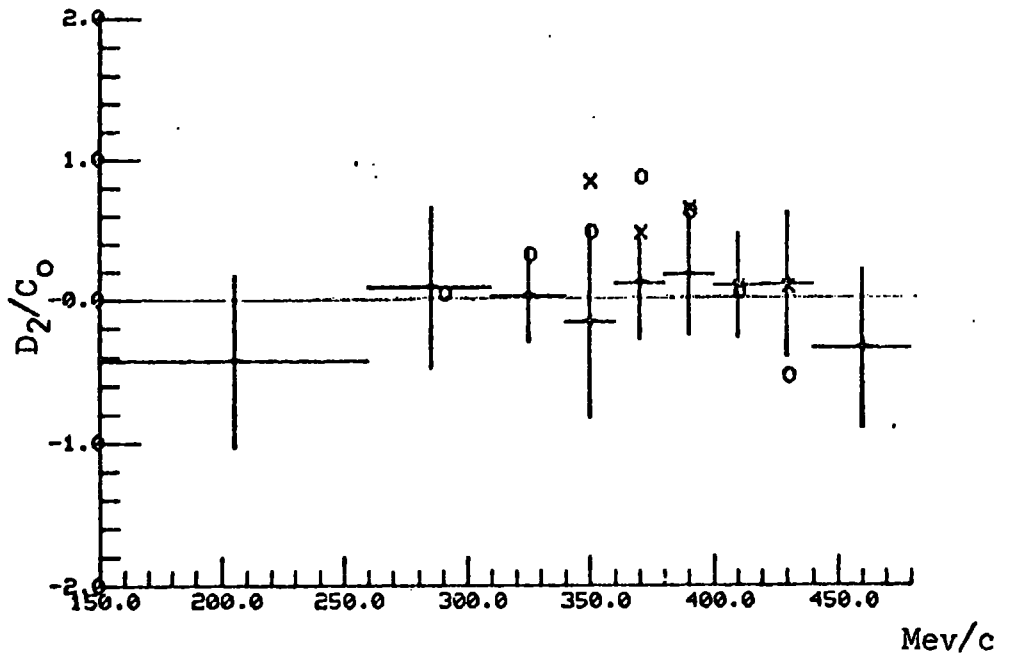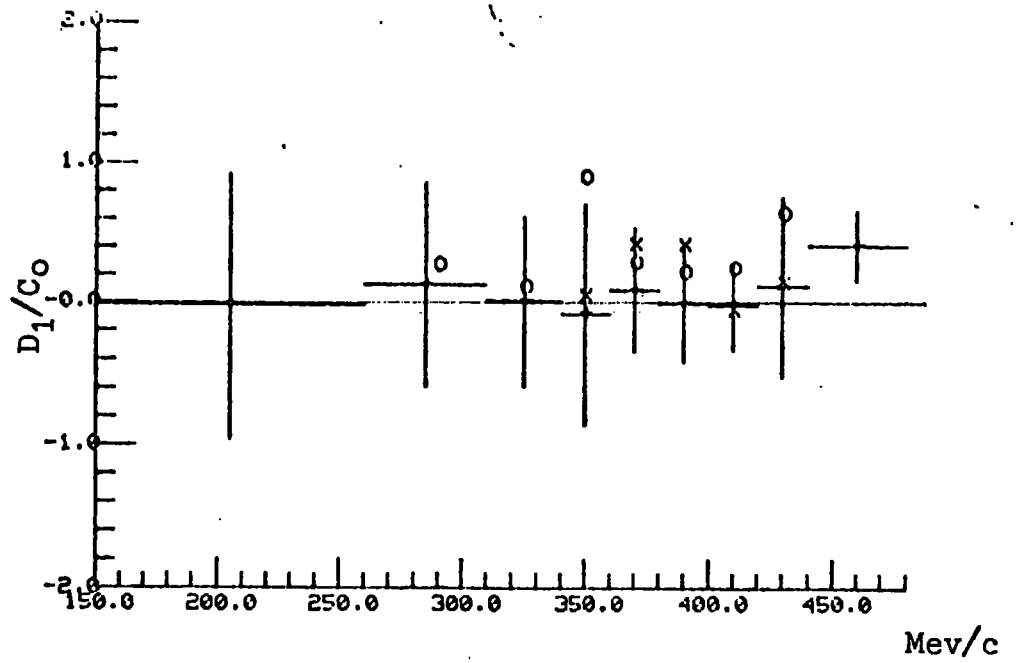
Fig 6-10

CHAPTER SEVEN

In this chapter, the events consisting of a Λ^o associated with one observed gamma ray (i.e. electron-positron pair) are considered and in particular the angular distribution from constrained fits to $K^-p \to \Lambda^o\pi^o$ and $K^-p \to \Sigma^o\pi^o$ channels are compared with those found in the last chapter. With only one gamma ray seen, the problem arises that this might have come from the π^o decay in the $K^-p \to \Sigma^o\pi^o$ channel. When this is the case, it is not kinematically possible to fit the interaction to the $\Sigma^o\pi^o$ channel and therefore there was a large proportion of events which fell into the no-fit category.

Recalling the problems in Chapter 5, the number of constrained fits to the $\Lambda^o\pi^o$ and $\Sigma^o\pi^o$ channels might have been surpressed by the sub-class of events with protons from the Λ^o stopping in the Perspex. However the fraction of such events in the sample of constrained fits is the same as for all Λ^o events and hence it has been assumed in this chapter that the constrained fits constitute a truely representative sample. This is not surprising, since the bias discussed in Chapter 5 is very small, of the order of $0.5 \ m^2_{\pi^o}$.

Since this chapter contains the first results of measurements on gamma rays in this experiment, the next section will deal with the expected features of gamma ray conversion and a comparison with the measurements. Section 7.2 uses the results of kinematic fitting the gamma rays to physical channels, to further check the measurements.
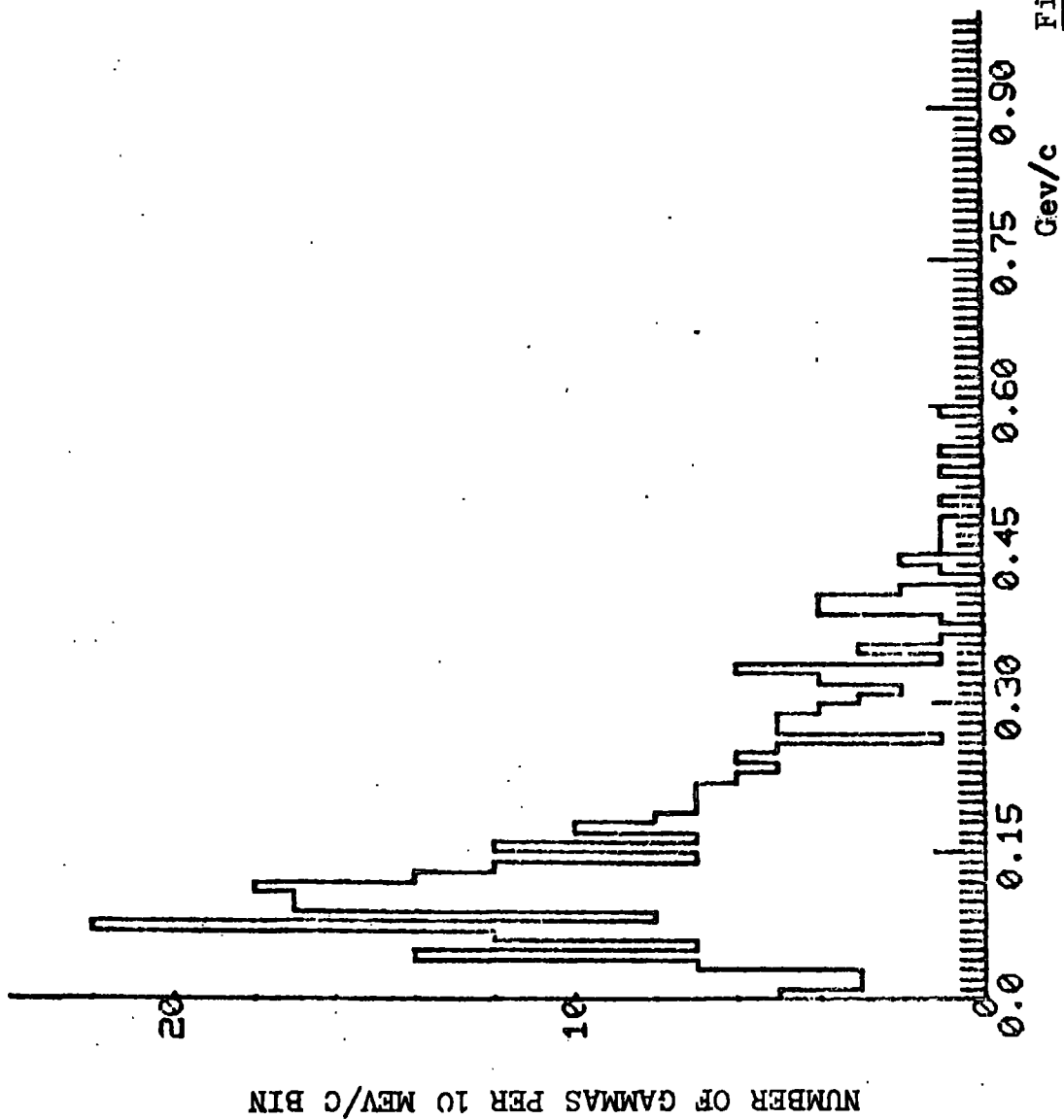
MOMENTUM DISTRIBUTION OF
MEASURED GAMMA RAYS

Fig 7-1

Finally the direct comparison of angular distributions is given in the last section.

7.1 ELECTROMAGNETIC INTERACTIONS

As the constrained fits considered in this chapter rely on pair production by gamma rays in the hydrogen-neon mixture, a closer examination of this phenomenon is necessary. The distribution of gamma ray energies is shown in fig 7.1. The energies range from 20 → 450 Mev. The Compton effect will not be dealt with, because the cross-section is not significant at these energies and events due to this process were not scanned for. The mean free path for the Compton effect is however included in figs 7.2a and 7.2b. The formulae given below are taken from Rossi ref 7.1. The curves shown in the figures have been calculated for this experiment.

Pair production is a quantum process that does not lend itself to classical description. The theory of pair production is closely related to that of radiation processes and consequently the equations are very similiar. The phenomenon is induced by the strong electric field that surrounds the nuclei. The nucleus which is nearest the photon materialisation, absorbs some of the momentum of the process, but because of its large mass it does not acquire any appreciable energy.

Therefore

$$E^* + E^{**} + 2\,m_e c^2 = E$$

where E^* and E^{**} are the energies of the electron and positron

Fig 7-2a

HYDROGEN

Fig 7-2b

HYDROGEN-NEON MIXTURE
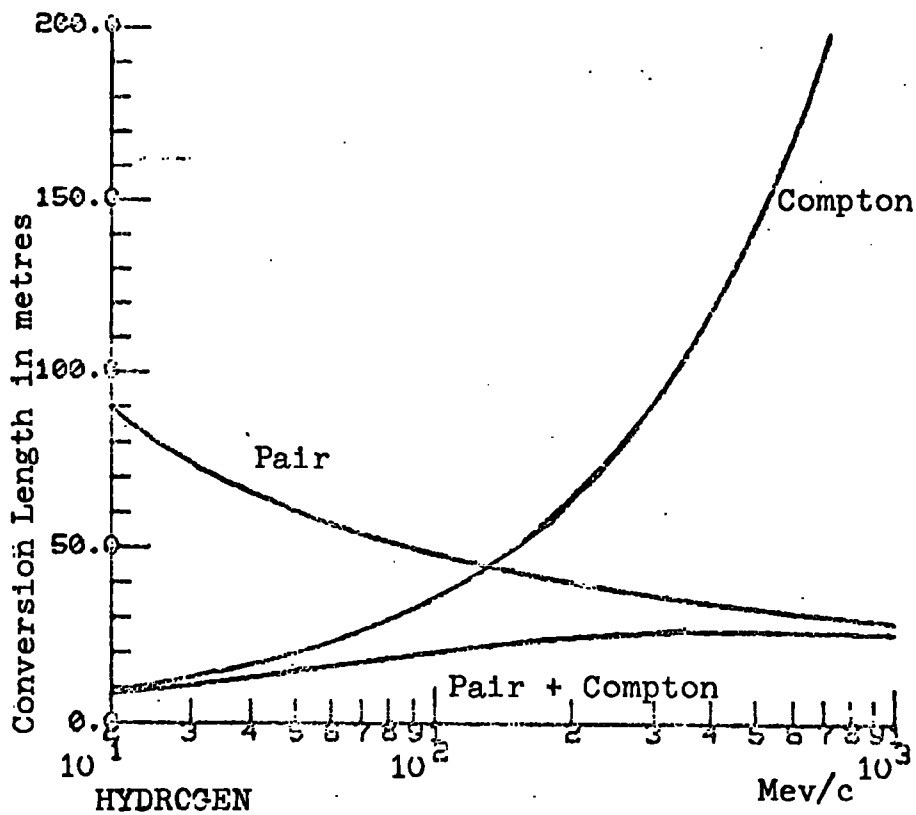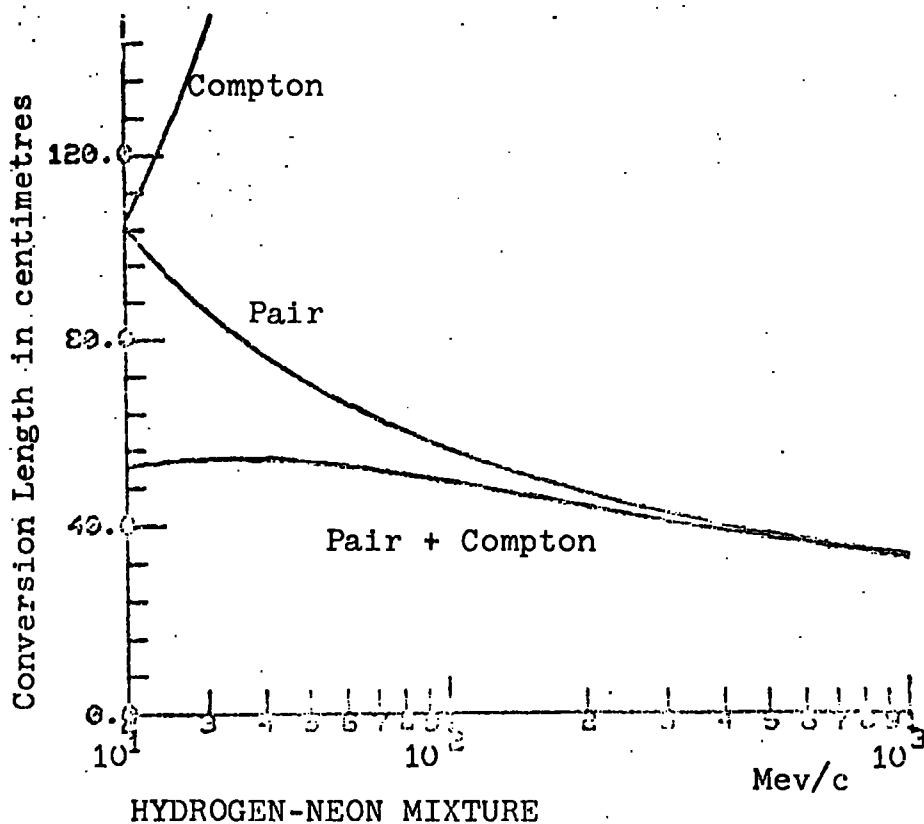
respectively, E is the energy of the photon, and m_e is the mass of the electron/positron.

Assuming $E \gg m_e c^2$ i.e. greater than 10 Mev/c , then $P(E,E^*)dE^*dx$ (which is the probability for a photon of energy E traversing a thickness of dx grms cm^{-2} to produce a pair, in which the positron has kinetic energy between E^* and $E^* + dE^*$) is given by :

$$P(E,E^*)dE^* = 4 \alpha \frac{NZ^2}{A} r_e^2 \frac{dE^*}{E} G(E,v)$$

where v is the fractional energy of the positron

$$v = \frac{E^* + m_e c^2}{E}$$

and $G(E,v)$ is a slowly varying function, $\alpha = 1/137$, N is Avogadro's number, Z and A are the charge and mass numbers of the material, and r_e is the classical radius of the electron.

Integration of $P(E,E^*)$ from $E^* = 0$ to $E^* = E - 2m_e c^2$ yields the total probability for a photon of energy E to produce a pair in a thickness of dx grms cm^{-2}. For the energy region of interest in this experiment , gamma energies lie between 20 → 450 Mev, this integration has to be done numerically. The results of the integration for both hydrogen and hydrogen-neon mixture are shown in figs 7.2a and 7.2b.

In this integration $G(E,v)$ was taken to be :

$$G(E,v) = [v^2 + (1-v)^2 + \frac{2v(1-v)}{3}] [\ln \left(\frac{2Ev(1-v)}{m_e c^2} \right) - 0.5]$$

(see ref 7.1 for further details).

For the mixture of neon and hydrogen the partial contributions were added together, the effective density for

Probability

1.00

>14J Mev/c

Actual data
cutoffs

>14U Me-/c

<8J Mev/c

<8U Mev/c

0.75

300 Mev/c

140 Mev/c

80 Mev/c

0.50

0.25

0.0
0.0   0.2   0.4   0.6   0.8   1.0

Fraction of gamma ray energy taken by the
positron

Fig 7-3

12

11

10

9

8

7

6

5

4

3

2

1

Number of events per 0.04 m^2 bin

0.0   0.60   1.20   1.80   2.40   3.00   3.60
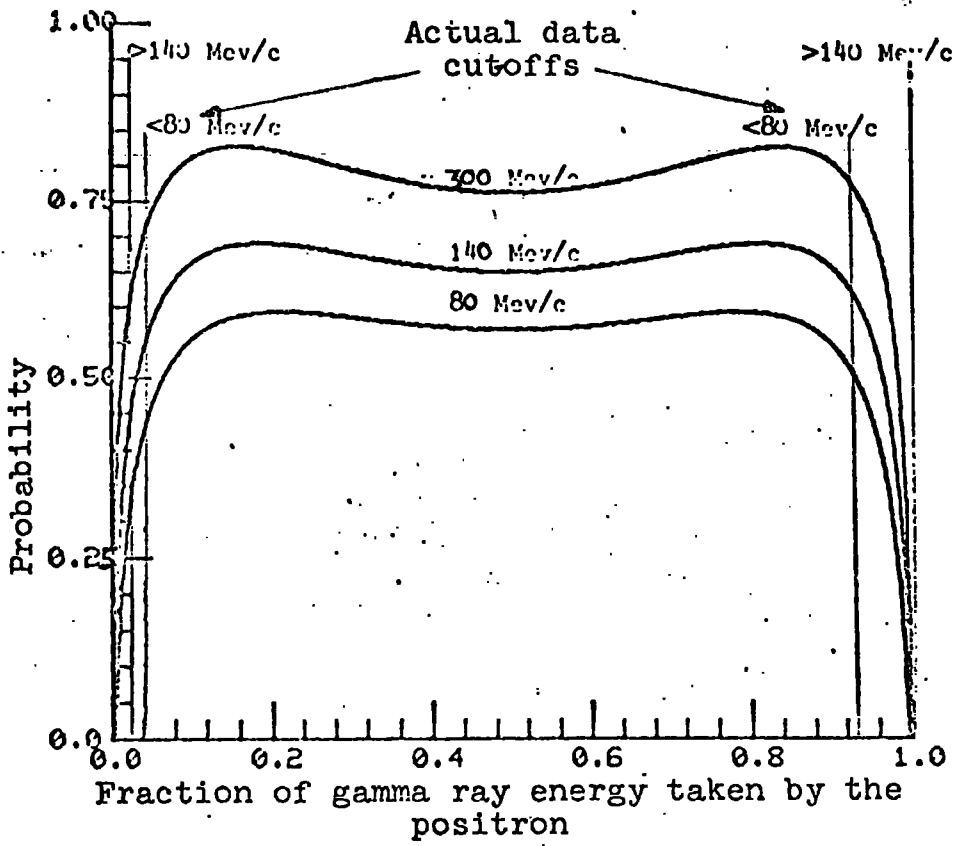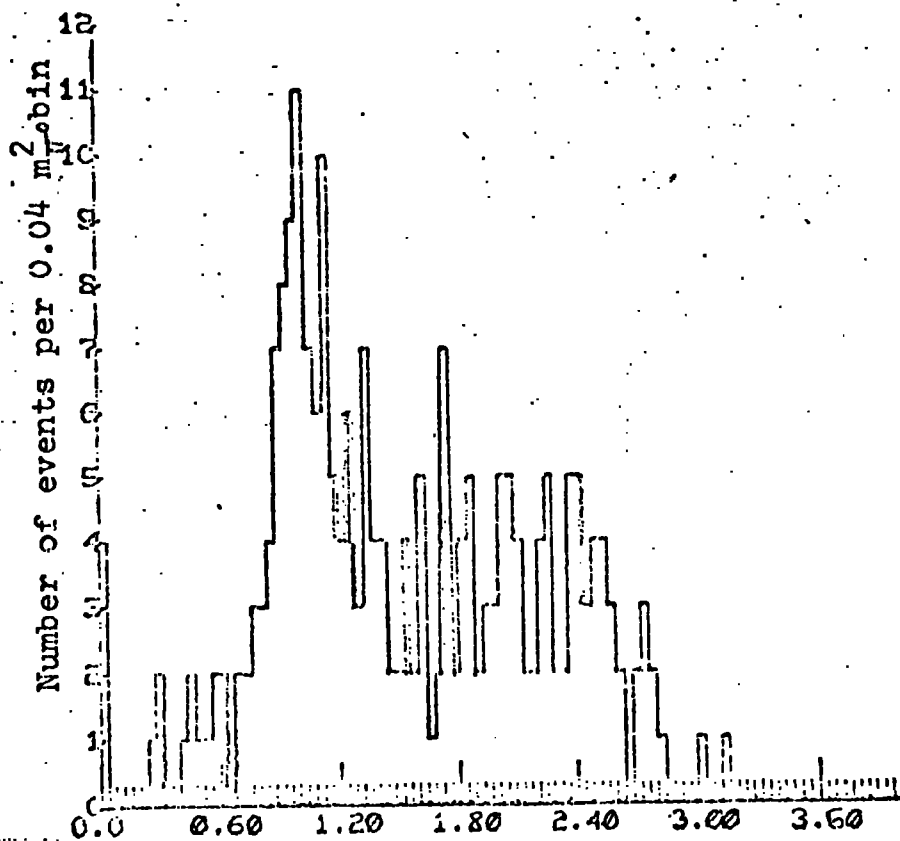
Fig 7-4

Invariant mass distribution of
gamma measured + gamma fitted in $K^- p \to \Lambda^0 \gamma$ (γ)

the components being 0.818 and 0.0229 grms cm^{-3} respectively. In fig 7.3 the fractional energy of the positron is plotted against the probability of getting that energy. The different curves are for different energies of incoming photons.

In the extreme regions of these curves, the gamma ray will have the appearance of a single arm (Compton) electron , and as mentioned above these were not scanned for. This situation is rectified somewhat, by measuring gamma rays with unequal pairs. The vertical lines on fig 7.3 show the observed position of the cutoffs, in the measurements of electron/ positron pairs, due to scanning and measuring losses for photon energies > 140 Mev and < 80 Mev. From fig 7.1, the bulk of the gamma ray energies lie between these values and the vertical lines represent the upper and lower limits of the cutoffs for the majority of the gamma rays. Such losses will of course simply reduce statistics and do not lead to a bias in investigating the K^-p interactions. Measuring gamma rays is complicated by the bremsstrahlung radiation losses of the electron and positron, presenting a difficult measuring problem. Checks were made to investigate possible biases in the gamma ray measurements and fitting, these are described in the next section.

7.2 GAMMA RAY CONSIDERATIONS

In order to investigate biases in the gamma ray measurements and fitting, a sample of events, which gave a kinematic fit of some description with the seen gamma rays, was checked. The sample was drawn from the $\Lambda^o \pi^o$ events.

Since the momentum spectrum of the K^- mesons is heavily weighted to the $\Lambda(1520)$ region, it is expected that the $\Lambda^0\pi^0$ channel will only make up $30 \to 50\%$ of the total sample. As mentioned in the introduction to this chapter most of the Λ^0 + one gamma events should not give a fit to a physical channel. However by including the hypothesis $K^-p \to \Lambda^0\gamma \, (\gamma)$, 80% of the events gave a fit of some kind including the gamma ray. In fig 7.4, the invariant mass is shown , obtained from the measured gamma ray and the fitted (unseen) gamma in the hypothesis $\Lambda^0\gamma(\gamma)$. The π^0 peak is clearly observed and has an intensity of about 35% of the total as expected. (i.e. 35% $\Lambda^0\pi^0$ in the $\Lambda(1520)$.)

Fig 7.5 shows a scatter plot of measured gamma ray energy against the value fitted to the physically constrained final state $K^-p \to \Lambda^0\pi^0$, $\pi^0 \to \gamma$ (seen) γ(fitted). This shows a satisfactory unbiassed spread of the measurements around the fitted values.

As an additional check, the point Λ^0 fit was combined with the measured gamma ray information and a missing mass squared found to the $\Lambda^0 + \gamma$ combination. Theoretically this missing mass squared distribution in units of $m^2_{\pi^0}$ should consist of δ-functions at 0 and 1 corresponding to the $\Lambda^0\pi^0$ and $\Sigma^0\pi^0$ channel where the gamma ray comes from the Σ^0 decay, superimposed on a continuous distribution between zero and approximately 2. The continuum arises from the two gamma combinations formed when the observed gamma is from the π^0 in the $\Sigma^0\pi^0$ channel.

Fig 7-5

Missing mass squared to Λ^0 + seen gamma   Fig 7-6

The distribution obtained is shown in fig 7.6. The peak at zero is clearly seen. The contribution from the Σ^0 at 1 is less obvious on these statistics but this is not too surprising since the signal can only occur for 33% of that channel.

7.3 THE $\Lambda^0 \pi^0$ AND $\Sigma^0 \pi^0$ CONSTRAINED CHANNELS

As explained in Chapter 4, the data for this thesis is from the first measure only. This and reasons given above account for the low statistics availiable for the Λ^0 + one gamma events.

In view of these statistics, only a comparison of the production angular distributions predicted by the results obtained in Chapter 6 for the momentum bin 340 → 440 Mev/c is made with that directly obtained from the constrained fits to the $\Lambda^0 \pi^0$ and $\Sigma^0 \pi^0$ channels.

As a preliminary to these comparisons the angular distribution of the gamma was found for the $\Sigma^0 \pi^0$ channel in the rest system of the Σ^0 (θ_γ**). This distribution is shown in fig 7.7; it should be isotropic but there is a significant excess in the bin $-0.6 > \cos \theta_\gamma^{**} > -0.4$. Unfortunately there are not the statistics to investigate this properly. For this distribution the Λ^0/Σ^0 ambiguous events were all taken to be $\Sigma^0 \pi^0$ events. For fig 7.8 the ambiguity was resolved by accepting the events as the channel with the highest χ^2 probability. This distribution still has an excess in the same bin, but it is reduced.

The production angular distributions are shown in fig 7.9
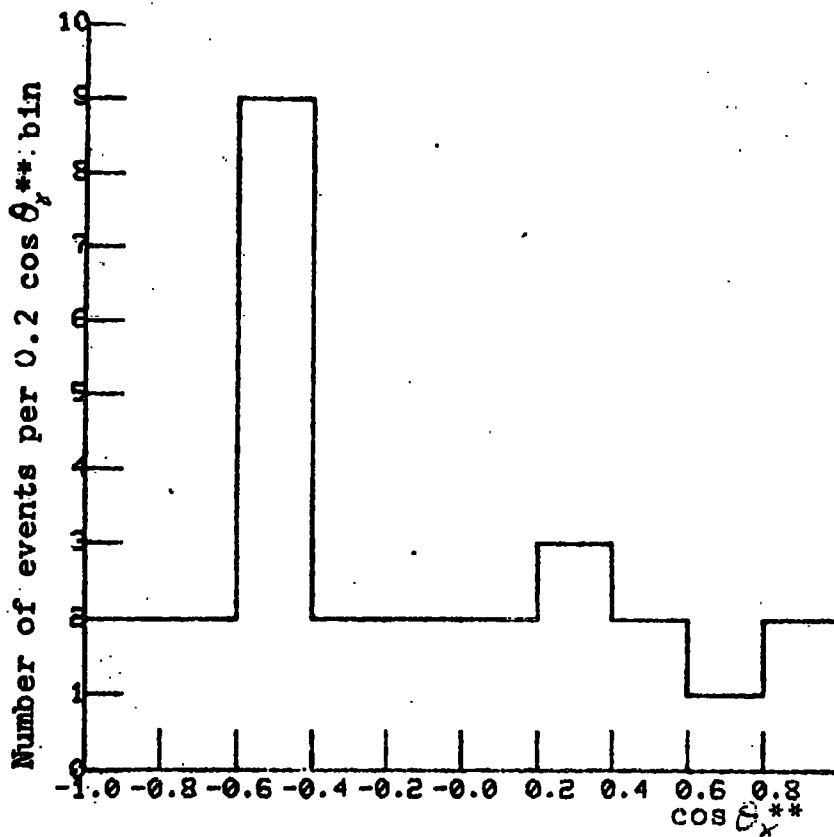
Fig 7-7

Angular distribution of gamma in rest frame of Σ^o
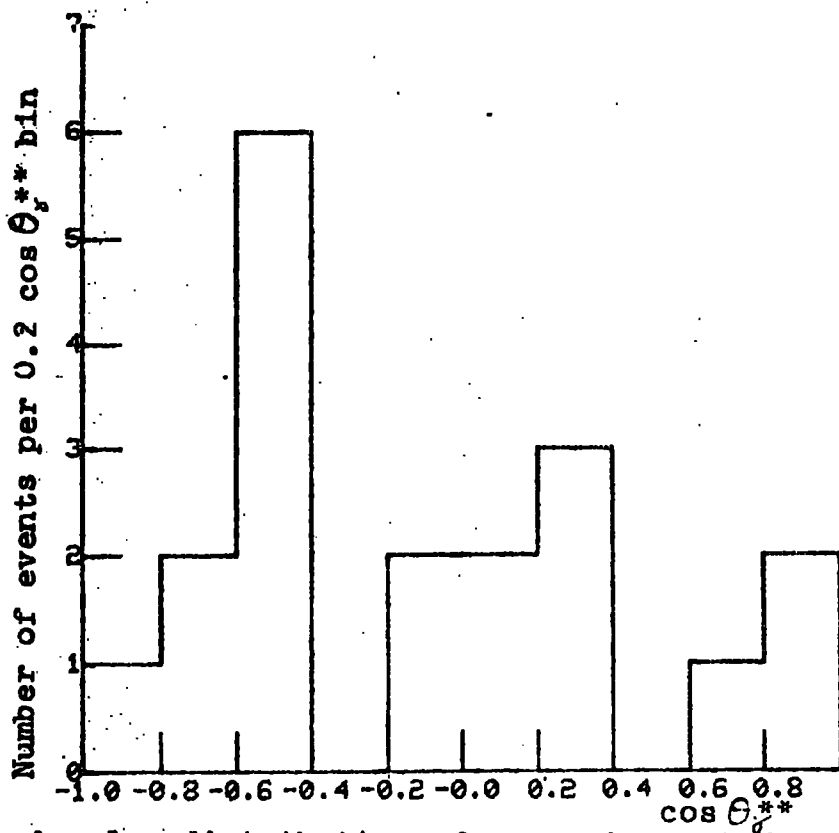
Fig 7-8

Angular distribution of gamma in rest frame of Σ^o
ambiguities resolved by probability.
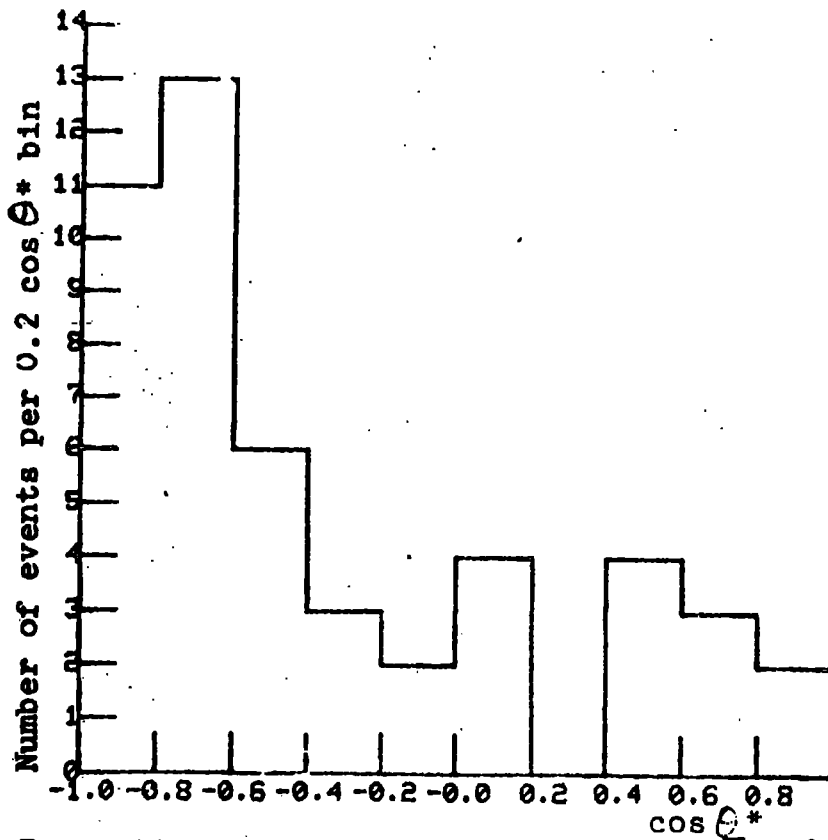
Fig 7-9

Production angular distribution for $K^-p \to \Lambda^0 \pi^0$

Fig 7-10
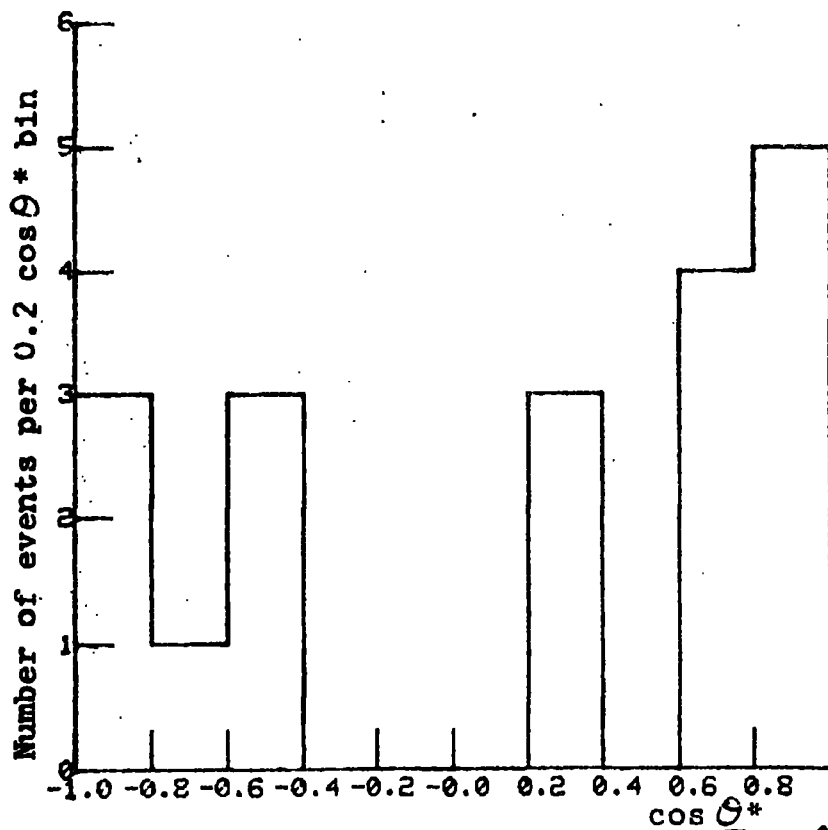
Production angular distribution for $K^-p \to \Sigma^0 \pi^0$

and fig 7.10 for the $\Lambda^0\pi^0$ and $\Sigma^0\pi^0$ channels respectively. The same probability criterion was used for ambiguous events as above. The distributions show the same shapes as those determined by the likelihood function and missing mass squared analyses in Chapter 6. The points (*) plotted on fig 7.11 show these distributions compared directly with those obtained in Chapter 6. Allowing for the very small statistics the agreement is very good. With the increased number of events which will be available at a later stage it will be possible to determine the angular distributions of these channels directly without resorting to the methods detailed in Chapter 6.

$K^-p \rightarrow \Lambda^0\pi^o$

$\cos\Theta *$

$K^-p \rightarrow \Sigma^0_\pi{}^0$

$\cos\Theta*$
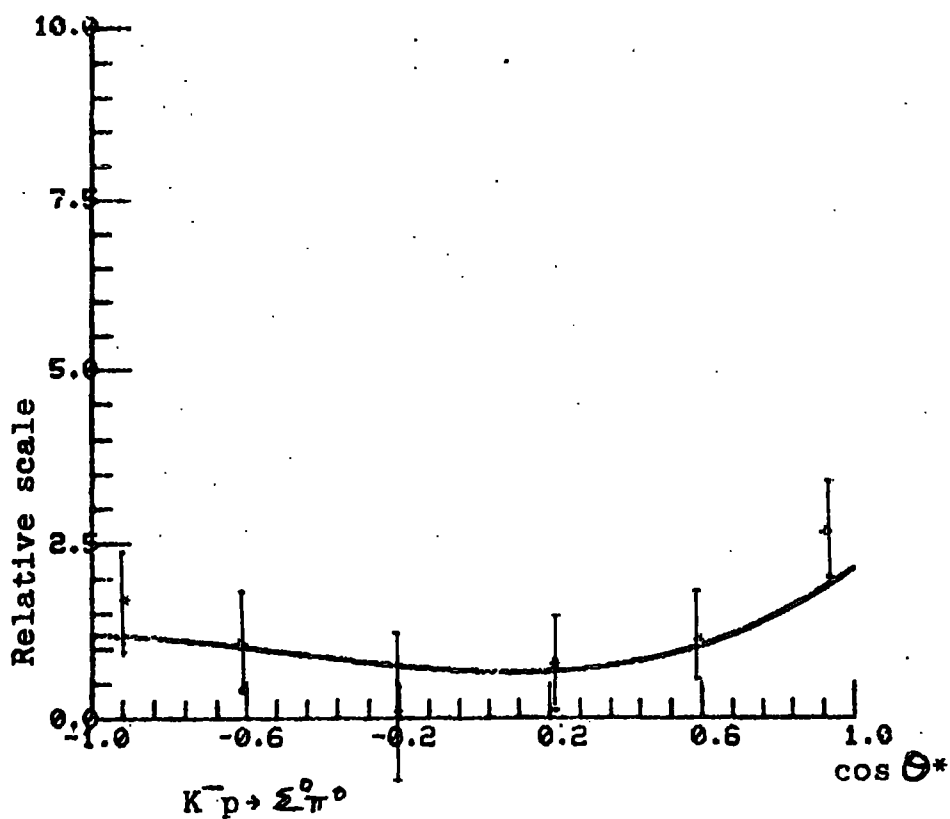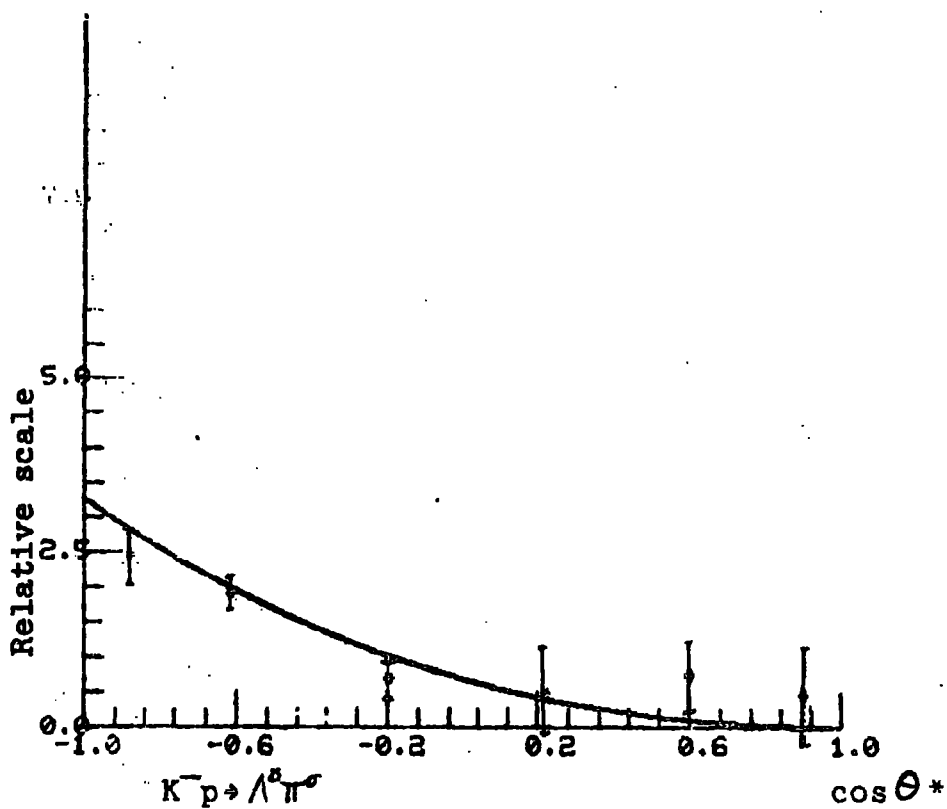
Constrained fit production angular
distributions compared directly with those
obtained in Chapter 6.

<u>Fig 7-11</u>

CHAPTER EIGHT

In this chapter, the results in previous chapters are briefly discussed and an outline of the statistics that will be available at the conclusion of the processing chain is given.

As has been explained in Chapters 4 and 7, the current statistics of this experiment are low. When the processing of events is concluded these statistics will not be large compared with, say, counter experiments. This is inherent in the bubble chamber technique. However, due to the complexity of the final states and the complex patterns of tracks, of diverse bubble density in the pictures (due to observing tracks through essentially three bubble chambers - hydrogen-neon mixture, T.S.T., hydrogen-neon mixture),it is very difficult to conceive a single experiment based on non-visual detectors (i.e. counter experiments) to measure all channels simultaneously, particularly one which could cover the complete solid angle. Thus a combination of low data collecting rate, inherent in bubble chamber experiments, and the preliminary stage of processing of events reached, has led to severely restricted statistics being available for these analyses.

It is proposed to normalise this experiment with the tau decays (see section 3.1.1) of the kaons. These decays will give a measure of the K⁻ path length in this experiment as a function of momentum. However it is not reasonable to normalise the branching ratios given in Chapter 5 to absolute cross-sections with the partial statistics currently available.

However this will be possible when the final D.S.T. s of events are ready.(See ref 8.1 for details of normalisation using tau decays of kaons).

8.1 THE Λ (1520) RESONANCE IN THE DATA

Despite the preliminary nature of the data available the analyses detailed in previous chapters has shown three features regarding the $K^-p \rightarrow \Lambda^o$ + neutrals channels.

i) Using all the Λ^os that with fitting in KINEMATICS point to a K^- ending in the T.S.T, it was found,(Chapter 5), that there was good agreement between the present and existing data for the fraction of the channel going into $\Lambda^o\pi^o$. In particular, the presence of the $\Lambda(1520) \rightarrow \Sigma^o\pi^o$ is clearly demonstrated, the former final state being $20.3 \pm 5\%$ of the total at the resonance energy. This is to be compared with $27 \pm 0.6\%$ from the high statistics experiment of Tripp et.al. There are no features in the region of the possible $\Sigma(1480)$ although no definite conclusions should be drawn at this present stage of the experiment.

ii) Also using all the point Λ^o events, a repeat of Tripp's maximum likelihood analysis yields good agreement for the coefficients of the Legendre polynomials used to describe the production angular distributions of the Λ^o and Σ^o . The statistics are too limited to achieve much precision particularly for the coefficients describing the polarisations but there is internal consistency between the analyses of Chapters 5 and 6 (see section 6.2). In particular the dominance of the coefficient for l = 2 in the $\Lambda(1520)$ region

for the $\Sigma^{0}\pi^{0}$ channel is clearly demonstrated. There are no particular features at other momenta, again presenting no evidence for the Σ (1480).

iii) The use of the T.S.T. is an embarrassment for the analyses of the type outlined in Chapters 5 and 6 , since it represents a smaller hydrogen chamber than would be chosen for an experiment without gamma ray detection. However in Chapter 7 is seen a comparison of the angular · distributions obtained directly from the fits to $\Sigma^{0}\pi^{0}$ and $\Lambda^{0}\pi^{0}$ channels, using the gamma ray information, with those derived from the coefficients obtained earlier . Even with the small statistics, the agreement is very encouraging. Some problems evidently may arise in the ambiguities in these fitted channels, but they may be well enough localised to be handled easily (see figs 7.7 and 7.11).

8.2 ESTIMATES OF FINAL STATISTICS

Currently there are 1560 events in the momentum region 150 to 480 Mev/c. This includes some 167 events with a seen gamma ray. As explained in Chapter 4 (section 4.2), a further detailed scan was done at the judging stage and any events with additional associated gamma rays were put into the remeasure chain.

When the remeasures are ready, the following estimated total statistics should be availiable in the momentum region 150 to 480 Mev/c :-

Overall total Λ^{0} + neutrals	= 2400
Of this total Λ^{0} + one gamma ray	= 900

$$\Lambda^o + \text{two gamma rays} = 120$$

$$\Lambda^o + \text{three gamma rays} = 6$$

It is important to emphasise that this represents the Durham statistics only. These figures should be scaled by approximately 3 to 4 to find the overall estimated number of Λ^o + neutrals events.

The Λ^o + one gamma events can be broken down to give approximate estimates of the number of constrained fits. The approximate numbers are as follows :

$$K^- p \rightarrow \Lambda^o \pi^o = 200 \text{ events}$$

$$K^- p \rightarrow \Sigma^o \pi^o = 80 \text{ events}$$

$$\text{Ambiguous } \Lambda^o / \Sigma^o = 80 \text{ events}$$

Again these can be scaled by 3 to 4 to find the collaboration's overall statistics for these constrained channels.

APPENDICES

In view of the large number of mathematical symbols used in these appendices, they are written in script.

APPENDIX A

ERROR ON THE MISSING MASS SQUARED

$$MMSQ = \left(q_i - q_\Lambda \right)^2$$

$$= m_K^2 + m_p^2 + m_\Lambda^2 + 2 E_K m_p$$
$$- 2 E_K E_\Lambda - 2 m_p E_\Lambda + 2 p_K p_\Lambda \cos\theta$$

where these terms have been defined in Chapter 5 (section 5.2)

$$EMMSQ = \frac{\partial MMSQ}{\partial p_K} E\left(1/p_K\right) p_K^2 + \frac{\partial MMSQ}{\partial \phi_K} \frac{\partial \phi_K}{\partial p_K} E\left(1/p_K\right) p_K^2$$

$$+ \frac{\partial MMSQ}{\partial \phi_K} E\left(\phi_K\right) + \frac{\partial MMSQ}{\partial \lambda_K} \frac{E\left(\tan\lambda_K\right)}{\sec^2\lambda_K}$$

$$+ \frac{\partial MMSQ}{\partial p_\Lambda} E\left(1/p_\Lambda\right) p_\Lambda^2 + \frac{\partial MMSQ}{\partial \phi_\Lambda} E\left(\phi_\Lambda\right) + \frac{\partial MMSQ}{\partial \lambda_\Lambda} \frac{E\left(\tan\lambda_\Lambda\right)}{\sec^2\lambda_\Lambda}$$

$$(A.1)$$

Taking each term in turn :

$$\frac{\partial MMSQ}{\partial p_K} = 2\left(\frac{m_p p_K}{E_K} - \frac{p_K E_\Lambda}{E_K} + p_\Lambda \cos\theta \right).$$

$$\frac{\partial MMSQ}{\partial p_\Lambda} = 2\left(-\frac{p_\Lambda E_K}{E_\Lambda} - \frac{m_p p_\Lambda}{E_\Lambda} + p_K \cos\theta \right)$$

$$\cos\theta = \cos\lambda_K \cos\phi_K \cos\lambda_\Lambda \cos\phi_\Lambda + \cos\lambda_K \sin\phi_K \cos\lambda_\Lambda \sin\phi_\Lambda$$

$$+ \sin\lambda_K \sin\lambda_\Lambda$$

$$\therefore \quad \frac{\partial MMSQ}{\partial \phi_K} = 2 p_K p_\Lambda \cos \lambda_K \cos \lambda_\Lambda \sin (\phi_\Lambda - \phi_K)$$

$$\frac{\partial MMSQ}{\partial \phi_\Lambda} = 2 p_K p_\Lambda \cos \lambda_K \cos \lambda_\Lambda \sin (\phi_K - \phi_\Lambda)$$

$$\frac{\partial MMSQ}{\partial \lambda_K} = 2 p_K p_\Lambda \left\{ \cos \lambda_K \sin \lambda_\Lambda - \sin \lambda_K \cos \lambda_\Lambda \cos (\phi_K - \phi_\Lambda) \right\}$$

$$\frac{\partial MMSQ}{\partial \lambda_\Lambda} = 2 p_K p_\Lambda \left\{ \cos \lambda_\Lambda \sin \lambda_K - \sin \lambda_\Lambda \cos \lambda_K \cos (\phi_K - \phi_\Lambda) \right\}$$

Before considering $\frac{\partial MMSQ}{\partial p_K}$ it is useful to look at the swimming of errors on momentum for the K^- track, from the centre of track to the interaction vertex (there is no swimming for the Λ^0 as it neutral and therefore is unaffected). The change in $E(\phi)$ and $E(\tan \lambda)$ errors is negligible with swimming and therefore the centre of track values have been used to calculate EMMSQ.

The range of a track is connected to its momentum as follows :

$$R = K \rho^n$$

where K is a constant and n = 3.6

$$R_c = K p_c^n$$

$$p_v = \left[\frac{1}{K} (R_c - L) \right]^{1/n}$$

where L is the length of track from the centre to the interaction vertex, and P_v and P_c are the momenta at the vertex and centre of track respectively.

$$E\left(P_v\right) = \frac{dP_v}{dR_c} \frac{dR_c}{dP_c} \; F\left(P_c\right)$$

$$\frac{dP_v}{dR_c} = \frac{P_v}{n}\left(R_c - L\right)^{-1} \qquad \qquad \ldots\ldots (\,A.2)$$

$$\frac{dR_c}{dP_c} = n\,k\,P_c^{n-1} \qquad \qquad \ldots\ldots (\,A.3)$$

$$\therefore \quad E(P_v) = P_v^{1-n}\,P_c^{n-1}\,E(P_c)$$

$$E\left(\frac{1}{P}\right) = -\frac{E(P)}{P^2}$$

$$\therefore \quad E\left(\frac{1}{P_v}\right) = P_v^{1-n}\cdot P_v^{-2}\cdot P_c^{2}\,P_c^{n-1}\,E\left(\frac{1}{P_c}\right)$$

$$E\left(\frac{1}{P_v}\right) = \left(\frac{P_c}{P_v}\right)^{n+1}E\left(\frac{1}{P_c}\right)$$

Now to evaluate the $\dfrac{\partial\phi}{\partial P_\kappa}$

The change in azimuth angle $d\phi$ caused by moving a small distance dl is given by :

$$\frac{d\phi}{dl} = -\frac{\beta}{P(l)}$$

where B is the magnetic field.

$$\left(R_c - l\right) = K \, \rho(l)^n$$

$$d\phi = \frac{-B \, K^{-1/n}}{\left(R_c - l\right)^{1/n}} \, dl \, .$$

$$\int_{\phi_c}^{\phi_v} d\phi = -B \, K^{-1/n} \int_0^L \frac{dl}{\left(R_c - l\right)^{1/n}}$$

This gives

$$\phi_v - \phi_c = B K^{-1/n} \frac{n}{n-1} \left[\frac{R_c - L}{\left(R_c - L\right)^{1/n}} - \frac{R_c}{\left(R_c\right)^{1/n}} \right]$$

Rearrange

$$= B \frac{n}{n-1} \left[\frac{R_c - L}{\rho_v} - \frac{R_c}{\rho_c} \right]$$

$$= B \frac{n}{n-1} \left[K \rho_c^n \left(\frac{1}{\rho_v} - \frac{1}{\rho_c} \right) - \frac{L}{\rho_v} \right]$$

$$\therefore \quad \frac{\partial \phi_v}{\partial \rho_v} = \frac{Bn}{n-1} \left[K \frac{\partial}{\partial \rho_v} \left(\frac{\rho_c^n}{\rho_v} - \rho_c^{n-1} \right) + \frac{L}{\rho_v^2} \right]$$

$$= \frac{Bn}{n-1} \left[K \frac{\rho_c^{n-1}}{\rho_v} n \frac{d\rho_c}{d\rho_v} - \frac{K \rho_c^n}{\rho_v^2} - K(n-1) \rho_c^{n-2} \frac{d\rho_c}{d\rho_v} + \frac{L}{\rho_v^2} \right]$$

Using equations A.2 and A.3

for

$$\frac{\partial \rho_c}{\partial \rho_v} = \frac{\partial R_c}{\partial \rho_v} \cdot \frac{\partial \rho_c}{\partial R_c}$$

gives

$$\frac{\partial P_c}{\partial P_v} = \left(R_c - L\right)\frac{P_c^{1-n}}{K P_v}$$

$$\therefore \quad \frac{d\emptyset}{\partial P_K} = \frac{\beta n}{P_v}\left(R_c - L\right)\left[\frac{1}{P_v} - \frac{1}{P_c}\right]$$

All the terms in the expression for EMMSQ (eqn A.1) can now be evaluated in terms of known variables. Each term was calculated by computer program and then squared, correlation between terms was taken to be zero, the sum of these squares was then taken to be the variance of the MMSQ and used in the analyses outlined in Chapters 5 and 6. See Chapter 5 for further discussion.

APPENDIX B

THE $\Sigma^0\pi^0$ CHANNEL PRODUCTION ANGULAR DISTRIBUTION

The production angular distribution for the channel is expressed, in Chapter 6 as follows :

$$\frac{dN}{d\left(\cos\Theta_\Sigma^*\right)} = \sum_\ell C_\ell^\circ \, P_\ell\left(\cos\Theta_\Sigma^*\right)$$

$\cos\Theta_\Sigma^*$ is unknown ; the known angles are $\cos\Theta_\Lambda^*$ and $\cos x$, the angle between the Σ^0 and Λ^0 . To resolve this problem, an addition theorem obeyed by Legendre polynomials is used. If (Θ_1, ϕ_1) and (Θ_2, ϕ_2) define two directions in space such that $\Theta_1 + \Theta_2 < \pi$, and if ψ is the angle between them then :

$$\cos\psi = \cos\Theta_1 \cos\Theta_2 + \sin\Theta_1 \sin\Theta_2 \cos\left(\phi_1 - \phi_2\right)$$

and the addition theorem is that :

$$P_\ell\left(\cos\psi\right) = \left(\frac{4\pi}{2\ell+1}\right) \sum_{m=-\ell}^{+\ell} Y_{\ell m}\left(\Theta_1, \phi_1\right) Y_{\ell-m}\left(\Theta_2, \phi_2\right)$$

In terms of the angles in fig 6.2 and 6.3

$$P_\ell\left(\cos\Theta_\Sigma^*\right) = \frac{4\pi}{2\ell+1} \sum_{m=-\ell}^{+\ell} Y_{\ell m}\left(x, \phi\right) \cdot Y_{\ell-m}\left(\Theta_\Lambda^*, 0\right)$$

$$Y_{\ell m}\left(\Theta, \phi\right) = (-1)^m \left\{\frac{(2\ell+1)}{4\pi} \frac{(\ell-m)!}{(\ell+m)!}\right\}^{\frac{1}{2}} P_\ell^m\left(\cos\Theta\right) e^{im\phi}$$

and

$$Y_{l,-m}(\theta,\phi) = (-1)^m Y_{l,m}^*(\theta,\phi)$$

for m = 0

$$Y_{l,0}(\theta,\phi) = \left(\frac{2l+1}{4\pi}\right)^{1/2} P_l(\cos\theta)$$

Therefore in the $P_l(\cos\theta_\varepsilon^*)$ expression the contribution from m = 0 is :

$$P_l(\cos\theta_\Lambda^*) P_l(\cos x)$$

for m = +n or -n then the contribution is :

$$\frac{4\pi}{2l+1}\left(Y_{l,n}(x,\phi)\, Y_{l,-n}(\theta_\Lambda^*,0) + Y_{l-n}(x,\phi)\, Y_{ln}(\theta_\Lambda^*,0)\right)$$

which gives :

$$(-1)^n\frac{4\pi}{2l+1}\left[Y_{ln}(x,\phi)\, Y_{ln}^*(\theta_\Lambda^*,0) + Y_{ln}^*(x,\phi)\, Y_{ln}(\theta_\Lambda^*,0)\right]$$

$$= (-1)^n P_l^n(\cos\theta_\Lambda^*)\left[P_l^n(\cos x)\, e^{in\phi} + P_l^n(\cos x)\, e^{-in\phi}\right]\frac{(l-n)!}{(l+n)!}$$

$$= 2(-1)^n P_l^n(\cos\theta_\Lambda^*)\, P_l^n(\cos x)\cos n\phi$$

$$P_l(\cos\theta_\varepsilon^*) = P_l(\cos\theta_\Lambda^*) P_l(\cos x) + 2\sum_{m=1}^{l}(-1)^m P_l^m(\cos\theta_\Lambda^*)\, P_l^m(\cos x)\cos m\phi$$

Integrating over ϕ gives :

$$\int_0^{2\pi} P_\ell(\cos\Theta_\varepsilon^+) \, \frac{d\phi}{2\pi} \;=\; P_\ell(\cos x) \, P_\ell(\cos\Theta_\Lambda^+)$$

$$\therefore \quad \frac{dN}{d(\cos\Theta_\varepsilon^+)} \;=\; \sum_\ell \rho_\ell \, P_\ell(\cos x) \, P_\ell(\cos\Theta_\Lambda^+)$$

APPENDIX C

SAMPLE D.S.T. RECORD

The record is shown overleaf, it is only part of a record but it is sufficient to demonstrate the structure.

The format is :- word number, word contents in three formats floating point, integer, and hexidecimal.

Notes

word 1 = Frame no. × 10 + event no.	Integer
word 2 = No. of hypotheses in the record	Integer

Section A (Header)

i) hypothesis no. × 10 + no. in fit sequence	Integer
ii) no. of constraints of fit + χ^2 probability	Int + fl.pt.
iii) Missing Mass Squared to this fit	Fl.pt.
iv) no. of vertices (NV) , no of tracks (NT)	Hex (packed)

Section B (Vertex block for NV vertices)

i),ii),iii) x, y, z vertex co-ordinates

iv),v),vi) $E^2(x), E^2(y), E^2(z)$ errors

Section C (Track block for NT tracks)

i) a= charge* , b= mass code, c= beginning label, d= end label

ii),iii),iv) $1/p$, ϕ , $\tan \lambda$ unfitted track variables

v), vi), vii) $E^2(1/p), E^2(\phi), E^2(\tan \lambda)$ errors

next 6 words for fitted variables

next 5 words for magnetic field components

xix) half length of track (+100.0 if continues into Ne-H)

---

* Charge = 127 -ve, 128 neutral , 129 +ve, 0 unknown

A	1	0.0000	12400041	000035A9
	2	0.0000	1	00000001
	3	0.0000	210131	00035413
	4	4.8681	1095623040	414DE3F8
	5	0.0000	50397952	03010300
	6	0.0080	131077	00020005
B	7	2.9486	1093618896	412F2D80
	8	-4.6981	-1052032343	C1402B39
	9	23.8892	1108089433	42171609
	10	0.0001	1030192641	3D677E01
	11	0.0001	1027729781	3D41E975
	12	0.0009	1043894625	3E386A51
	13	2.9241	1093585132	412EC8EC
	14	-4.9642	-1051759235	C14F6D7D
	15	23.3204	1108824582	42175206
	16	0.0001	1033213074	3D9594?2
	17	0.0000	1025319433	3D1D2209
	18	0.0015	1046567120	3E6158D0
C	19	*************	2130968577	7F040081
	20	5.8280	1096630189	415D3FAD
	21	-0.0196	-1087660227	BF2B9F3D
	22	3.3426	1094024037	41357B65
	23	0.0000	1026402022	3D2DA6E6
	24	0.0001	1027135343	3D38D76F
	25	0.0148	1060926138	3F3C72DA
	26	5.8280	1096630185	415D3FAA
	27	-0.0104	-1087729775	BF2A8F91
	28	3.3455	1094027096	41358758
	29	0.0000	1026202949	3D2A9D45
	30	0.0001	1027111712	3D387020
	31	0.0031	1059131791	3F21118F
	32	0.0037	1056073586	3EF26772
	33	1.0007	1091568365	411002ED
	34	0.9971	1090470301	40FF419D
	35	-0.0000	-1124102247	BCFF8F99
	36	-0.0000	-1122382001	BD19CF4F
	37	14.9620	1106207848	41EF6468
C	38	*************	2131165442	7FC70102
	39	4.6204	1095363846	4149ED06
	40	0.8847	1088249914	40D1603A
	41	0.0	0	00000000
	42	0.0036	1055523736	3EE0398E
	43	0.0321	1065900257	3F039DF1
	44	-1.0000	-1055010032	C1100000
	45	4.6463	1095391055	414A574F
	46	0.7148	1085733538	40B6FAA2
	47	5.4320	1096211909	4156E97D
	48	0.0011	1044723450	3E4536FF
	49	0.0004	1041852190	3E19671E
	50	0.0211	1062633082	3F5681FE
	51	0.0037	1056035318	3EF1D3E?
	52	1.0000	1091567616	4110000?
	53	1.0000	1091567616	41100000
	54	0.0	0	00000000
	55	0.0	0	00000000
	56	0.1767	1076786303	402D3DFF
C	57	-0.0000	-2135500568	81039100
	58	0.0043	1058266112	3F13DC0E

Acknowledgements

I would like to thank Professor A. W. Wolfendale who made available the facilites of the Physics Department at Durham during my work for this thesis. My particular thanks go to my supervisor Dr. D. Evans and Dr. J. V. Major without whose guidance, patience and help during all phases of the work, this thesis would not have been possible.

I would also like to thank all the other members of the High Energy Nuclear Physics Group at Durham for their many discussions during the course of the work, in particular Mr. A. P. Lotts and Dr. P. S. Jones. My thanks also to the scanning and measuring staff at the University of Durham.

Last, but not least, I would like to thank my fiancée, Yvonne for all her help and encouragement during this work.

To these, and many others , my deepest thanks.

This work was financed by a Durham University Studentship and the Science Research Council.

References

Chapter One

1.1 Berley et. al. Phys. Rev. D <u>1</u> 1996 (1970)

1.2 Tripp et. al. Phys. Rev. D <u>11</u> 3078 (1975)

1.3 Humphrey et. al. Phys. Rev. <u>127</u> 1305 (1962)

1.4 Particle Data Group Rev. Mod. Phys. <u>48</u> pt2 (1976)

Chapter Two

see also

2.1 The operation of a track sensitive target in a 500 litre Neon-Hydrogen bubble chamber. J.F.Ayres (Rutherford Pre-print)

2.2 A low momentum separated beam for use with the 1.5 metre bubble chamber. F. Atchinson RHEL/M/NIM9

Chapter Three

3.1 Y. Hamam Private Communication

Chapter Four

4.1 The Geometrical reconstruction of bubble chamber tracks.J.W.Burren and J. Sparrow NIRL/R/14

4.2 RHEL Bubble Chamber Research Group (Physics Notes) Memo 25 (1970)

4.3 A kinematical fitting program for the analysis of bubble chamber events. A.G.Wilson NIRL/M/38

4.4 Hypothesis assigning in the testing of bubble chamber events. A.G.Wilson NIRL/R/42

4.5 HYBRID - plotting program similiar to SUMX see e.g. SUMX on the Rutherford Laboratory Central Computer. P.J.Hemmings and G.R.Donaldson RL-74-061 C77.

4.6 ELECTRIC Users Manual (Rutherford laboratory 1977)

4.7 MINUIT   Long write-up CERN computer program
Library. F. James and M. Reos D506,D516 1971.

Chapter Five

5.1 Berley et. al. Phys Rev. D $\underline{1}$ 1996 (1970)

5.2 Tripp et. al. Phys Rev. D $\underline{11}$ 3078 (1975)

5.3 Tripp et. al. Phys Rev. D $\underline{7}$ 5 (1973)

5.4 Tripp et. al. Phys Rev. Lett. $\underline{21}$ 1715 (1968)

Chapter Six

6.1 Tripp et. al. Phys Rev.D $\underline{11}$ 3078 (1975)

6.2 Tripp et. al. Phys Rev.D $\underline{7}$ 5 (1973)

6.3 Berley et. al. Phys Rev. D $\underline{1}$ 1996 (1970)

Chapter Seven

7.1 High Energy Particles B. Rossi (Prentice-Hall 1952)

Chapter Eight

8.1 Tripp et. al. Phys Rev. $\underline{183}$ 1200 (1969)